

University of Windsor

Scholarship at UWindor

Electronic Theses and Dissertations

Theses, Dissertations, and Major Papers

2003

Experimental study and theoretical modelling of ultrasonic wave propagation in resistance spot welds.

Andriy M. Chertov
University of Windsor

Follow this and additional works at: <https://scholar.uwindsor.ca/etd>

Recommended Citation

Chertov, Andriy M., "Experimental study and theoretical modelling of ultrasonic wave propagation in resistance spot welds." (2003). *Electronic Theses and Dissertations*. 2028.
<https://scholar.uwindsor.ca/etd/2028>

This online database contains the full-text of PhD dissertations and Masters' theses of University of Windsor students from 1954 forward. These documents are made available for personal study and research purposes only, in accordance with the Canadian Copyright Act and the Creative Commons license—CC BY-NC-ND (Attribution, Non-Commercial, No Derivative Works). Under this license, works must always be attributed to the copyright holder (original author), cannot be used for any commercial purposes, and may not be altered. Any other use would require the permission of the copyright holder. Students may inquire about withdrawing their dissertation and/or thesis from this database. For additional inquiries, please contact the repository administrator via email (scholarship@uwindsor.ca) or by telephone at 519-253-3000ext. 3208.

EXPERIMENTAL STUDY AND THEORETICAL MODELLING
OF ULTRASONIC WAVE PROPAGATION IN
RESISTANCE SPOT WELDS

By Andriy M. Chertov

A Thesis
Submitted to the Faculty of Graduate Studies and Research
Through the Department of Physics
In Partial Fulfillment of the Requirements for
The Degree of Master of Science at the
University of Windsor

WINDSOR, ONTARIO, CANADA
JUNE 2003

© Copyright by Andriy M. Chertov, 2003



National Library
of Canada

Bibliothèque nationale
du Canada

Acquisitions and
Bibliographic Services

Acquisitions et
services bibliographiques

395 Wellington Street
Ottawa ON K1A 0N4
Canada

395, rue Wellington
Ottawa ON K1A 0N4
Canada

Your file *Votre référence*
ISBN: 0-612-92446-7
Our file *Notre référence*
ISBN: 0-612-92446-7

The author has granted a non-exclusive licence allowing the National Library of Canada to reproduce, loan, distribute or sell copies of this thesis in microform, paper or electronic formats.

L'auteur a accordé une licence non exclusive permettant à la Bibliothèque nationale du Canada de reproduire, prêter, distribuer ou vendre des copies de cette thèse sous la forme de microfiche/film, de reproduction sur papier ou sur format électronique.

The author retains ownership of the copyright in this thesis. Neither the thesis nor substantial extracts from it may be printed or otherwise reproduced without the author's permission.

L'auteur conserve la propriété du droit d'auteur qui protège cette thèse. Ni la thèse ni des extraits substantiels de celle-ci ne doivent être imprimés ou autrement reproduits sans son autorisation.

In compliance with the Canadian Privacy Act some supporting forms may have been removed from this dissertation.

Conformément à la loi canadienne sur la protection de la vie privée, quelques formulaires secondaires ont été enlevés de ce manuscrit.

While these forms may be included in the document page count, their removal does not represent any loss of content from the dissertation.

Bien que ces formulaires aient inclus dans la pagination, il n'y aura aucun contenu manquant.

Canada

Abstract

The theoretical and experimental study of resistance spot weld quality has a long history. Since the invention of the method manufacturers are concerned about the means of quality assurance of the joints. One of the most promising current techniques of quality inspection is the real time ultrasonic nondestructive evaluation. In such a system the acoustic signals are sent through the spot weld during welding and then analyzed to predict the size of the future joint. In spite of its purely industrial application and seemingly easy setup the problem involves several complicated mechanisms to be described using a physical-mathematical approach. This thesis is concerned with the development of mathematical models describing thermal dynamics in the system and acoustic wave propagation through it. The analysis of these results helps to understand the ways the system could affect the transmitted signal. The models are compared with experimental observations. Possible applications of the developed simulations are discussed.

To my family

Acknowledgements

I would like to thank many people who supported and encouraged me in my research and study.

I want to express my sincere gratitude to my supervisor Dr. Roman Gr. Maev. His understanding and belief in success have helped me to overcome many difficulties I was faced. His support is of great importance to me as student and researcher.

My deepest respect is due to the members of our team – Elena Maeva, Serge Titov, Alex Denisov, Brian O’Neill, Fedar Seviaryn for their continuous support and advice. Their professionalism and knowledge in different areas forms a really strong team which is the pleasure to work in.

I would like to thank Dr. J.B. Atkinson, Dr. A. Sobiesiak and Dr. G.W.F. Drake for their role as my committee members.

My special thanks to Sarah Beneteau and Emily Schmidt for their concern and help.

I can’t find enough words to express my gratitude and convey my deepest appreciation to my parents for their patience, belief and support.

And I send all my love to my family. My cordial thankfulness to Julia and Arseniy for the inspiration and faith they bring to my heart.

Table of Contents

Abstract	iii
Acknowledgements	v
List of Tables	vii
List of Figures	viii
CHAPTER I	
Introduction	1
1. Foreword	1
2. Development of Nondestructive Techniques	3
3. Scope of Thesis	9
CHAPTER II	
Experimental Setup	11
CHAPTER III	
Temperature Distributions in Spot Weld	25
1. Introduction	25
2. Governing equations and boundary conditions	28
3. Finite Difference Modeling	33
4. Analytic 1D model	50
CHAPTER IV	
Wave Propagation in Spot Weld	63
1. Introduction	63
2. Analytical Approach	66
3. Finite Difference Model	72
CHAPTER V	
Discussions, Conclusions and Future Work	83
APPENDICES	
Appendix A. Material Properties	87
Appendix B. Abbreviations used for analytical solution in Chapter III	91
Appendix C. The Acoustic Field of Circular Transducer	92
Appendix D. Linear Approximation Errors	95

List of Tables

3.1. Summary of the coefficients and material properties.	33
3.2. First few eigenvalues, numerical solution.....	56
3.3. Comparison of analytical and numerical approaches.....	61

List of Figures

1.1. Schematic view of resistance spot welding.....	5
1.2. Weld electrodes with built-in longitudinal wave transducers; trough-transmission method.....	5
1.3. Ultrasonic patterns of the through-transmitted signal as a function of time corresponding to various numbers of welding cycles.....	7
2.1. Schematic view of the welding setup.	12
2.2. Main sources of heat in spot welding.	13
2.3. Metallographic views of cut welds.	14
2.4. Signature (or B-scan) of the weld.	15
2.5. Few waveforms from the signature of the weld.	15
2.6. Waveforms at 6 moments shown on Fig. 4.	16
2.7. Amplitude of the signal during different stages of welding.....	17
2.8. Transmitted amplitude dynamics.	18
2.9. The Fast Fourier Transforms of the signals.....	19
2.10. TOF variation.	20
2.11. Phase shift variation.	20
2.12. Cross-correlation of the signals.	21
2.13. Tracking peak position and reduction of discretization error.	22
2.14. TOF calculation as is – with finite discretization.....	22
2.15. Quadratic approximation of the peak was applied. Increase of accuracy.....	22
2.16. Correlation of TOF parameter with weld nugget size.....	23
3.1. Temperature dependence of longitudinal velocity in steels.....	25
3.2. Temperature dependence of mild steel density.	26
3.3. Resistance spot welding setup.	27
3.4. Thermal boundary conditions.	29
3.5. Contact heat generation.....	30
3.6. Electrical resistivity of mild steel.	31
3.7. Process of melting of steel.	32
3.8. Finite-difference space-time representation. One space dimension.	35
3.9. Nomenclature for finite-difference representation for cylindrical symmetry.....	36
3.10. Finite-difference space-time representation. Two space dimensions.	36
3.11. Heat generation at the steel-steel interface during welding.	39
3.12. Heat generation in the steel plates during welding.....	40
3.13. Stability considerations.	41
3.14. First welding cycle.....	42
3.15. Second welding cycle.	42
3.16. Third welding cycle.....	43
3.17. Sixth welding cycle.....	43
3.18. Ninth welding cycle	43
3.19. End of cycle 11.....	43
3.20. Temperature scale.	43

3.21. Temperature at the faying surface.	44
3.22. Temperature in the middle of the steel plate under the electrode.	44
3.23. Temperature at the steel-copper contact surface.	45
3.24. View of the weld and temperature distribution along central axis; first cycle.	45
3.25. View of the weld and temperature distribution along central axis; 6th cycle.	46
3.26. View of the weld and temperature distribution along central axis; 8th cycle.	46
3.27. View of the weld and temperature distribution along central axis; 11th cycle.	47
3.28. Samples of metallographic sections of spot welds.	49
3.29. Spot weld formation, numerical simulation.	49
3.30. Temperature profile (lower part) in the spot weld along horizontal line.	51
3.31. Schematic view of the 2D setup and its 1D analog.	51
3.32. Graphical representation of the solutions of transcendental equation.	56
3.33. Heat redistribution.	59
3.34. Temperature profile in copper-steel-copper setup at final moment of welding.	60
3.35. Graphical comparison of numeric and analytic results.	61
4.1. Temperature distribution in the spot weld.	65
4.2. Temperature profile in the spot weld along the central axis.	66
4.3. Piecewise approximation in the copper part.	66
4.4. Piecewise approximation in the steel part.	66
4.5. Wave propagating in the media with linear inhomogeneity.	71
4.6. Wave propagating in the media with linear inhomogeneity.2	71
4.7. Discretization of space-time.	73
4.8. Introduction of imaginary layer in the faster media.	74
4.9. Wave with big grid size. In the beginning.	74
4.10. Wave 90 iterations later. The error accumulates as time progresses.	74
4.11. Wave in the media with correct grid size.	75
4.12. Wave 90 iterations later. Error is invisible (very small).	75
4.13. Temperature at first welding cycle.	76
4.14. Temperature at cycle 6.	76
4.15. Temperature at the end of cycle 11.	76
4.16. Velocity at first welding cycle.	76
4.17. Velocity at cycle 6.	76
4.18. Velocity at the end of cycle 11.	76
4.19. Pressure of the wave passing through different materials.	77
4.20. Pressure of the wave passing through different materials.	78
4.21. Stick weld; experimental TOF curve (upper), theoretical (lower).	80
4.22. Good weld; experimental TOF curve (upper), theoretical (lower).	80
4.23. Electrical resistivity of steel as function of temperature.	81

CHAPTER I

Introduction

1. Foreword

Resistance spot welding of sheet metal, commonly used in the automotive industry and other manufacturing operations (Fig. 1), requires a means of ascertaining the quality of the weld joints. The resistance spot welding is a cost effective process and adaptable to high speed automated production. To ensure high quality and integrity of the weld joint, several parameters of the joint need to be controlled, because there are a number of variables in the manufacturing process that can result in a variety of weld discontinuities. A common spot welding problem is the 'cold' weld (stick weld). Such welds are typically formed in mild-to-mild or galvanized-to-galvanized steel combinations when the electrode force is high, the current is low or the cycle time is short, or a combination of all three. Under such conditions, a weld pool never forms. Instead, a small amount of surface melting occurs, resulting in a weak fusion between the sheets. Another problem in spot welding is the undersized weld nugget.

Some methods of quality control are required to ensure reliability of the product. Destructive tests (peel, shear and fatigue tests) have been a common practice for determining the weld quality. But they provide only selective monitoring and are often too costly for the manufacturer. That is why most of the efforts are focused now on nondestructive techniques. Only the latter could provide inspection of each item produced, which is the ultimate goal of quality inspection.

Many research groups have been working on this issue for a few decades. Various approaches have been attempted using a variety of physical phenomena involved in the process, but the problem is still to be solved. As part of our continuing efforts, our team is exploring the ways of spot weld characterization using ultrasound. Even though this approach was tried 35 years ago without much success, technological progress offers much better opportunities to realize this idea today.

The problem has purely industrial background, but its solution requires developing some mathematical models capable to simulate the process and point out the most prospective features to characterize the spot weld quality. Among them are:

- formation of a liquid steel area in the steel sheets using extremely high current densities of magnitude ~ 200 million Amperes/m². Heating of steel from room temperature up to 2000 K takes a fraction of a second.
- propagation of acoustic waves through this severe thermodynamic storm. The system represents a multilayered structure consisting of inhomogeneous pieces; the inhomogeneity arises from temperature gradients of the order ~ 1000 K/mm.

Understanding the mechanisms affecting the acoustic wave on its way through such a system could provide valuable information about the ways the signal should be analyzed. Correct signal interpretation could provide enough information to characterize the weld quality. That is why the development of physical-mathematical models describing these processes is very important in our research and is the main focus of this thesis.

2. Development of Nondestructive Techniques

The continued development of spot weld industry requires the creation of reliable methods of nondestructive monitoring of spot welds. Many techniques have been developed, but the problem of reliability and accuracy of estimation still exists.

Methods of nondestructive evaluation (NDE) for measuring nugget formation include acoustic emission, ultrasonics, and monitoring of temperature and electrical properties such as resistance, voltage, dissipated energy. The monitoring provides information about the quality of the product. The basic ideas of some techniques using measurements of temperature, linear expansion and acoustic emission signals, are reported in [1, 2]. Nondestructive methods such as thermal, electric, X-ray and eddy current are unable to distinguish stick welds (bad welds) from good quality welds. Ultrasonic (US) methods using the pulse-echo technique have shown reliability in this matter and have been implemented in manufacturing operations since 1985. Development of high frequency broadband US transducers enabled the extension of the method to test spot welds as thin as 0.5 mm.

Actual US procedures of spot weld evaluation after welding on cold products, are well described in [3-7]. They consist of a pulsed elastic wave excitation directed perpendicularly to the surface of welded sheets and reception of a series of elastic pulses reflected at the acoustical interfaces. Conclusions about the weld quality are reached by analyzing acquired pulse-echo patterns. This technique makes it feasible to distinguish between 4 configurations (good weld, undersize weld, stick weld and no weld). The above method gives an integral a posteriori estimation of the spot weld quality, but does

not allow feed back into the welding procedure. A modified pulse-echo technique using a masked broadband transducer is described in [7].

Some advanced techniques based on the application of acoustic microscopy methods, have been recently reported. A cylindrically focused 20 MHz contact pick-up linear array probe has been used in [8] to monitor the spot weld diameter. The main advantage of the device is that instead of mechanical scanning, electronic scanning is implemented. However, the uneven state of the nugget surface usually affects the obtained results.

A two-dimensional map of the spot weld was obtained using scanning acoustic microscopy [9-10]. An immersion spherically focused 50 MHz transducer [10] performs a C-scan in the plane parallel to the welded metal sheet surface, and the corresponding reflected signal amplitude distribution is recorded and visualized with a good resolution. The major advantage of the method is the visual character of the welded area presentation, clearly distinguishing 'stick weld' and 'no weld' areas and welding flaws.

Ultrasonic NDE techniques consisting of measurements during the welding process, are particularly advantageous since they permit feedback during the process so that the welding current can be maintained to produce a good quality weld. So that, the welding current should be maintained up to good quality spot weld. This approach was investigated in a series of papers [11-15]. In [11, 12] elastic Lamb waves were used to get information about the weld nugget configuration and size. The method is based on real-time weld monitoring by measuring the amplitude of ultrasonic Lamb wave signals transmitted through the weld region. The transmitted signal is affected by temperature changes in the weld region during cooling and solidification of the molten pool. The time

from weld current cutoff to the attenuation maximum corresponding to the temperature of the austenite-pearlite transformation, depends on the heat capacity of the molten pool and therefore can be related to the nugget size and the weld strength. The nugget size in this method is estimated indirectly, and various physical factors, such as electrodes' pressure, acoustical and thermal damping of electrodes, steel sheet thickness variations can modify the cooling and in consequence give erroneous results.

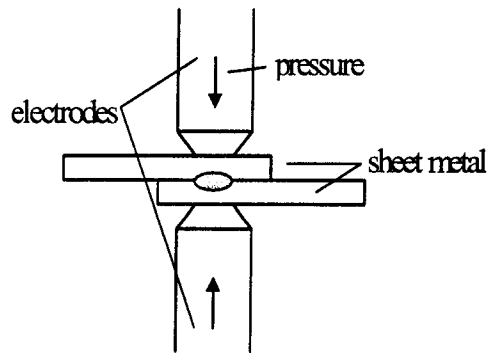


Figure 1. Schematic view of resistance spot welding

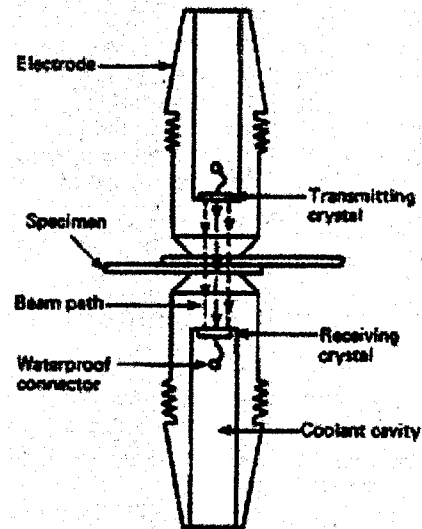


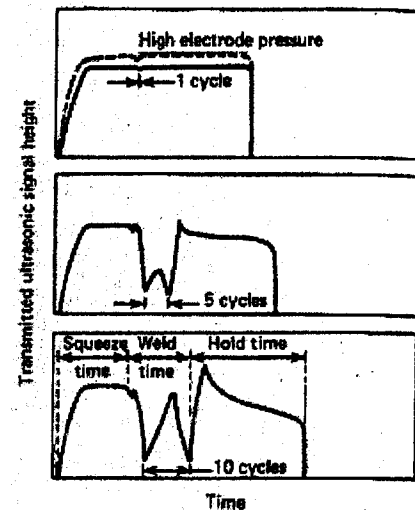
Figure 2. Weld electrodes with built-in longitudinal wave transducers; trough-transmission method (Ref. 13)

Some developmental efforts have been given to the Lamb wave technique using non-contact Electro-Magnetic Acoustic Transducers (EMAT). The method still has not been implemented into the manufacturing process due to above mentioned difficulties and problems of decoupling EMAT from the welding machine's electromagnetic noise.

Normal incidence ultrasonic transducers (i.e. those generating an acoustic beam perpendicular to the metal sheet surface) mounted in the welder electrodes, may have

some advantages in comparison with the Lamb wave technique, due to the direct estimation of the nugget configuration (cross section and thickness). A schematic view of welder electrodes with built-in ultrasonic transducers is given in Fig. 2. The scheme using the through-transmitted signal was first applied in 1965 for the aluminum spot weld nugget growth monitoring [13]. Two 5 MHz X-cut quartz elements were glued directly inside the electrodes, and the through-transmitted signal amplitude was monitored during welding. The resulting ultrasonic patterns as a function of time corresponding to various numbers of welding cycles are shown in Fig. 3. Initially the transmitted signal is close to zero, then, it increases due to applied pressure, and then remains constant until the welding current starts. The signal drops abruptly following the welded metal heating and the corresponding increase in the ultrasonic wave attenuation. As the molten pool starts to grow, so does the through-transmitted signal. As temperature of the molten metal grows, the attenuation of the signal goes up again. After the current cutoff the welded metal begins to cool, the ultrasonic amplitude first increases, and when the crystallization begins, the ultrasonic attenuation grows again. The maximum height of the signal was plotted with respect to the measured nugget diameter and a good correlation between the ultrasonic through signal height and the nugget diameter has been obtained. Similar technical aspects of the same method are also discussed in [14-16].

Figure 3. Ultrasonic patterns of the through-transmitted signal as a function of time corresponding to various numbers of welding cycles (Ref. 13).



Transmission techniques can, in theory, be particularly advantageous when using normal incidence shear waves. The advantages in employing shear waves are:

- Lower sound velocity and thus higher spatial (frontal and lateral) resolution;
- Total reflection of normal incidence shear waves from the 'solid-liquid' interface;
- Better sensitivity to stick weld interface detection.

The molten nugget should mostly reflect normal incidence shear wave beam created by one of the transducers and thus produce an intense shadow on the receiver, which drastically diminishes the received signal. It is important to note that a stick weld does not shadow the beam. However, many researchers reported no significant advantage of shear waves despite the theoretical 100 percent reflectivity at the interface [17, 18]. Reduced reflected ultrasonic signals and the 'liquid-solid' interface roughness have been also observed. Apparently two factors are present: temperature attenuation effects are more severe for shear than for longitudinal waves, and due to dendritic grain growth the solid-liquid interface appears to be rough, which significantly modifies reflection-refraction coefficients.

An echo-pulse technique was applied for molten pool geometry evaluation using longitudinal waves [18]. No significant difference was observed in reflected signal amplitude between shear and longitudinal waves. The shear wave attenuation coefficient in metals is about 3-5 times greater than that of longitudinal waves, so that shear waves are usually used at lower frequencies rather than longitudinal waves.

Direct implementation of the above mentioned techniques in the manufacturing process is not straightforward, due to extremely severe thermal and mechanical exposures of welder electrodes, technical constraints of the welding electrode-holder assembly, and possible pressure and temperature variations during welding time. Only a few techniques have been implemented on industrial floor and still their accuracy needs to be improved.

The attempts of our team are concentrated on the study of through-transmission techniques using longitudinal waves. The time of flight (TOF) of the signal is the focus of the research. The very high (90-95 %) correlation of TOF with the weld size made us turn our attention to it. It is believed that this is the most stable parameter and it is not much affected by misalignment of the tips, wearing and other side effects. It will be shown that while the amplitude and attenuation of the signal are very much dependent on the surface conditions, the time of flight is more reliable and steady. We therefore concentrate our efforts to try to solve the problem of real time quality assurance of the spot welds using TOF. A thorough analysis of the experimental results and development of adequate models are required in order to understand the mechanisms affecting the signal, and probably to find some other features to help characterize the welds using ultrasound.

3. Scope of Thesis

In spite of its purely industrial nature the problem of spot welding provides a wide range of interesting physical problems. Understanding them could enable us to develop reliable algorithms for nondestructive quality control techniques.

In this research the analysis of ultrasonic transducer configuration using the transmission method is made. The thermal dynamics and the transmitted acoustic signal patterns are analyzed both numerically and analytically. The most flexible and promising technique – the time-of-flight method – is outlined regarding its efficiency to acquire unambiguous data about the joint properties. The model of spot weld formation is developed to calculate temperature and then material property distributions. The latter are consequently used to analyze acoustic wave propagation in the setup. The models make it possible to obtain the theoretical TOF curve of the through transmitted signal. It is shown that the experimental and theoretical curves are close and have common features.

The practical importance of the obtained calculations is discussed. The most interesting application is solving the inverse problem: the calculation of the temperature distributions in the spot weld using experimentally obtained TOF curve. The possibilities of the method and the influence of the side effects are discussed.

References

1. D.V. Dickinson. *Resistance Spot Welding in Metals Handbook*. 9th edition, ASM, 1983.
2. A. Gedeon, C. D. Sorensen, K. T. Ulrich, and T. W. Eagar, *Measurement of Dynamic Electrical and Mechanical Properties of Resistance Spot Welds*. Welding Research Supplement, Dec. 1987, pp. 378-385.
3. Pittaway R. G. *Ultrasonic Testing of resistance Spot Welds*, Weld. Met. Fabr., 35, 1967, pp.443-447.
4. *Ultrasonic Testing Applications in Welding*. Nondestructive Testing Handbook. Vol. 7, technical eds. A. S. Birks, R. E. Green, Jr., and ed. P. McIntire, ASNT (1991).
5. *Nondestructive Evaluation and Quality Control*. ASM Handbook Vol. 17, ASM International, (1989), pp. 597-600.
6. Mansour T.M. *Ultrasonic Inspection of Spot Welds in Thin-gage steel*. Materials Evaluation, 46 (1988) pp. 650-658.
7. J. Krautkramer, H. Krautkramer. *Ultrasonic Testing of Materials*. New York: Springer-Verlag, 1969.
8. H. Yuasa and K. Masazumi. *Inspection Device for Spot Welded Nugget*. Acoustical Imaging, Vol. 22, P. Tortoli and L. Masotti, eds. NY Plenum Press (1996), pp. 771-778.
9. T. Adams. *Ultrasonic Microscope Aids In Spotting Unsound Welds*. Welding Journal, Aug. 1984, pp. 47-48.
10. R. Gr. Maev, D. F. Watt, R. Pan, V. M. Levin, and K. I. Maslov. *Development of High Resolution Ultrasonic Inspection methods for Welding Microdefectoscopy*. Acoustical Imaging, Vol. 22, P. Tortoli and L. Masotti, eds. NY Plenum Press (1996), pp. 779-783.
11. S.I. Rokhlin, M.C. Chan and L. Adler. *Quantitative Evaluation of Spot Welds by Ultrasonic Waves*. Review of Progress in QNDE, Vol. 3B, eds. D. O. Thompson and D. E. Chimenti, NY Plenum Press (1984), pp. 1229-1241.
12. S.I. Rokhlin, R. J. Mayhan and L. Adler. *On-Line Ultrasonic Lamb Wave Monitoring of Spot Welds*. Mater. Eval., 43, (1985), pp. 879-883.
13. G. E. Burbank, and W. D. Taylor. *Ultrasonic In-Process Inspection Of Resistance Spot Welds*. Supplement to the Welding Journal, May 1965, pp. 193-198.
14. Murray E. E. *Ultrasonic in-Process Control of Spot Welding Quality*. Materials Evaluation, 25 (1967) pp. 226-230.
15. Hall E. T., Crecraft D. I. *NDT of Resistance Spot, Roll Spot Stitch and Seam Welds*. Non Destructive Testing, 4 (1971) pp. 181-191.
16. D. I. Crecraft and G. Warner. *Ultrasonic Evaluation of Electrical Resistance Spot Welds*. Non-destructive Testing, February (1969), pp. 40-43.
17. C. Lynnworth, and E. H. Carnevale. *Ultrasonic Testing of Solids at Elevated Temperatures*. Proceedings of the Fifth International Conference on Nondestructive Testing, Queen's Printer, Ottawa (1969), pp. 300-307.
18. Lott, *Ultrasonic Detection of Molten/Solid Interfaces of Weld Pools*. Materials Evaluation, 42, March, 1984, pp. 337-341.

CHAPTER II

Experimental Setup

Method of Nondestructive Evaluation of the Weld Quality

The experimental system included a “scissors” resistance spot welder equipped with a Pertron welding control, two embedded 5 MHz broadband ultrasonic transducers, and the data acquisition system consisting of a USD-15 (Krautkramer’s ultrasonic pulser-receiver), and a TDS-520 (Tektronix digitizing oscilloscope). Later, the data acquisition system consisting of several devices was replaced by a few electronic boards. The latter were incorporated in the unit responsible for both signal acquisition and communications with the welder controller. The measurement system also contained a PMAC-2000 force gauge and a WS-25 (Robotron) welding current monitor, and a PC for the final signal analysis. A single-turn coil has been also installed in the neighborhood of the welder frame in order to monitor the welding current. A view of the system and its constituent blocks is given in Fig. 1.

The welding system enables us to join together the steel plates of different thicknesses (0.5-3 mm) and coatings. In the first stage of the welding process, electrodes squeeze the plates exerting pressure in the range of 500-1500 lbs. The AC (or DC) current, ranging from 5 to 15 kA, is being sent through the setup. The welding time is measured by cycles, each lasting $1/60^{\text{th}}$ seconds, and lies in the range of 5-20 cycles. Only certain combination of pressure, welding time and current produce good welds.

When the current passes through the stack it generates Joule heat. Most of the power is dissipated on the steel-steel interface, since it has high resistance due to the roughness of the surface. The heat is also dissipated at the steel-copper interfaces and in the volume of copper and steel, Fig. 2. As time progresses, the most heated central part between steel plates begins to melt. A proper adjustment of current and welding time produces the spot weld of required size. Fig. 3 shows metallographic sections of a good and poor (stick) weld. Visual inspection of such welds does not provide enough information about their quality. Only destructive testing and some nondestructive techniques reveal the real structure of the weld.

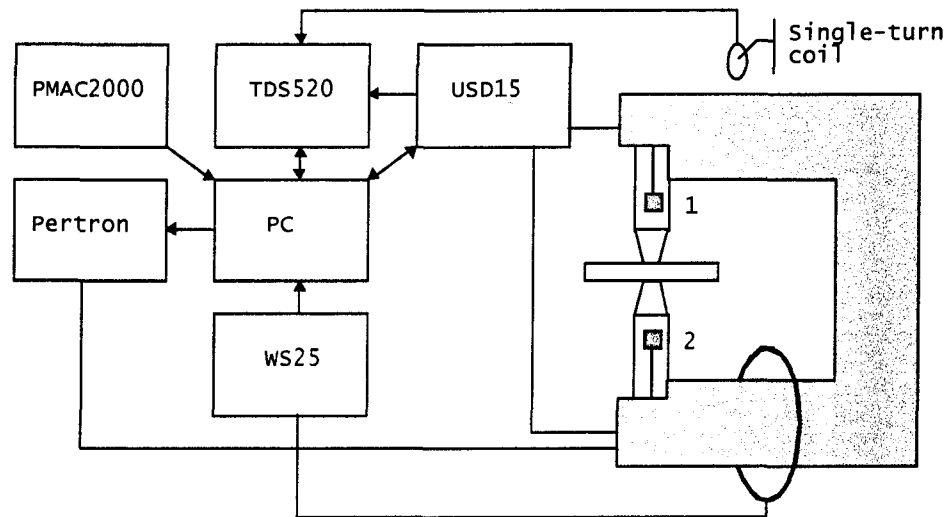


Figure 1. Schematic view of the welding setup. The PC drives the weld controller Pertron to run the welder. The PC drives the Krautkramer USD15 which is synchronized with oscilloscope TDS520. The USD15 sends a signal at emitting transducer 1 and picks it up at the receiving transducer 2. The acquired data are transferred to the TDS520 and finally uploaded to the PC. PMAC2000 measures the pressure exerted on the steel plates by electrodes. The WS25 current monitor measures the current parameters during welding.

The pulser-receiver sends a series of pulses through the system during welding. The pulse repetition frequency is 400 Hz. During the 0.6-0.8 seconds of the welding process,

a set of 240-320 waveforms is acquired and uploaded into the PC. The “train” of pulses is called B-scan or signature and is represented graphically in Fig 4.

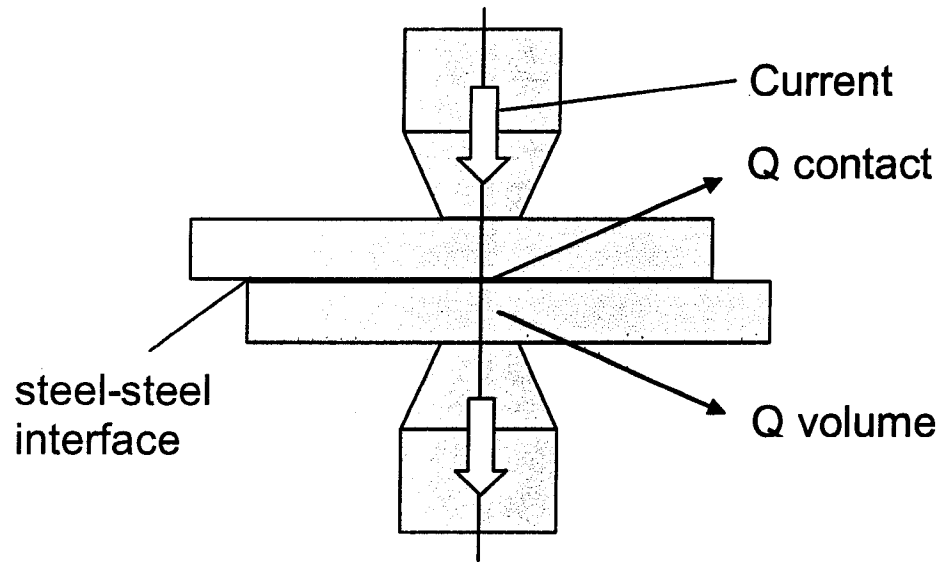


Figure 2. Main sources of heat in spot welding.

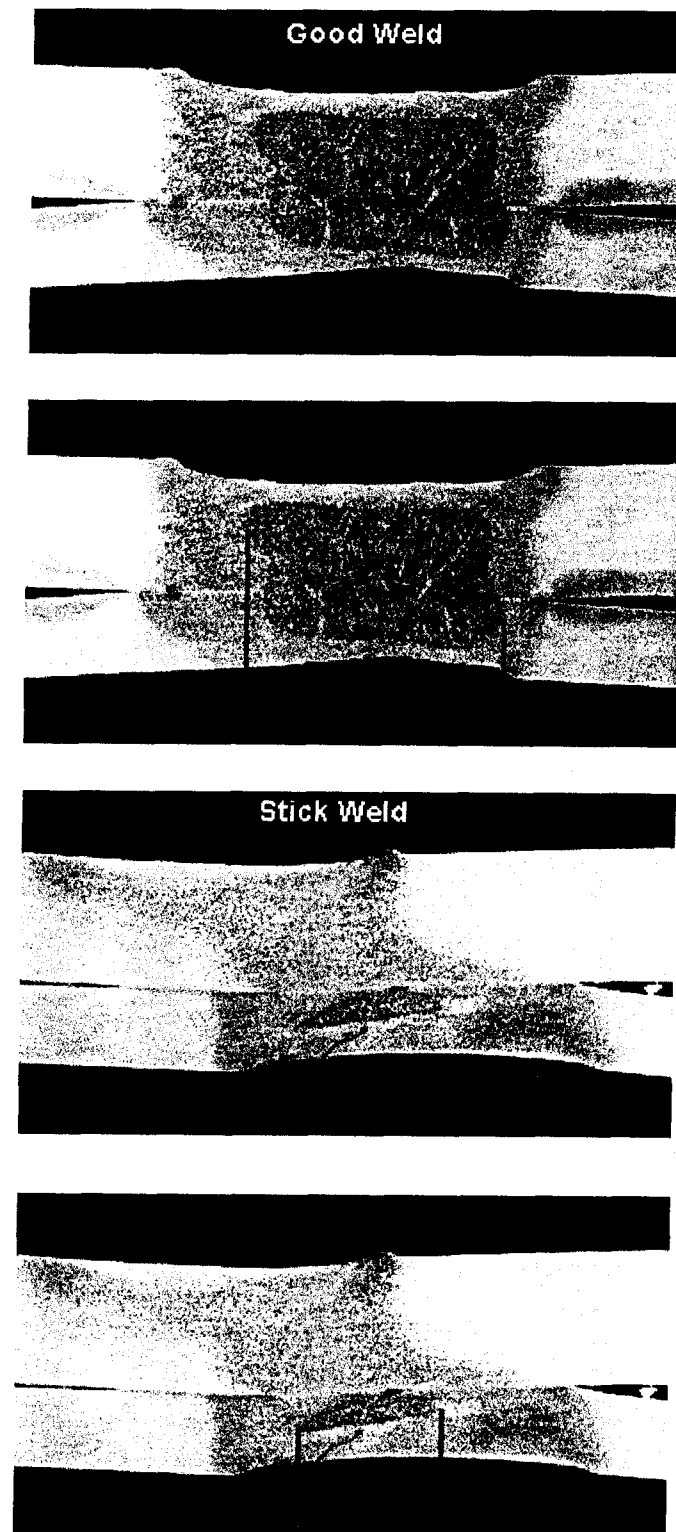


Figure 3. Metallographic cross-sectional views of welds. The first two pictures show good weld and its effective size; the last two pictures show bad weld with weak adhesion strength.

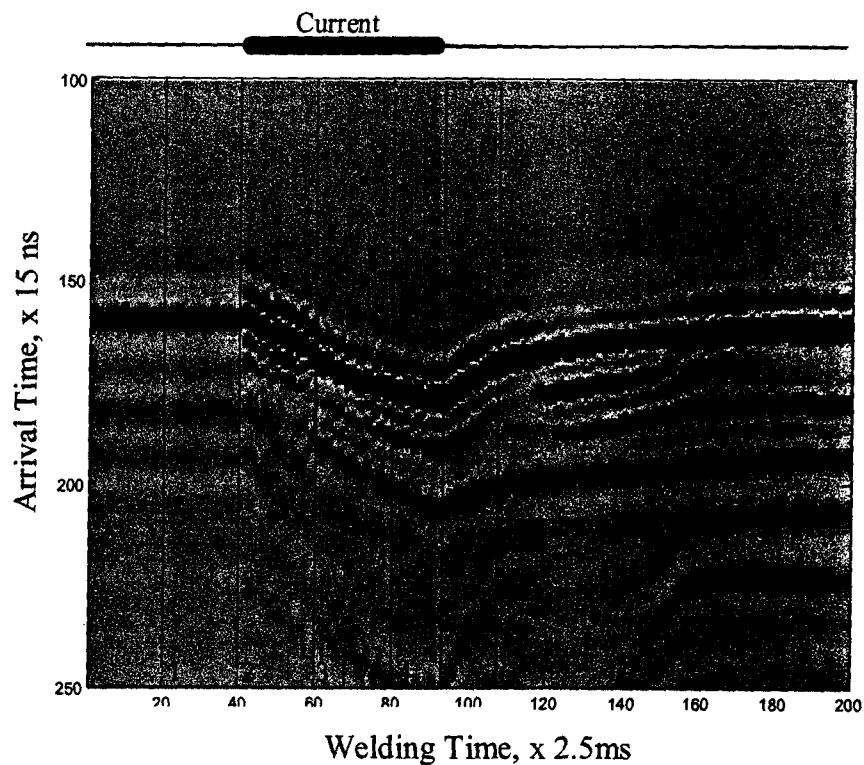


Figure 4. Signature (or B-scan) of the weld – the set of 200 waveforms put together. They cover the time period from before the welding, welding itself and cooling (solidification) of the new weld.

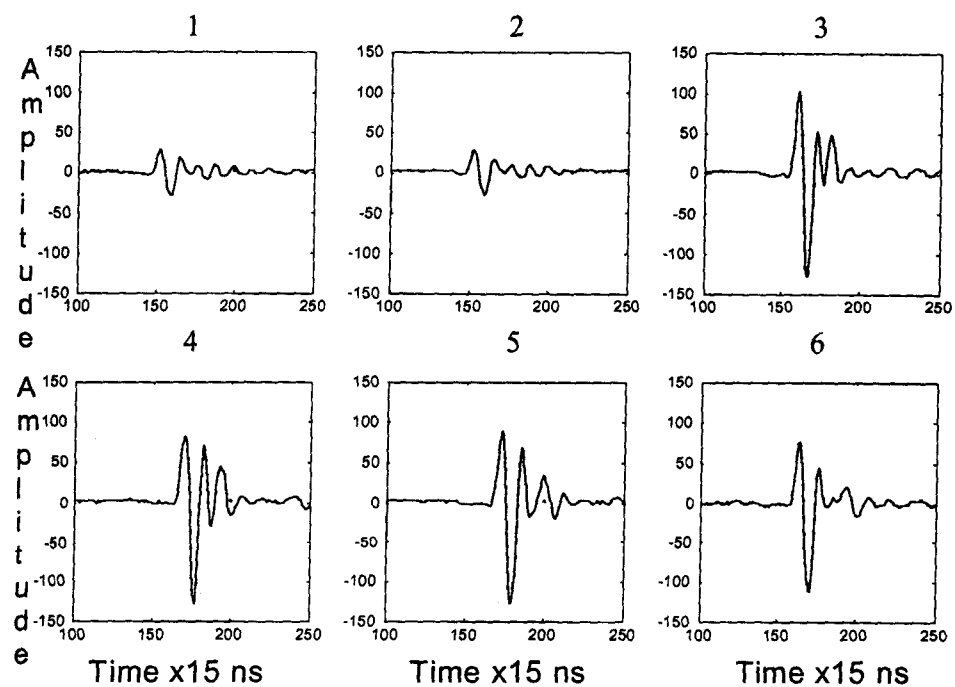


Figure 5. Waveforms at 6 times shown on Fig. 4.

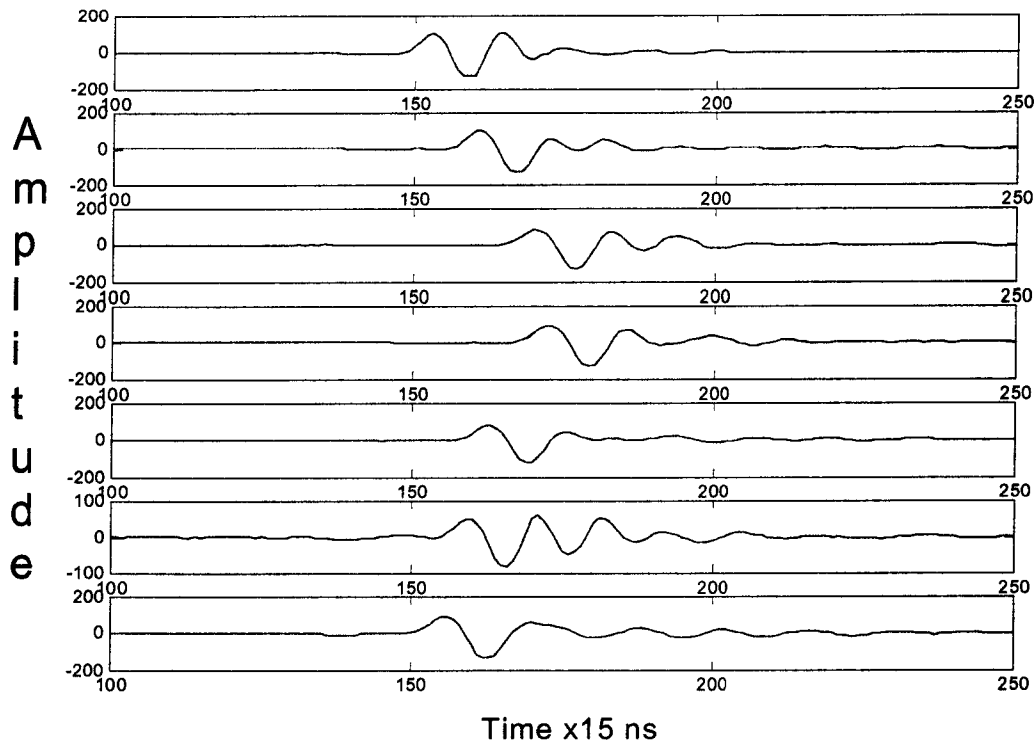


Figure 6. Waveforms of the signature demonstrate the change of the arrival time at different moments of welding. 1.0 mm steel plates, 600 lbs electrode force.

The data acquisition starts 0.1 s before welding, when the electrodes have already squeezed the steel plates. The weak horizontal lines from scan 1 to 40 in Fig. 4 represent this period. When the 60 Hz AC current is on, each transmitted signal arrives later than the previous one (scans 41 through 92 on Fig. 4). It is caused by thermal expansion and velocity drop in the material. It is also clearly seen on Fig. 6 – each of the first four waveforms sent within this time interval, arrive later than the previous one. Turning off the current makes the system cool down causing the signals to arrive earlier – seen in scans 93 to 200. The system loses the acquired heat. Fig. 5 shows a selection of signals taken at the different times shown in Fig. 4.

After the series of welds and signatures is obtained the peel test is performed for the welds. The button average radius is the direct characteristic of the weld quality. The

idea of the nondestructive method is to find some parameters in the signature which are stable and correlate well with the weld size. It would enable us to make estimations without peeling the sample once a reliable database is collected.

Different signal processing techniques have been used to find the parameter which correlates best with the nugget size. Two parameters could be used to characterize the weld size: nugget diameter and nugget height. For a good weld the ratio of nugget diameter and height lie in the range of 2.5-3.0. Thus one can measure either of these two parameters to qualify the weld. The analysis of the signal amplitude during welding has revealed some common features for a series of welds. Fig. 7 shows the most stable parameters in amplitude dynamics. The ratio of A and B parameters provided satisfactory correlation with the weld size, but only within very narrow range of welding variables. The main reasons for instability of the amplitude method (see Fig. 8) are:

- the changing interface conditions (variable pressure, aging of electrodes);
- focusing-defocusing properties of the molten region (it works like a lens);
- misalignment and angle change affect the transmission coefficient at the interface.

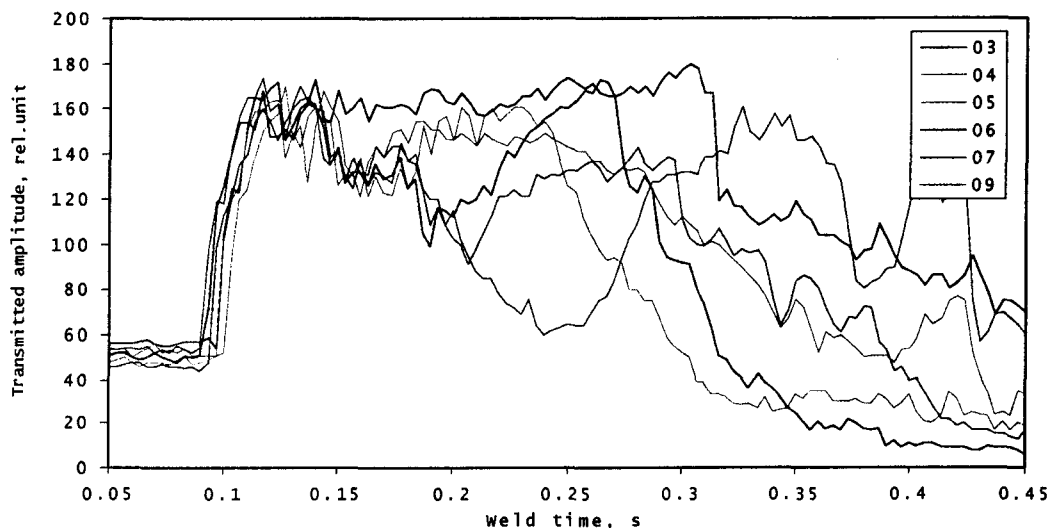


Figure 7. Amplitude of the signal during different stages of welding. Dynamics at various cycles in 2.0mm steel plates recorded at 55% current (part of the cycle at which the current is on), 1200lb force. Different number of welding cycles.

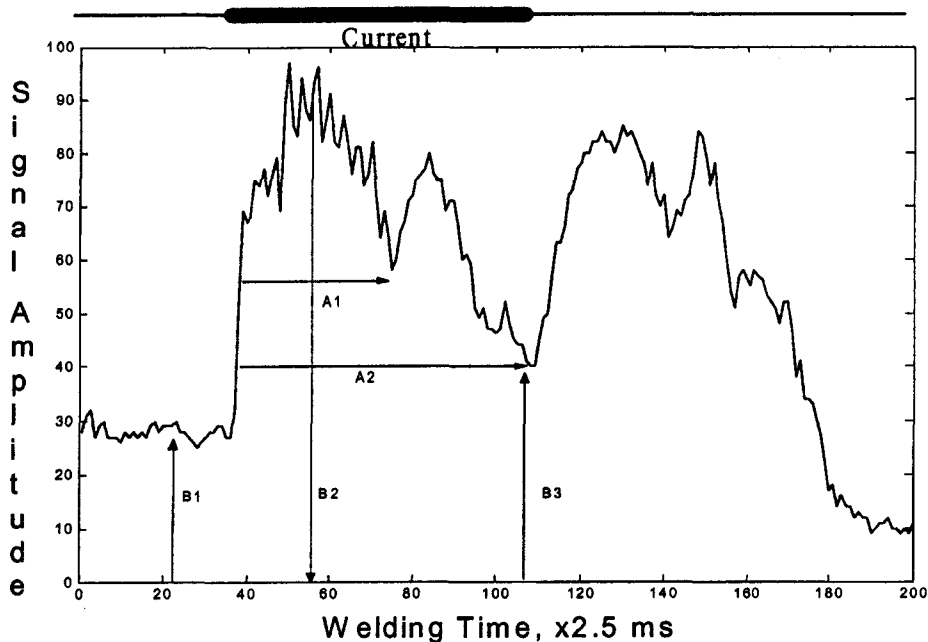


Figure 8. Transmitted amplitude dynamics. Analogous to Fig. 3 in Chapter I.

The spectrum of the signal did not reveal any dependence on the nugget size. Bigger attenuation of high frequencies in liquid steel or nonlinear effects due to material phase transformation has not been discovered. One of the possible reasons is that these effects could be hidden under much more powerful changes of amplitude due to electrode pressure variations and unstable conditions on the interfaces. The signatures and spectra of the waveforms passed through the stick (unwelded) and normal weld at various moments of welding are shown on Fig. 9.

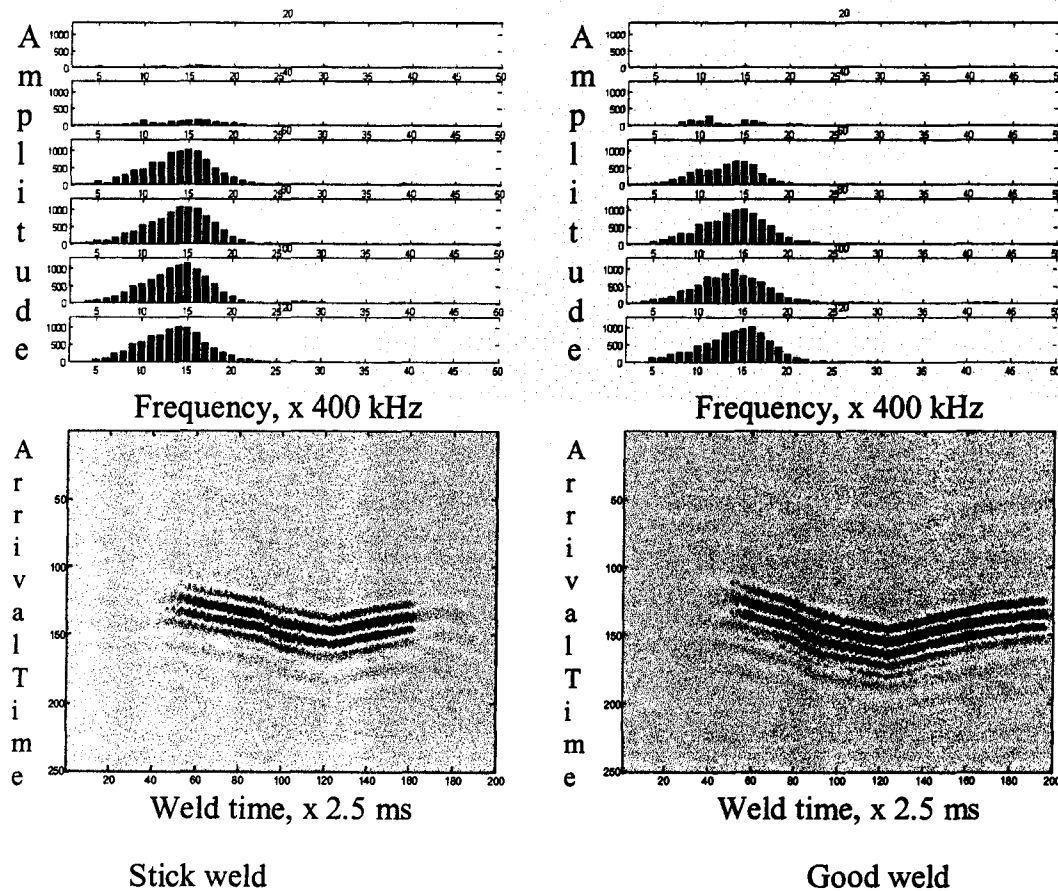


Figure 9. The Fast Fourier Transforms of the signals passed through stick and good weld at different welding moments. The spectrum of the signal does not change much at the moment of melting.

The phase analysis of the signal spectrum has shown good correlation of phase shift with weld size. The phase shift of few harmonics near the central frequency (about 5 MHz) has shown stable dependence on the welding procedure. In fact, only relative phase shift of the waves with respect to each other is of practical interest – phase shift of the waves sent through the weld at different moments of welding. Fig. 11 shows three phase shifts of the harmonics close to the central frequency. Different phase lags correspond to the wavelength of specific harmonic. Working on the same harmonic (frequency) at different welds gave strong correlation of the height of the curve h with weld size.

In fact, the phase shift in this case is nothing else but time of flight of the wave. As current is on and time progresses, the material is being heated gradually. Heating causes:

- change of the material properties of steel and copper which leads to the acoustical velocity drop and thus the delay of the signal;
- moving of electrodes (and transducers) apart due to the thermal expansion, which increases the effective travel distance of the signal.

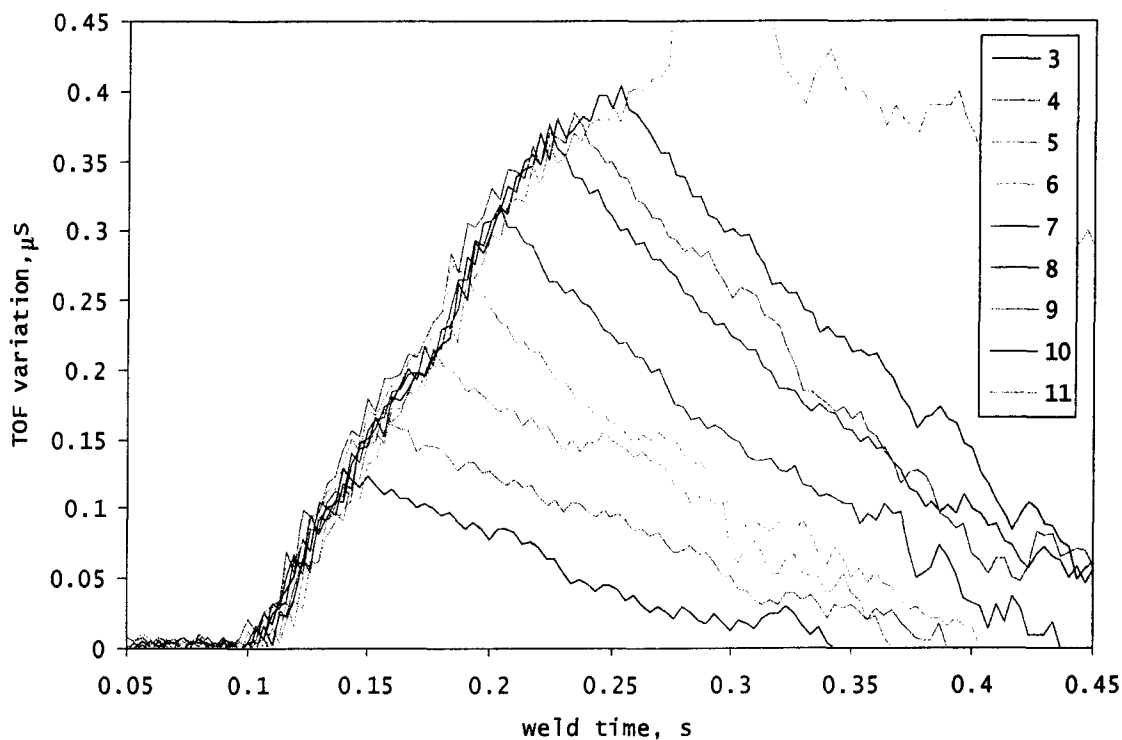


Figure 10. TOF variation at various cycles in 2.0mm steel plates recorded at 55% heat, 1200lb force.

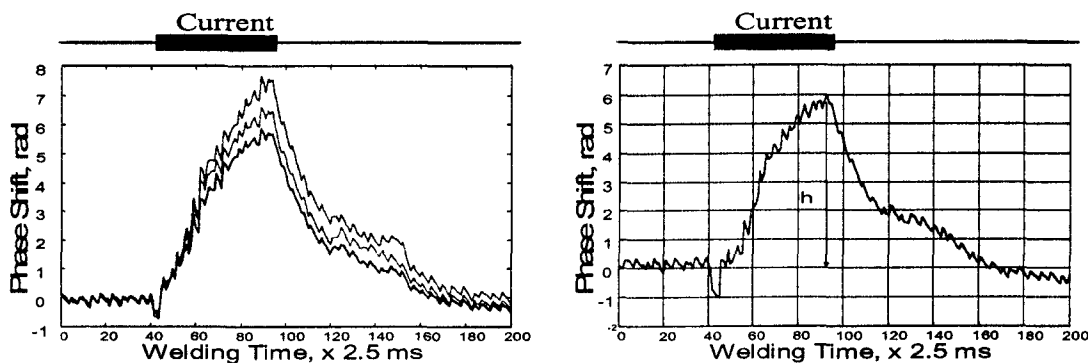


Figure 11. Phase shift variation resembles TOF much. The same way as for TOF the height of the peak characterizes the degree of heating of the setup.

The analysis has shown that time of flight correlated with nugget diameter much better than other signal parameters. Thus TOF was considered to be the most reliable characteristic of weld quality.

Two other methods have been used to calculate the TOF of the signal. The arrival time of the signal at different moments of welding was compared with the arrival time of the signal through the cold setup. In order to minimize possible spectrum changes and thus minimize the error in TOF calculations cross-correlation technique has been applied. This is illustrated in Fig. 12. The original signal (through the cold setup) was cross-correlated with the signals received during welding.

$$P(t) = C(t) * [C_T(t)]$$

In this case the signal is better localized and TOF calculation is more precise. It can be calculated as the distance from zero to the main peak position.

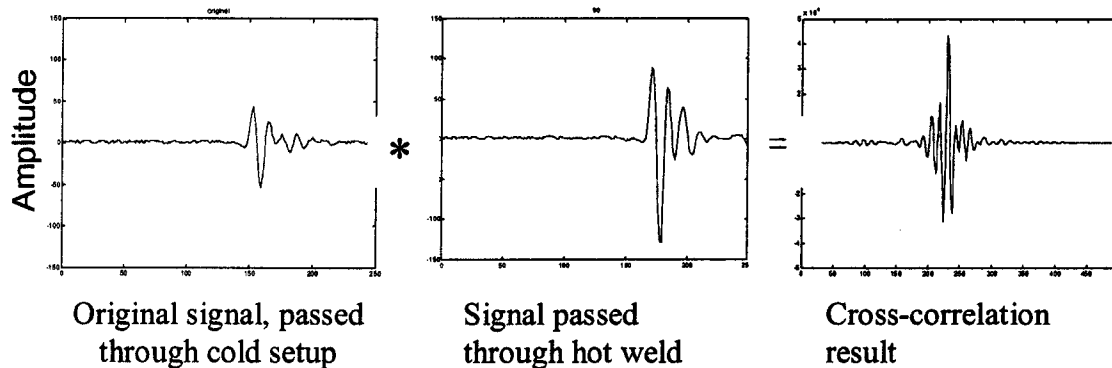


Figure 12. Cross-correlation of the signals using original signal transmitted through cold system.

The direct calculation of the TOF involves localization of one of the peaks of the signal and tracing its position in every waveform. Due to the finite digitizing of the signal there exists ambiguity in the calculation of the peak position. To reduce error, a quadratic approximation at the extremum of the signal was used as shown in Fig. 13. The

approximation used seven points near the peak – the peak itself and three points to the left and to the right – to represent parabola symmetrically. Seven points was enough to represent the shape of the lower part of the wave. The TOF curve can be visually inferred from the “signature” of the weld (see Fig. 4 (page 15)). The TOF curves for different welding times are represented on Fig. 10.

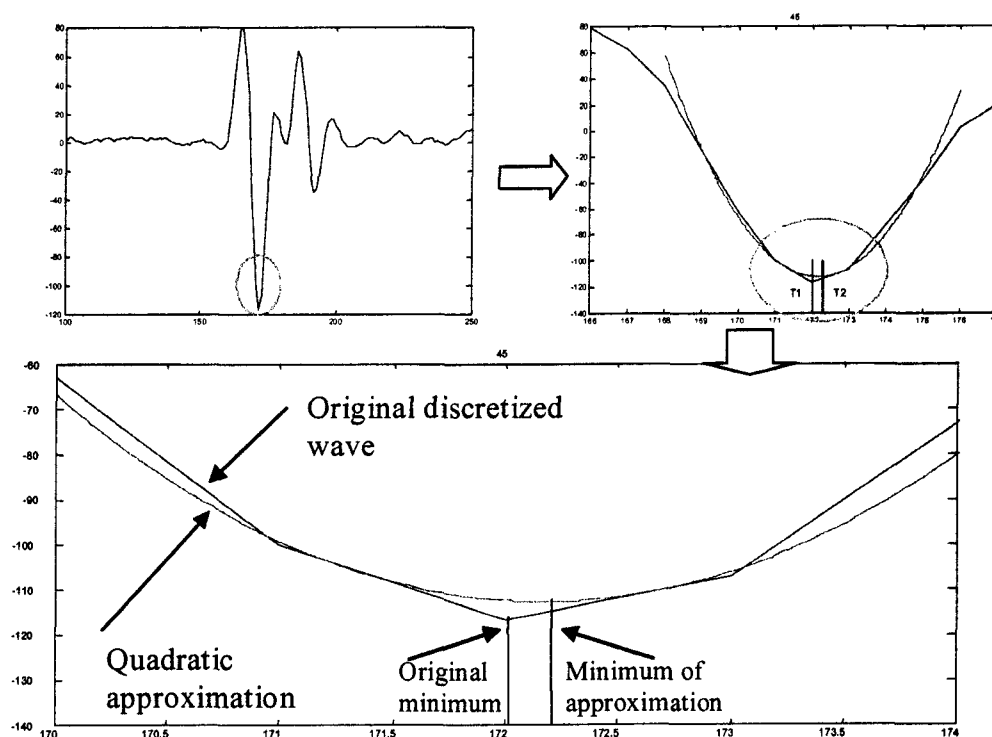


Figure 13. Tracking peak position and reduction of discretization error.

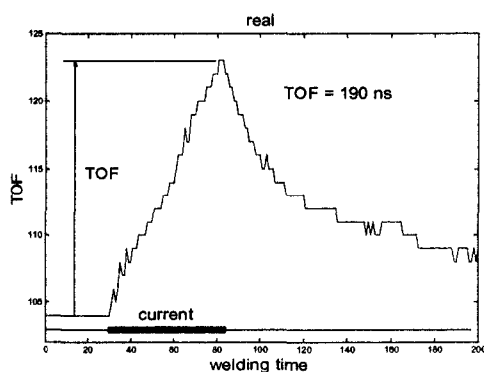


Figure 14. TOF calculation as is – with finite discretization

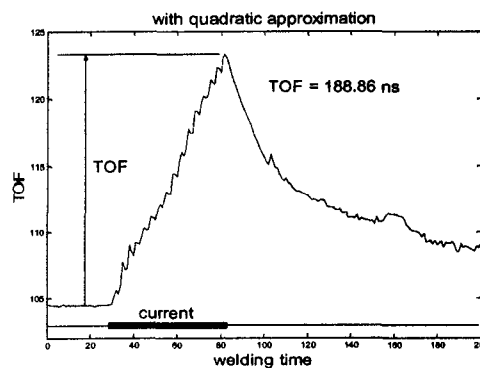


Figure 15. Quadratic approximation of the peak was applied. Increase of accuracy.

All three methods – phase shift, cross-correlation and direct TOF calculation have shown strong correlation with the weld size. The peak on the TOF curve represents the last moment of current flowing through the setup. Thus it reflects the moment of the highest degree of heating, and thus can best characterize the future nugget size. The maximum value of TOF occurs at the end of the current pulse through the setup. It therefore occurs at the highest temperature and hence at the largest molten pool size which is the future nugget size. A typical plot of maximum TOF versus weld size is shown in Fig 16. The fit to a straight line is quite good with the r-square value ranging between 0.90-0.95.

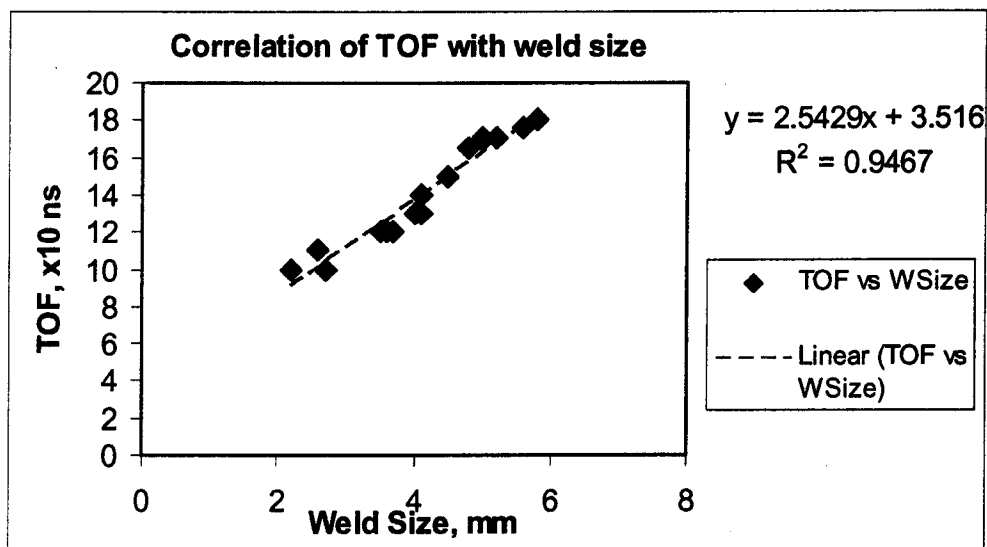


Figure 16. Correlation of TOF parameter with weld nugget size; 1 mm galvanneal (zinc coated) mild steel plates; 600 lbs, 8 welding cycles, current range 7-11 kA.

Two main mechanisms cause the delay of the received signal. As has been mentioned above they are the decrease in the velocity of sound and the thermal expansion of the metal. They are a measure of the degree of heating of the material. The inverse problem of measuring the amount of heat transferred to the system can be solved from the

TOF delay measurement and hence to estimate the nugget size from the empirical database.

The modeling of the heating process enables one to calculate the contributions of thermal expansion and velocity drop to the total TOF delay. It helps to separate these effects later during analysis. Knowing the material properties as a function of temperature (thermal expansion, density, velocity), the exact pattern of temperature distributions in the spot weld system and the total signal delay, one can recalculate the possible nugget size. This is the final goal of the in-line spot weld characterization technique.

The model also enables one to visualize the process and helps one to understand the main mechanisms affecting the signal. The direct estimation of the nugget size by measuring the size of the molten region using the reflection mode can also be examined using this model. The theoretical efficiency of the technique will be also estimated using this method.

References

1. A. Ptchelintsev, R.Gr. Maev. Method of Quantitative Evaluation of Elastic Properties of Metals at Elevated Temperatures. Review of Progress in Quantitative Nondestructive Evaluation, Ames Iowa 2000, Volume 20B.
2. R.Gr. Maev, A. Ptchelintsev. Monitoring of Pulsed Ultrasonic Waves' Interaction with Metal Continuously Heated to the Melting Point. Review of Progress in Quantitative Nondestructive Evaluation, Ames Iowa 2000, Volume 20B.

Chapter III

Temperature Distributions in a Spot Weld

1. Introduction

In order to model the wave propagation in the spot weld it is essential to know the physical properties of the material at every moment of welding and at every point of interest. Large temperature gradients (~ 1000 K/mm) give rise to large material property gradients which affect the wave propagating through the setup.

Therefore one needs to know the temperature distribution in the setup at every moment so that it can be recalculated into the acoustic velocity and mass density fields. The temperature dependence of the velocity and density is taken from [1, 2]. Plots are shown in Figs. 1, 2. The temperature dependence of the longitudinal and shear velocities and the mass density can be used to obtain Lamé constants using equations

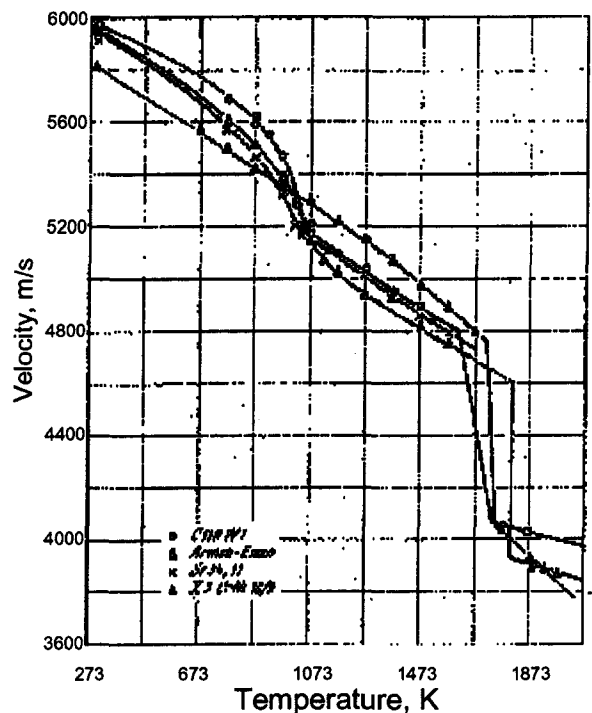


Figure 1. Temperature dependence of longitudinal velocity in steels. Courtesy of [1].

$$c_{longitudinal} = \sqrt{\frac{\lambda + 2\mu}{\rho}} \quad c_{shear} = \sqrt{\frac{\mu}{\rho}}$$

c is the velocity of wave propagation, ρ is the material density, and

$$\lambda = \frac{\nu E}{(1+\nu)(1-2\nu)}, \quad \mu = \frac{E}{2(1+\nu)}$$

are the Lamé constants defined in terms of other solid material properties – Young's modulus E and Poisson ratio ν . The Lamé constants should be used in the equation of motion describing propagation of vibrations in the media.

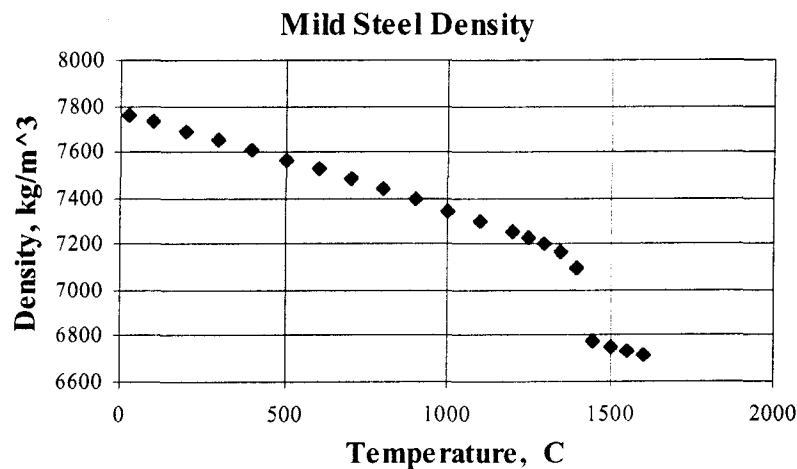


Figure 2. Temperature dependence of mild steel density. Courtesy of [2].

The weld nugget in resistance spot welding (RSW) is produced by melting a small amount of metal in the contacting plates. The electric current passing through the plates generates heat due to the Joule effect. Two main mechanisms of heat generation are known, contact and volume generation. The first one arises from the roughness of the contacting surfaces of plates and electrodes. It vanishes very quickly as the material is being heated. The second one is characterized by the resistivity of the material itself. As the contact resistance between plates is very high at the very beginning of welding, the most heated zone of the setup will be located between the plates. As long as the resistivity

directly depends on temperature, this area will continue to be the hottest even after the contact resistance disappears. In general the generated heat depends on the total resistance of the setup and the square of the current passing through it.

The main components of the system are depicted in Fig. 3.

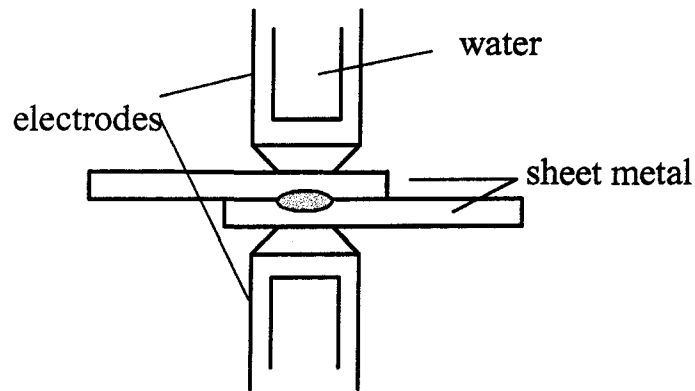


Figure 3. Resistance spot welding setup.

The copper water cooled electrodes exert force on the plates to be welded. The pressure may vary in the range of 500-1500 lb. For 2.0 mm bare steel plates the required pressure is 1300 lbs. The contact resistance is mainly characterized by the type of plate coating and the pressure applied. A pressure increase usually leads to a decrease of contact resistance. The heat generation occurs mainly in steel as its resistivity is much higher than that of copper. Also contact resistance between plates is higher than between plates and electrodes because of the softness of copper. To generate enough heat to melt steel one needs to use very high currents of the order of kilo amperes. High thermal conductivity of copper provides efficient cooling after welding to help fast solidification of the molten region.

2. Governing equations and boundary conditions

A welding current passes through the work-pieces and initiates the formation of a weld nugget at the faying (joining) surface. The effects of the liquid motion in the fused weld nugget are assumed to be negligible due to the short time and small size of the weld pool. In order to describe the thermal processes taking place in the material the three dimensional transient heat conduction equation was used:

$$\frac{1}{\alpha} \frac{\partial T}{\partial t} = \frac{\partial^2 T}{\partial x^2} + \frac{\partial^2 T}{\partial y^2} + \frac{\partial^2 T}{\partial z^2} + \frac{1}{k} g(x, y, z, t) \quad (1)$$

T is the temperature which is a function of position and time, g is the heat generation function, k is the thermal conductivity which depends on temperature and thus is also implicitly a function of position and time, α – thermal diffusivity, $\alpha = k/(\rho C_p)$.

It is convenient to introduce cylindrical coordinates to solve the problem. Assuming symmetry of the processes with respect to the electrode axis it is possible to reduce the number of dimensions to two without loss of generality. The heat conduction equation in cylindrical coordinates with symmetry with respect to the azimuthal angle is:

$$\frac{1}{\alpha} \frac{\partial T}{\partial t} = \frac{\partial^2 T}{\partial r^2} + \frac{\partial^2 T}{\partial z^2} + \frac{1}{r} \frac{\partial T}{\partial r} + \frac{1}{k} g(r, z, t), \quad (2)$$

for $r > 0$ and

$$\frac{1}{\alpha} \frac{\partial T}{\partial t} = 2 \frac{\partial^2 T}{\partial r^2} + \frac{\partial^2 T}{\partial z^2} + \frac{1}{k} g(r, z, t), \quad (3)$$

for $r = 0$,

using the property

$$\nabla^2 T = \frac{1}{r} \frac{\partial}{\partial r} \left(r \frac{\partial T}{\partial r} \right) + \frac{1}{r^2} \frac{\partial^2 T}{\partial \theta^2} + \frac{\partial^2 T}{\partial z^2}.$$

The r and z coordinates are represented in Fig. 4 together with boundary conditions.

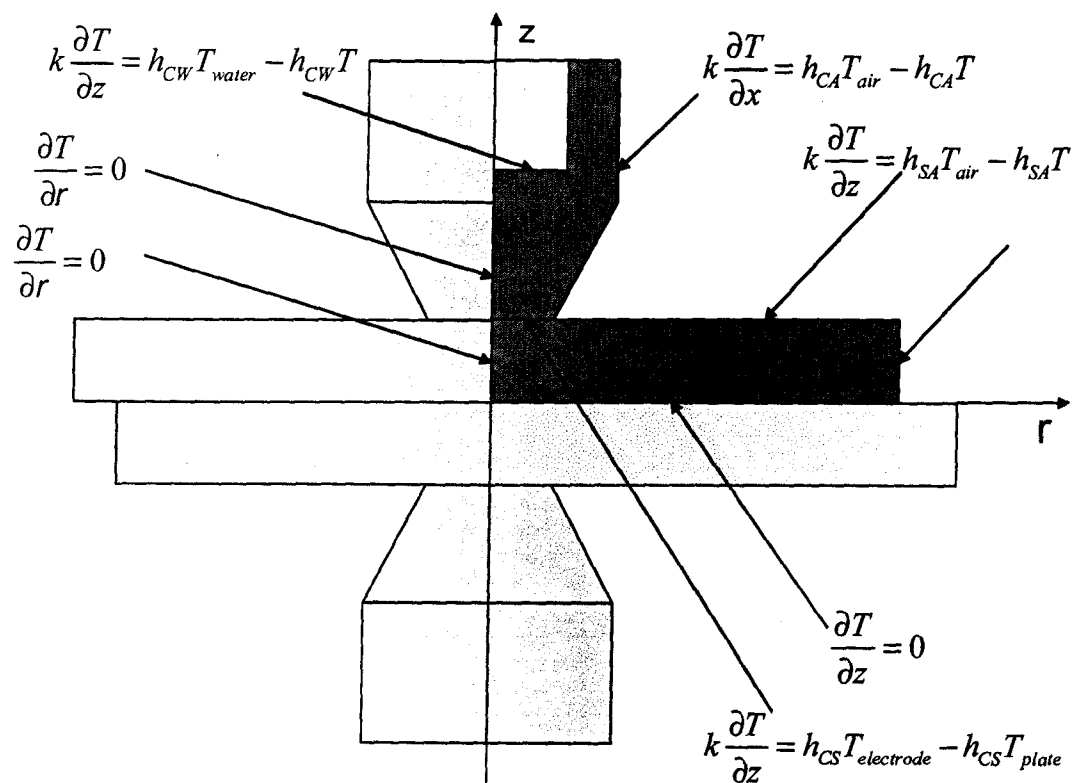


Figure 4. Thermal boundary conditions.

The symmetrical distribution of temperatures through the thickness of the material and along the interface enable to consider only one quarter of the setup (hatched area in Fig.4). Later, the obtained solution can be reflected to restore the whole four-quadrant picture. The temperature of the cooling water is considered to be constant. Symmetry with respect to r and z axis is described by setting the gradient of temperature on the symmetry lines to zero. Heat transfer coefficients h are the characteristics of the particular material (see Table 1).

The heat generation function g can be represented by two components, contact and volume heat generations.

$$g_{volume} = \frac{I^2 R(T)}{V} = \rho(T) \frac{I^2}{A^2}, \quad \left[\frac{W}{m^3} \right], \quad T = T(r, z, t).$$

A is the cross-sectional area of the electrode tip, $\rho(T)$ is the resistivity of steel as a function of temperature. I is the current passing through the system. The current varies sinusoidally with a frequency of 60 Hz as $I = I_0 \sin(2\pi \cdot t/T)$, $T = 1/60$ s.

The same formula is used to model the contact heat generation taking into account the thickness of generation zone d :

$$g_{contact} = \frac{I^2 \cdot R(T)}{A \cdot d}, \quad \left[\frac{W}{m^3} \right]$$

Here R is the total contact resistance between two plates and $A \cdot d$ is the volume which generates this heat. Fig. 5 shows a schematic view of near-contact volume.

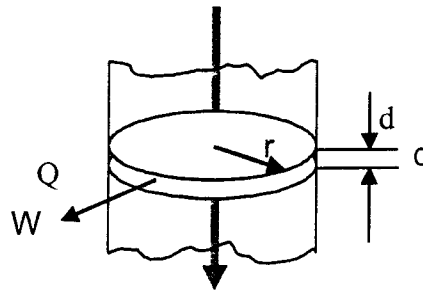


Figure 5. The contact heat generation. Contact area is considered as a small volume (disc) of thickness d and radius r .

The electrical resistivity of mild steel as a function of temperature is defined in the broad range of temperatures, Fig. 6.

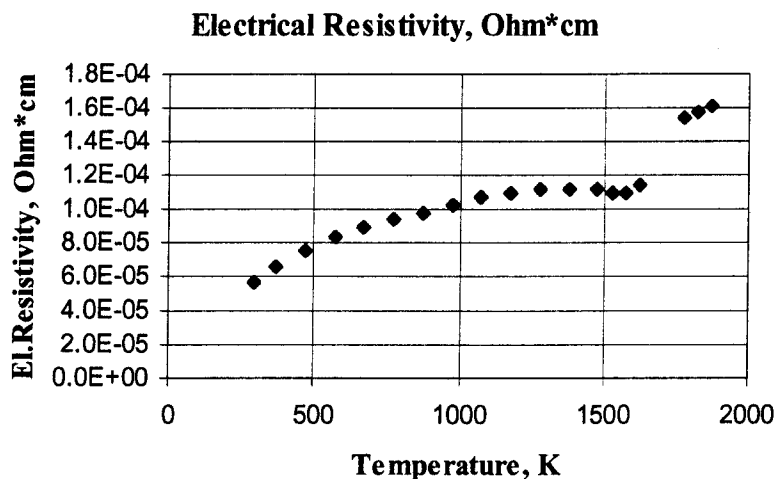


Figure 6. Electrical resistivity of mild steel. Courtesy of [2].

To approximate the contact resistance, it is assumed that it is a linear function of temperature and disappears at the melting point. Other estimations suggest that it drops exponentially as the welding time proceeds up to few semi cycles. In this model

$$R_{CONTACT} = R_0 \left(\frac{T_M - T}{T_M - T_0} \right) \quad (6)$$

has been used. T_M is the melting temperature, T_0 is the initial temperature, and R_0 - static contact resistance at the initial temperature.

Melting could cause some problems in the calculations, as in this process, latent heat of fusion should be taken into account. To avoid this problem the enthalpy method described by Crank [3] can be used. Instead of working in terms of temperature, one can define the enthalpy function which describes the total heat content of the system [4]. Enthalpy is a state function equal to the total energy of the system including PV-work done against the surroundings at constant pressure during a process or change of the system. With equation 8 relating the enthalpy with temperature the full effect of the phase change can be modeled without needing to know the exact size of the phase change

region. This fact makes numerical solutions relatively easy. The heat conduction equation in terms of internal energy can be used for both liquid and solid matter of the setup. In cylindrical coordinates it is represented by

$$\frac{\partial H}{\partial t} = \frac{1}{r} \frac{\partial}{\partial r} \left(rk \frac{\partial T}{\partial r} \right) + \frac{\partial}{\partial z} \left(k \frac{\partial T}{\partial z} \right) + g(r, z, t), \quad \left[\frac{\text{J}}{\text{cm}^3 \text{s}} \right] \quad (7)$$

The energy-temperature relationship is defined by (see Voller and Cross [5])

$$H = \begin{cases} \rho(T)C_p(T)T, & T \leq T_M - \varepsilon \\ H|_{T_M - \varepsilon} + \frac{(\rho_s + \rho_l)LHF(T - T_M + \varepsilon)}{4\varepsilon}, & T_M - \varepsilon < T < T_M + \varepsilon \\ H|_{T_M + \varepsilon} + \rho(T)C_p(T)(T - T_M - \varepsilon), & T \geq T_M + \varepsilon \end{cases} \quad (8)$$

The enthalpy is a discontinuous function at the melting point of the pure material as shown in Fig. 7. In order to smooth it to ease computer calculations it was represented by three parts in three temperature ranges. $\varepsilon = 10\text{K}$ is a reasonable number for numerical modeling.

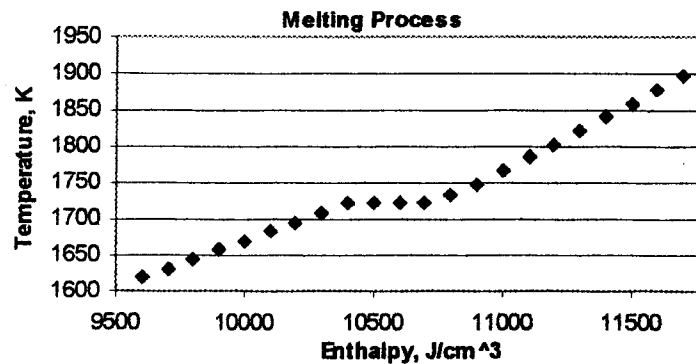


Figure 7. Enthalpy-temperature graph for steel.

A summary of the coefficients and material properties used in calculations is shown in Table 1. All dynamic (temperature dependent) material properties are presented in Appendix A.

Steel latent heat of fusion, J/kg	LHF	1.14×10^5
Heat transfer coefficient steel-air, W/m ² /K	h_{SA}	50
Heat transfer coefficient steel-copper, W/m ² /K	h_{CS}	40000
Heat transfer coefficient copper-air, W/m ² /K	h_{CA}	55
Heat transfer coefficient copper-water, W/m ² /K	h_{CW}	20000
Initial temperature, K	T_0	300
Separation gap at faying surface, m	d	5×10^{-5}
Steel melting temperature, K	T_s	1723
Copper melting temperature, K	T_c	1357
Static contact resistance (steel-steel interface), Ω	R_0	2.5×10^{-4}

Table 1. Summary of the coefficients and material properties.

3. Finite Difference Modeling

The method

The main idea of the finite difference method is to represent partial differential equation in terms of discrete values of the function whose solution is sought. Using the Taylor expansion one can represent any derivative of a smooth function in terms of low order derivatives. The Taylor series expansion is described by

$$f(x_0 - \Delta x) = f(x_0) - \left. \frac{df}{dx} \right|_0 \Delta x + \left. \frac{d^2 f}{dx^2} \right|_0 \frac{(\Delta x)^2}{2!} - \left. \frac{d^3 f}{dx^3} \right|_0 \frac{(\Delta x)^3}{3!} + \dots \quad (9)$$

$$f(x_0 + \Delta x) = f(x_0) + \left. \frac{df}{dx} \right|_0 \Delta x + \left. \frac{d^2 f}{dx^2} \right|_0 \frac{(\Delta x)^2}{2!} + \left. \frac{d^3 f}{dx^3} \right|_0 \frac{(\Delta x)^3}{3!} + \dots \quad (10)$$

These two expressions form the basis for developing the finite difference approximation for the first derivative about x_0 . Rearranging equations (9) and (10), the forward and backward finite difference approximations for the first derivative become

$$\left. \frac{df}{dx} \right|_0 = \frac{f(x_0 + \Delta x) - f(x_0)}{\Delta x} + O(\Delta x); \quad (\text{forward}) \quad (11)$$

$$\left. \frac{df}{dx} \right|_0 = \frac{f(x_0) - f(x_0 - \Delta x)}{\Delta x} + O(\Delta x). \quad (\text{backward}) \quad (12)$$

Introducing letter notation i for point x_0 , $i+1$ for $x_0 + \Delta x$, $i-1$ for $x_0 - \Delta x$, and h for Δx and combining (11) and (12) one obtains the central formula for the first derivative

$$f'_i = \frac{f_{i+1} - f_{i-1}}{2h} + O(h^2) \quad (\text{central}) \quad (13)$$

This representation is one order higher approximation (order 2), which is usually enough for modeling. Adding equations (9) and (10) one easily obtains expression for the second derivative

$$f''_i = \frac{f_{i-1} - 2f_i + f_{i+1}}{h^2} + O(h^2) \quad (\text{central}) \quad (14)$$

The Simple explicit method

This is one of the most frequently used techniques of the FDM. The main idea of the method is calculation of the unknown function value at time level $n+1$, T_i^{n+1} , from three known previous time level function values T_{i-1}^n , T_i^n , T_{i+1}^n . See Fig. 8.

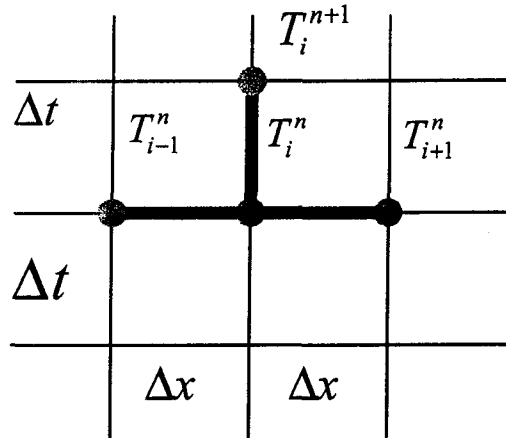


Figure 8. Finite-difference space-time representation with one space dimension using the simple explicit method.

The one dimensional parabolic equation

$$\alpha \frac{\partial^2 T(x,t)}{\partial x^2} = \frac{\partial T(x,t)}{\partial t} \quad (15)$$

in the region $0 < x < L$, $t > 0$ will be solved by replacing the second-order derivative by the second-order central difference formula and the time derivative by the first-order forward difference formula. The equation becomes

$$\frac{T_i^{n+1} - T_i^n}{\Delta t} = \alpha \frac{T_{i-1}^n - 2T_i^n + T_{i+1}^n}{(\Delta x)^2} + O[\Delta t, (\Delta x)^2]. \quad (16)$$

Equation (16) is called the simple explicit form of the finite difference approximation of the diffusion equation (15) because it involves only one unknown T_i^{n+1} .

Because of the azimuthal angle symmetry, the two-dimensional problem can be solved using just one independent coordinate r . The two-dimensional picture can be restored by turning the solution along the r -coordinate around the origin, see Fig. 9.

The two-dimensional picture of finite-difference scheme will be the similar except that it will use five points at given time level to calculate one point at the next level, as seen in Fig. 10.

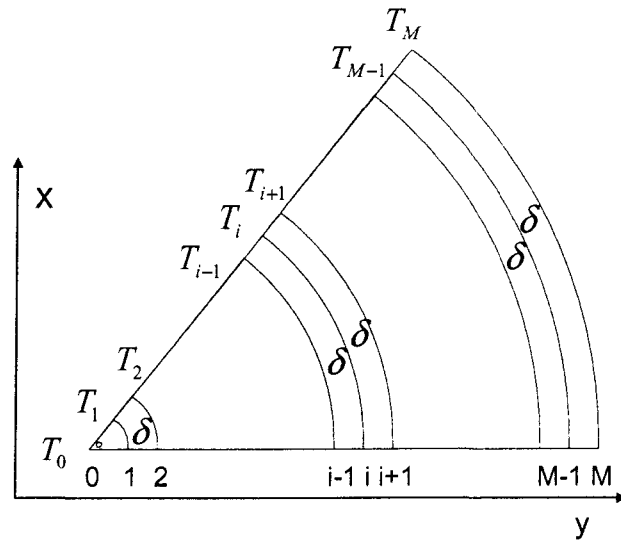


Figure 9. Nomenclature for finite-difference representation for azimuthal symmetry.

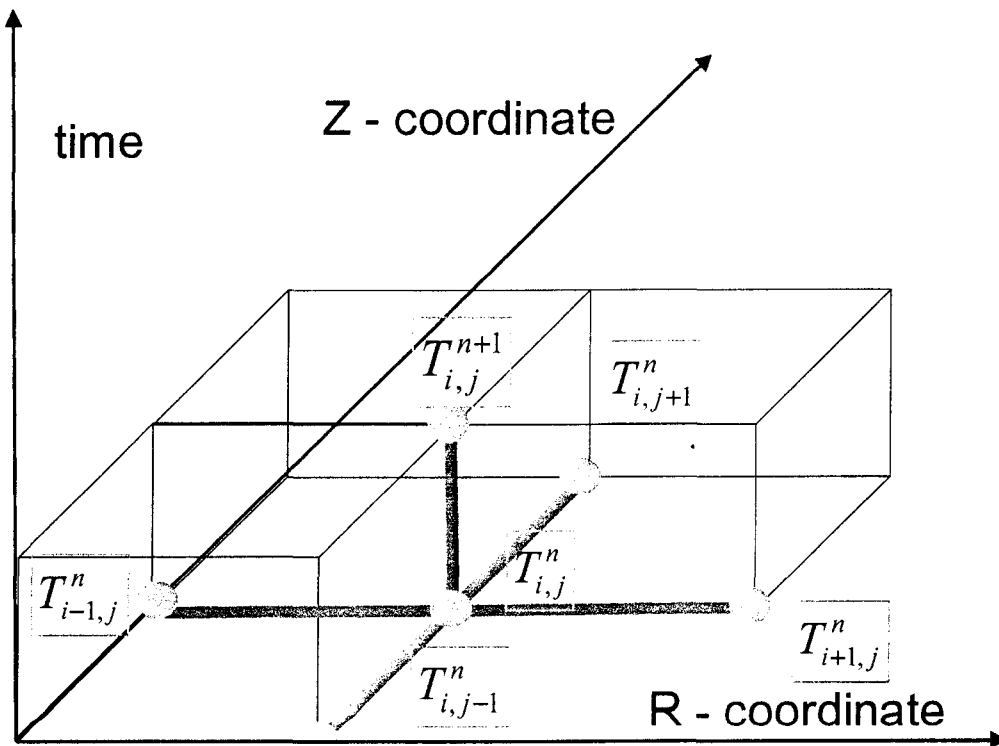


Figure 10. Finite-difference space-time representation of the two space dimensions using the simple explicit method.

Two-dimensional equation will have the form

$$\frac{T_{i,j}^{n+1} - T_{i,j}^n}{\Delta t} = \alpha \left[\frac{T_{i-1,j}^n - 2T_{i,j}^n + T_{i+1,j}^n}{(\Delta x)^2} + \frac{T_{i,j-1}^n - 2T_{i,j}^n + T_{i,j+1}^n}{(\Delta z)^2} + \frac{1}{k} g_{i,j}^n \right] \quad (17)$$

The Enthalpy Approach

Using this method the governing equation in cylindrical coordinates

$$\frac{\partial^2 T}{\partial r^2} + \frac{\partial^2 T}{\partial z^2} + \frac{1}{r} \frac{\partial T}{\partial r} + \frac{1}{k} g(r, z, t) = \frac{1}{\alpha} \frac{\partial T}{\partial t}$$

can be written as

$$H_{i,j}^{n+1} = H_{i,j}^n + \frac{k\Delta t}{\delta^2} \left(1 - \frac{1}{2i} \right) T_{i-1,j}^n + \frac{4k\Delta t}{\delta^2} T_{i,j}^n + \frac{k\Delta t}{\delta^2} \left(1 + \frac{1}{2i} \right) T_{i+1,j}^n + \frac{k\Delta t}{\delta^2} T_{i,j-1}^n + \frac{k\Delta t}{\delta^2} T_{i,j+1}^n + \Delta t g_{i,j}^n \quad (18)$$

H is the total internal energy, ρ is the density, k - is thermal conductivity. All three are the functions of temperature. i is the number of the node in the grid; Δt is the time step; δ is the grid step; δ was the same for both z and r coordinates. This formula is valid only within the volume, and is not valid on the boundaries.

After H value at given time step has been determined, equation 8 is used to calculate the temperature. This approach avoids the problem of the discontinuous process of melting.

At the grid points Along the z axis where $i = 0$ and $r = 0$, equation 3 becomes

$$H_{0,j}^{n+1} = H_{0,j}^n - 6 \frac{k\Delta t}{\delta^2} T_{0,j}^n + 4 \frac{k\Delta t}{\delta^2} T_{1,j}^n + \frac{k\Delta t}{\delta^2} T_{0,j-1}^n + \frac{k\Delta t}{\delta^2} T_{0,j+1}^n + \Delta t g_{0,j}^n \quad (19)$$

Here the symmetry property $dT/dr = 0$ at $r = 0$ or $T_{-1,j}^n = T_{+1,j}^n$ has been applied.

At the right boundary, $i = M$, the heat transfer from steel into the air takes place. At this boundary the heat processes should be described by

$$H_{M,j}^{n+1} = H_{M,j}^n + \frac{2k\Delta t}{\delta^2} T_{M-1,j}^n - \left(\frac{4k\Delta t}{\delta^2} + \frac{2\Delta th_{SA}}{\delta} \left(1 + \frac{1}{2i} \right) \right) T_{M,j}^n + \frac{k\Delta t}{\delta^2} T_{M,j-1}^n + \frac{k\Delta t}{\delta^2} T_{M,j+1}^n + \frac{2\Delta th_{SA}}{\delta} \left(1 + \frac{1}{2i} \right) T_{Air} + \Delta tg_{M,j}^n \quad (20)$$

The same formula is applied for the copper part of the system, with the replacement of h_{SA} by h_{CA} . The steel-steel and copper-water horizontal interfaces are handled in the same way. Since the steel-copper interface is not symmetrical, it should be treated separately. Using the boundary conditions $k \frac{\partial T}{\partial x} = h_{CS} (T_{COPPER} - T_{i,N})$ from the steel side and

$$k \frac{\partial T}{\partial x} = h_{CS} (T_{i,N+1} - T_{STEEL}) \text{ from the copper side, two boundary equations were}$$

obtained:

$$H_{i,N}^{n+1} = H_{i,N}^n + \frac{k\Delta t}{\delta^2} \left(1 - \frac{1}{2i} \right) T_{i-1,N}^n - \left(\frac{4k\Delta t}{\delta^2} + \frac{2\Delta th_{CS}}{\delta} \right) T_{i,N}^n + \frac{k\Delta t}{\delta^2} \left(1 - \frac{1}{2i} \right) T_{i+1,N}^n + \frac{2k\Delta t}{\delta^2} T_{i,N-1}^n + \frac{2\Delta th_{CS}}{\delta} T_{i,N+1}^C + \Delta tg_{i,N}^n \quad (21)$$

$$\rho C_p T_{i,N+1}^{n+1} = \frac{k\Delta t}{\delta^2} \left(1 - \frac{1}{2i} \right) T_{i-1,N+1}^n + \left(\rho C_p - \frac{4k\Delta t}{\delta^2} - \frac{2\Delta th_{CS}}{\delta} \right) T_{i,N+1}^n + \frac{k\Delta t}{\delta^2} \left(1 - \frac{1}{2i} \right) T_{i+1,N+1}^n + \frac{2k\Delta t}{\delta^2} T_{i,N+2}^n + \frac{2\Delta th_{CS}}{\delta} T_{i,N}^{ST} \quad (22)$$

For the copper part one can work entirely in terms of temperature, because the electrode temperatures are far from the melting point of copper. The material constants for steel are used in equation 21 and those for copper are used in equation 22. Equation

22 does not contain a heat generation term as it was assumed that the heat generation in copper and on the steel-copper interface are negligible compared to that of steel and the steel-steel interface.

Every spatial point on a corner should also be treated separately but there are no principal difficulties in derivations.

Heat Generation

Heat generation function is described by two separate terms

$$g_{i,j}^n = g_{i,j}^{contact} + g_{i,j}^{volume}; \quad g_{i,j}^{contact} \neq 0 \text{ only for } j=0 \quad (23)$$

$$g_{i,j}^{contact} = \frac{I^2 R^{CONTACT} (T_{i,j}^n)}{\pi R^2 d}, \quad g_{i,j}^{volume} = \frac{I^2 \rho (T_{i,j}^n)}{\pi^2 R^4} \quad (24)$$

It was assumed that electrical current flows and generates heat only under the contact surface of radius R_t , the radius of the electrode tip. See Figs. 11, 12.

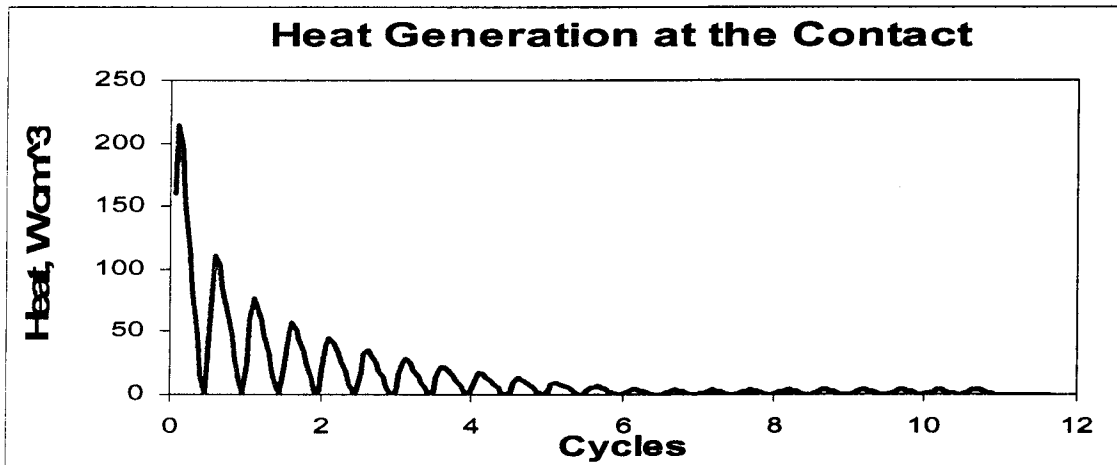


Figure 11. Heat generation at the steel-steel interface during welding. It has the highest value at the beginning and vanishes at the melting point of steel.

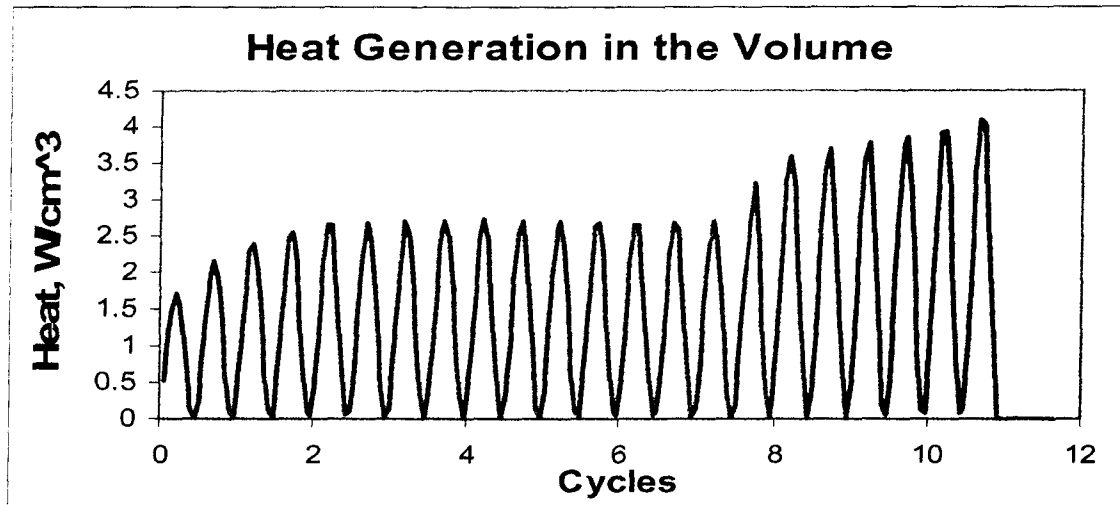


Figure 12. Heat generation in the steel plates during welding. It depends directly on the resistivity of steel, and the last depends on the temperature.

Stability of the Solution

The values of the time and coordinate steps in the explicit method are not arbitrary.

In order to have stable, non-oscillatory solution the steps should satisfy the inequality

$$0 < \frac{\alpha \Delta t}{(\Delta x)^2} \leq 0.5 \quad (25)$$

This stability criterion implies that, for given values α and Δx , the magnitude of the time step Δt cannot exceed the limit

$$\Delta t \leq \frac{(\Delta x)^2}{2\alpha}$$

The reason for this criterion comes from equation 16. If one leaves in the LHS only (n+1) time level, he gets

$$T_i^{n+1} = \left(1 - 2 \frac{\alpha \Delta t}{(\Delta x)^2} \right) T_i^n + \frac{\alpha \Delta t}{(\Delta x)^2} T_{i-1}^n + \frac{\alpha \Delta t}{(\Delta x)^2} T_{i+1}^n \quad (26)$$

For illustration purposes let $T_{i-1,j}^n = 0$, $T_{i+1,j}^n = 0$ and $T_i^n = 1$. Now we try to calculate T at the time level (n+1) using (26). The physical situation requires that the

temperature T_i^{n+1} can not go below the temperature of the two neighboring nodes, 0°C . An examination of (26) reveals that a negative value in parenthesis violates such a requirement. Thus to obtain meaningful results the solution must satisfy (25).

Fig. 13 illustrates effects of the value of r on the stability of finite-difference solution with the explicit method. For mesh size 0.0075 cm the maximum allowed time step for materials and temperature ranges in use is 60 microseconds.

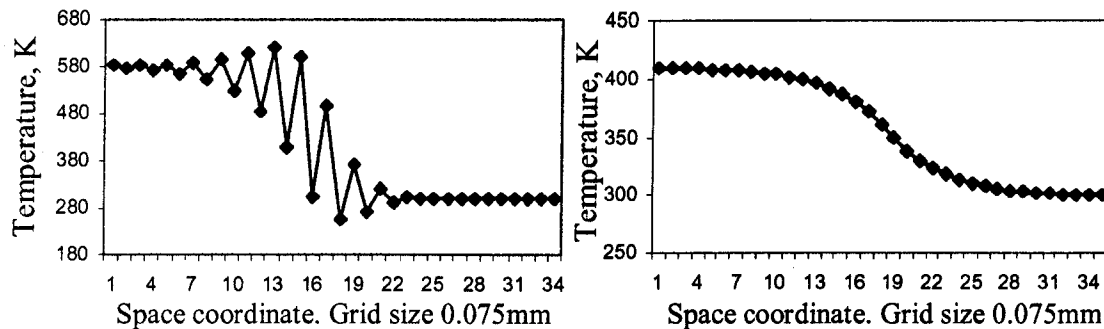


Figure 13. Stability considerations. The left figure shows an unstable solution with $\Delta t = 73 \mu\text{s}$. When $\Delta t = 56 \mu\text{s}$ – less than $60 \mu\text{s}$, the temperature distribution varies smoothly.

Summary of the assumptions used in the model

1. A cylindrical coordinate system was selected. The portions of coupon affected by heat and immediate adjacent areas of the unaffected base metal have been represented by a disk of 10 mm. Geometrical dependency is reduced to two dimensions, $T = T(r, z, \phi)$.
2. The temperatures of the cooling water and air are considered to be constant.
3. Natural convection is the dominant mechanism on the outer surfaces.
4. The material properties – density, thermal conductivity, resistivity, specific heat are considered as functions of temperature.

5. The contact resistance at the faying interface is the linear function of temperature and it vanishes at melting point.
6. Since the tip surfaces of the copper electrodes are easily deformed, and also polished before welding, the copper-steel interface resistances are neglected.
7. Since the metal undergoes a phase change, a latent heat of fusion evolves which is assumed to be isothermally absorbed.
8. The initial temperature of the metal is the ambient temperature, 300 K.
9. The symmetry with respect to z and x axis allowed to formulate the mathematical problem only for the quarter of the system as shown in figure 4, and to use obtained temperature distributions in one quadrant to restore the full picture.

Figs. 14-19 demonstrate the welding process lasting 11 cycles. Corresponding temperature scale is given in Fig. 20.

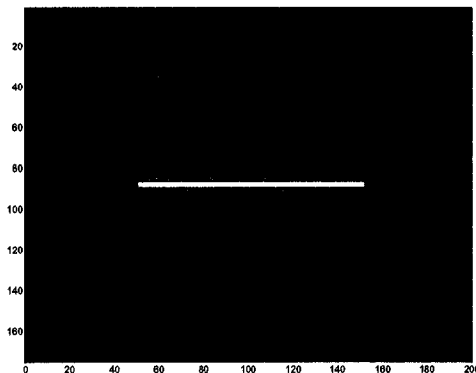


Fig. 14. First welding cycle

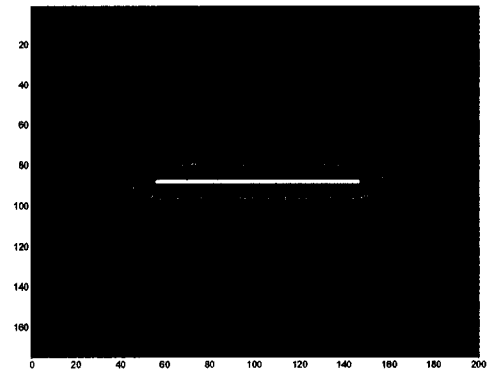


Fig. 15. Second welding cycle

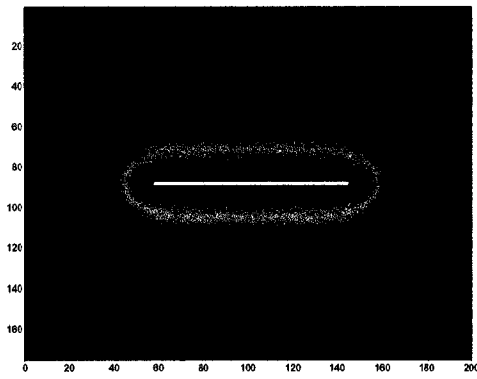


Fig. 16. Third welding cycle

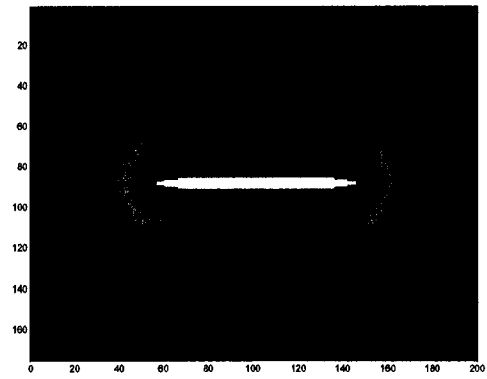


Fig. 17. Sixth welding cycle

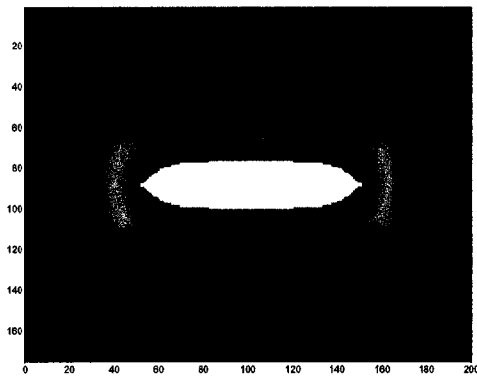


Fig. 18. Ninth welding cycle

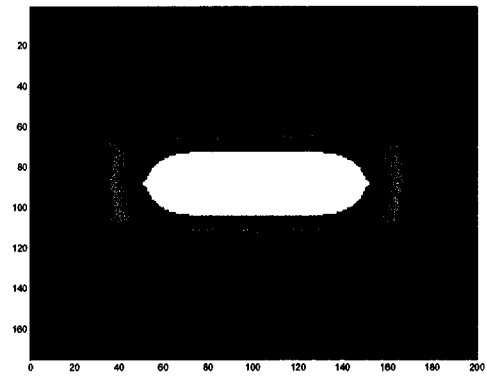


Fig. 19. End of cycle 11.

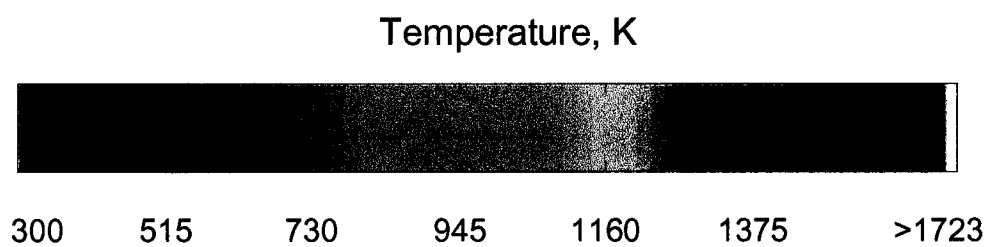


Figure 20. Temperature scale.

Figs. 21-23 describe temperature distributions in some indicative points during the process of welding.

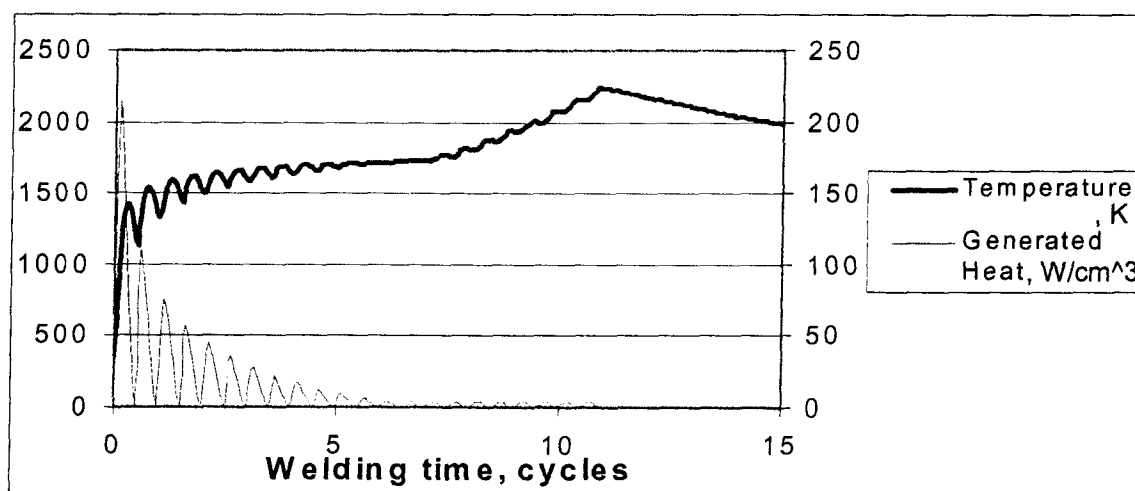


Figure 21 . Temperature at the faying surface. Because of high rate of heat generation in the beginning, temperature rises rapidly. But then the rate decreases because contact resistance drops. When the metal melts, the resistivity increases and heat generation rises again.

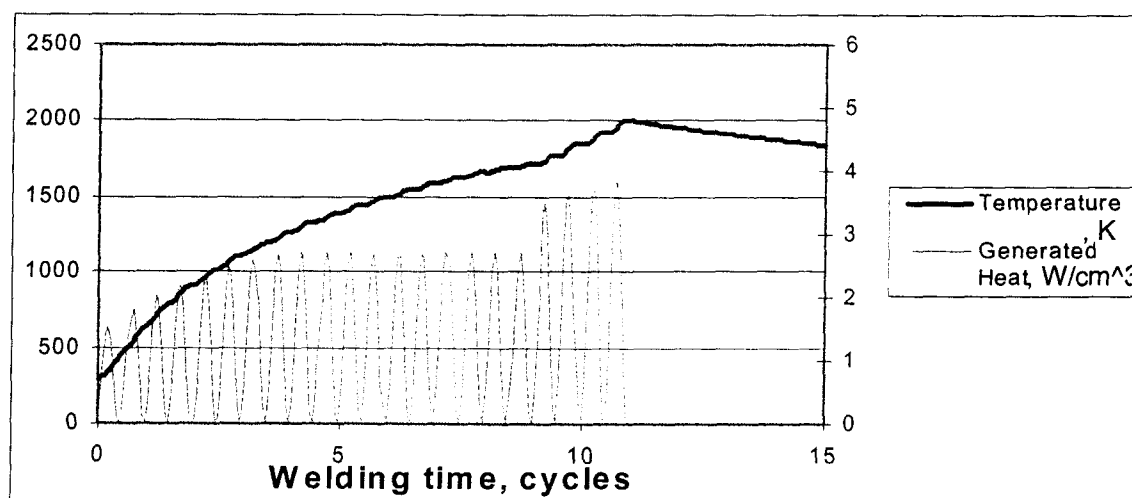


Figure 22. Temperature in the middle of the steel plate under the electrode. The picture is much more smooth because given point is removed far enough from the faying surface. Melting still occurs there but at later time.

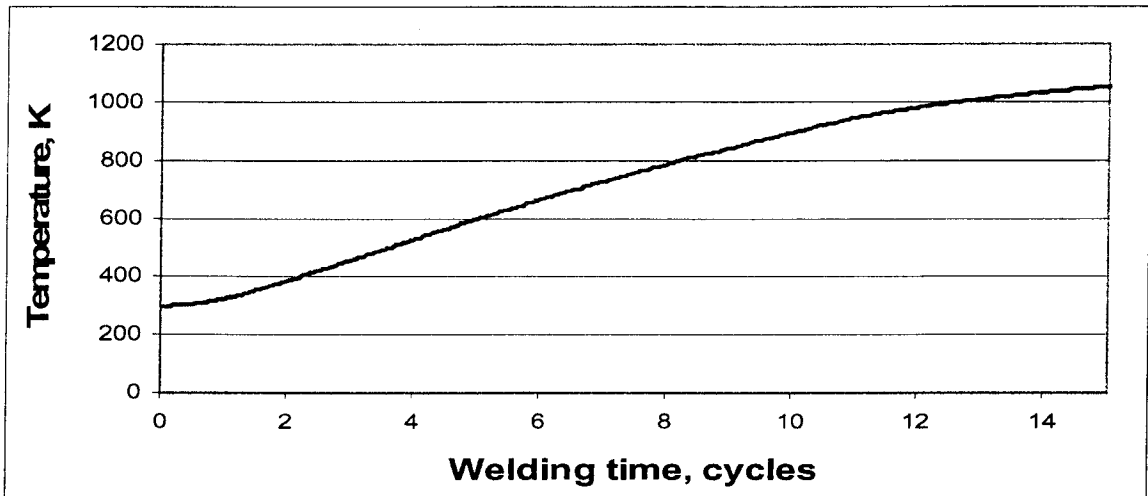


Figure 23. Temperature at the steel-copper contact surface. At the end of the eleventh cycle temperature is less than 1000°C . It continues to rise slightly even after turning off the current because electrode works like heat removing element.

Figs. 24, 25, 26, 27 show the temperature distributions in the weld along the central axis. The upper parts of each figure were obtained by rescaling the 2D weld pictures from Figs. 14, 17, 18, 19. These plots demonstrate the thickness of the molten area.

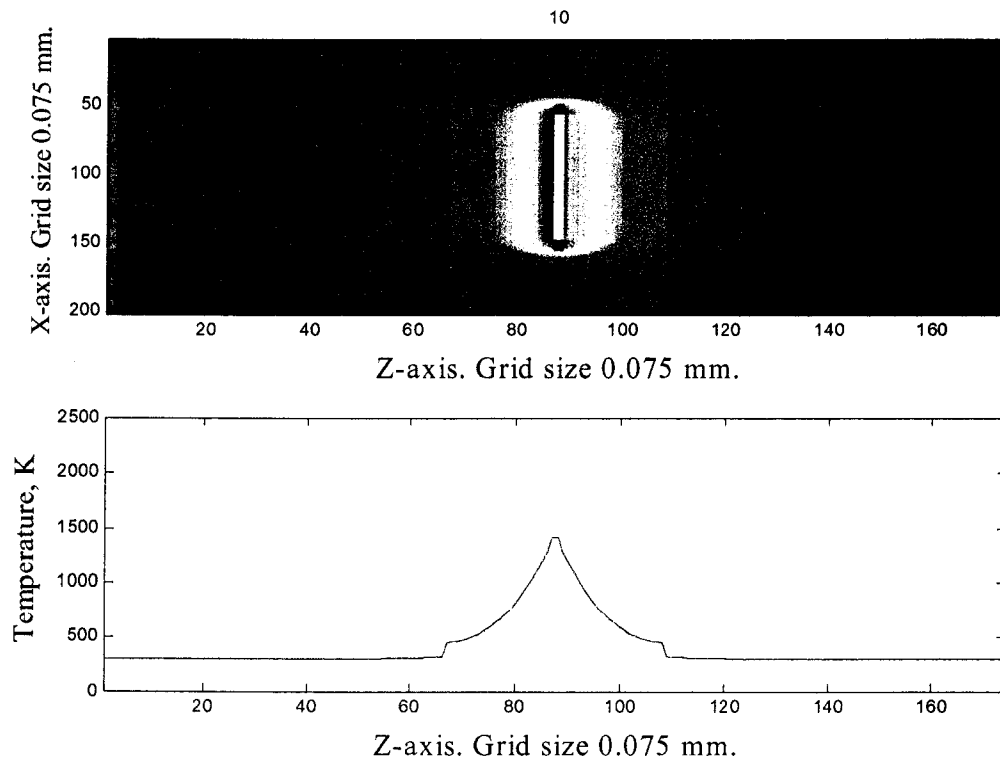


Figure 24. View of the weld and temperature distribution along central axis; first cycle.

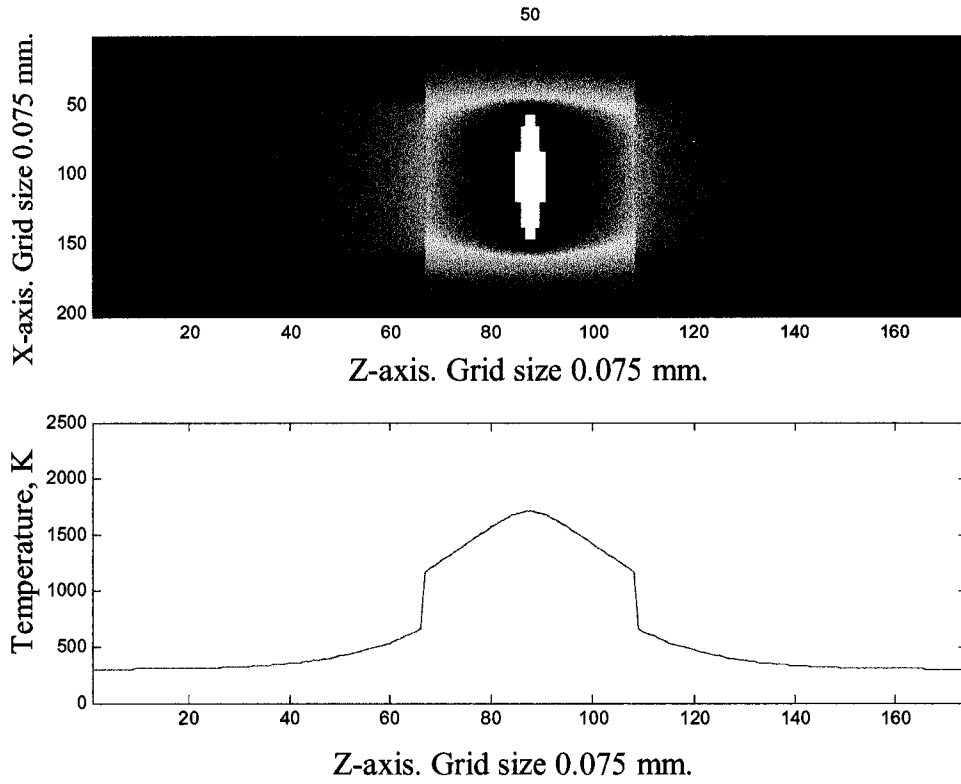


Figure 25. View of the weld and temperature distribution along central axis; 6th cycle.

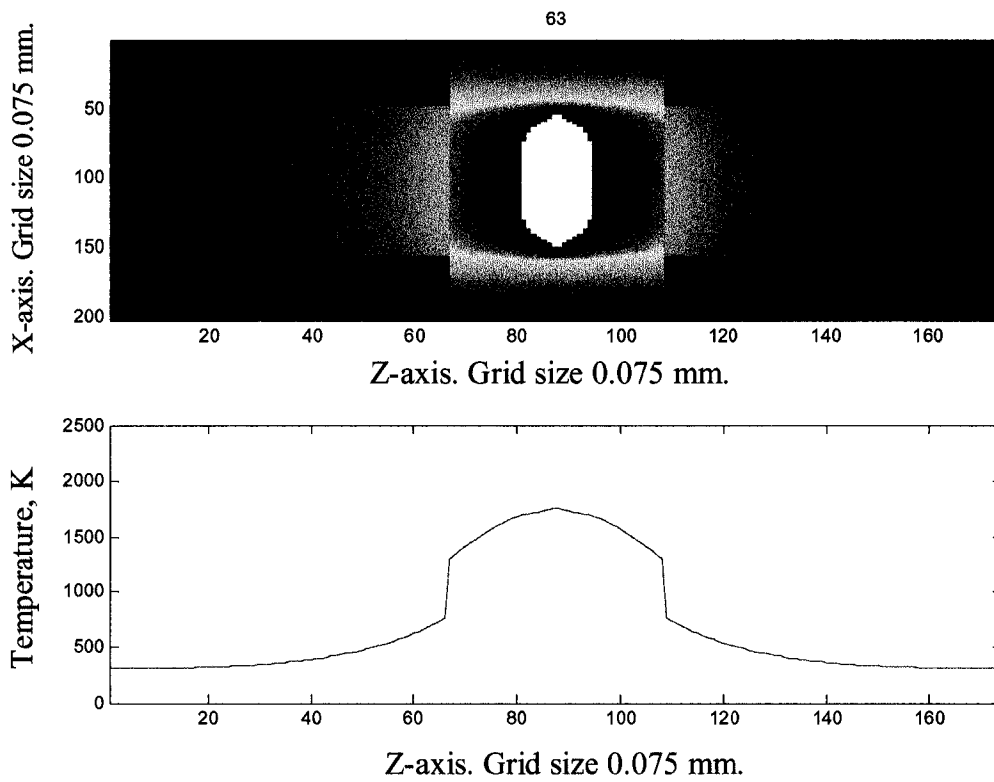


Figure 26. View of the weld and temperature distribution along central axis; 8th cycle.

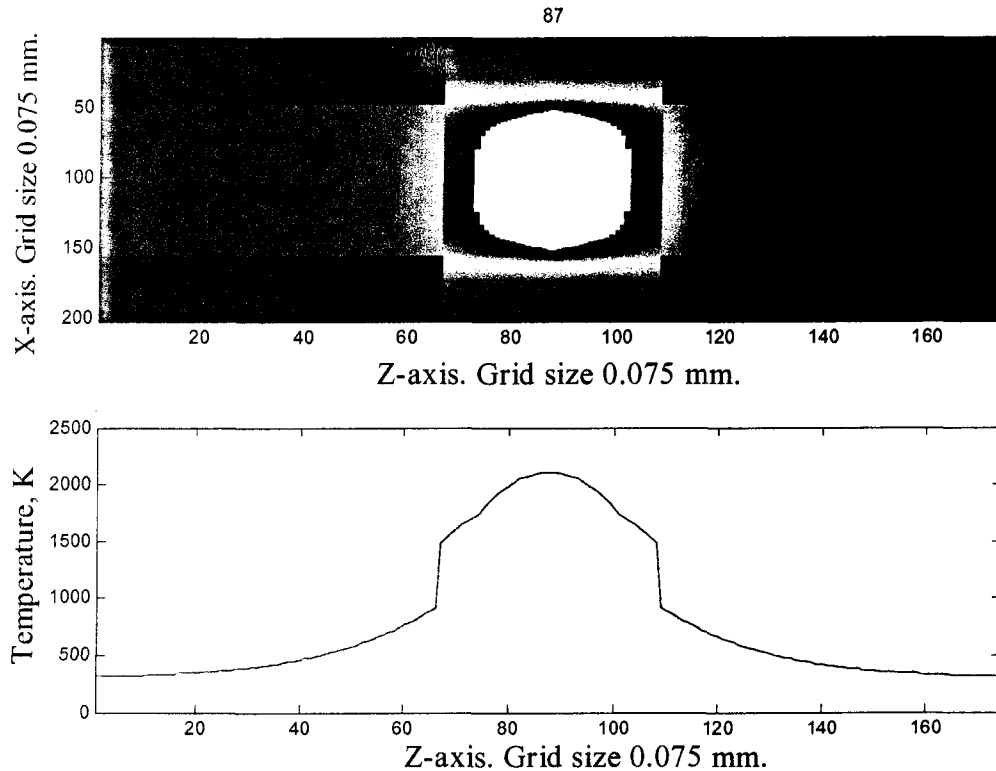


Figure 27. View of the weld and temperature distribution along central axis; 11th cycle.

The obtained simulations were compared with the experimental results. A series of spot welds has been produced using 1.5 mm thick galvanized mild steel plates. The welding regime was used in accordance with the one used in the model: 14.5 kA, 12 cycles (60 Hz), 7.9 mm tip diameter, 900 lbs electrode force. The set was peeled to check the diameter of the nugget. The nugget diameters in the given experiment lied in the range of 6.1-6.8 mm. The calculated nugget diameter is 7.4 mm. The difference arises from the uncertainty of peel test: the weld edges visible on the metallographic sections can be easily broken during peeling of the sample thus reducing the measured size.

The shape of the nugget was compared with the metallographic sections of the real welds. Figs. 28, 29 show the photos of sections of welds and the numerical model results. The real welds happen to be non-symmetric, with uneven edges, etc. These imperfections

are caused by various side effects that usually arise in welding. Among them are misalignment of tips, angle problem (when the electrodes are tilted with respect to their primary axis), tip wearing. All of them play some role in introducing uncertainties in weld production process. These effects were not taken into account during calculations because of the uniqueness of every imperfection on every weld gun. The model has shown the ideal, imperfection-free, case and has revealed the general features of dynamic temperature distribution during welding process.

The comparison with experiment confirms the correctness of calculations and enables to use the model as the basis for the further modeling of acoustic wave propagation in given media.

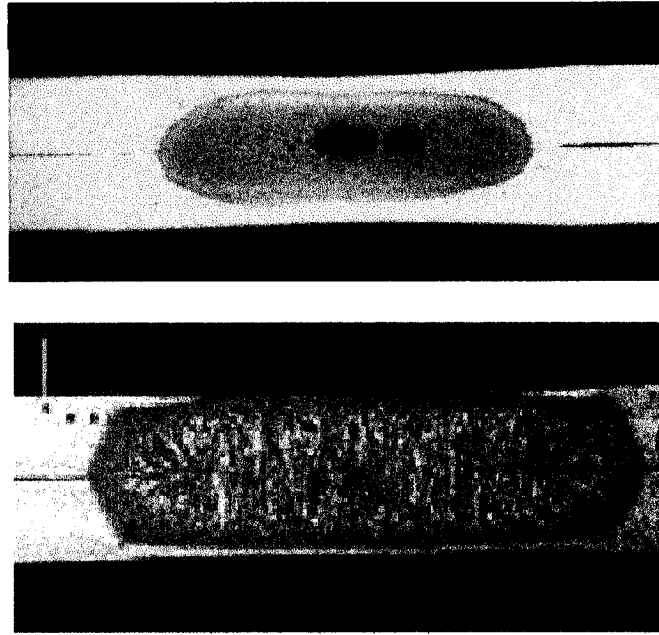


Figure 28. Metallographic sections of the spot welds.

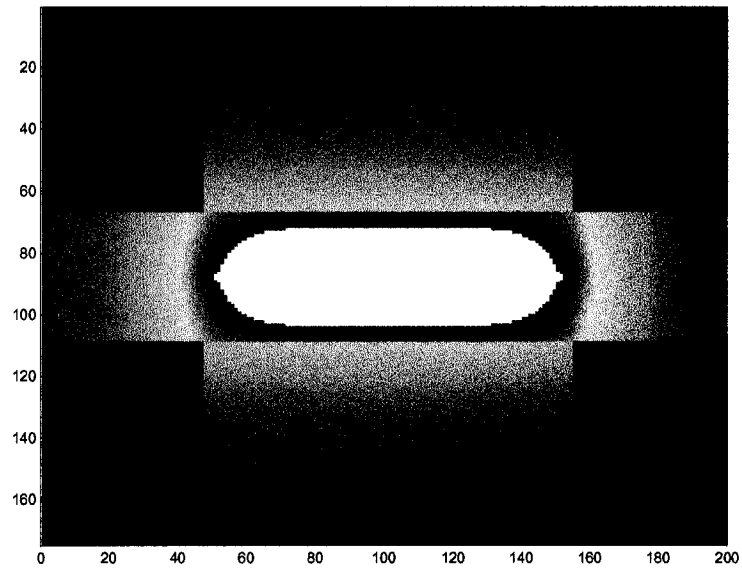


Figure 29. Spot weld shape, the numerical simulation.

4. Analytic 1D model

Introduction

In this part an attempt to make analytical model of temperature distributions in spot weld has been taken. There has been made an assumption that the majority of heat flow takes place along the central axis of the setup. The numerical model shows that the heat loss into the steel plates affects only peripheral parts of liquid steel pool (white area on Fig. 30, upper part). It makes the left and right parts of the nugget round and form some kind of a lens. The acoustic wave propagation won't be affected much by this side curves. In the first approximation the solid-liquid interfaces can be considered as plane. Possible distortion of the through transmitted and reflected wave will have very small effect on the propagation time.

The one-dimensional model will take into account heat generation at the steel-steel contact and in the steel volume and heat losses into the electrodes. Heat losses into the sides of steel plates and into the ambient will be neglected. As long as the system is symmetric with respect to the steel-steel interface, only one half of the setup will be considered.

Fig. 31 shows 2D picture of the spot weld system. The white line depicts the part to be modeled in 1D approach. The final system consists of two one-dimensional bars, steel and copper, in thermal contact. The steel bar starts at the point $z = 0$ and contacts copper one at $z = z_0$. At $z = L$ the copper bar contacts the cooling water of the constant temperature. The heat is generated in the volume of steel part between $z = 0$ and $z = z_0$.

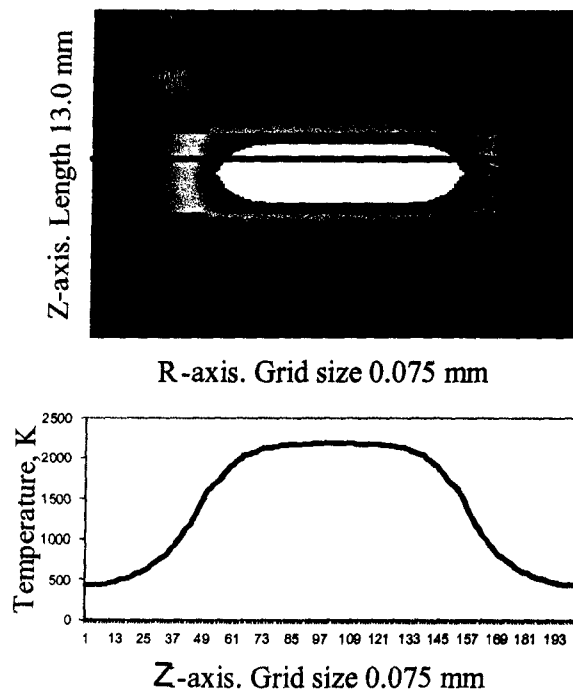


Figure 30. Temperature profile (lower part) in the spot weld along horizontal line in the upper part.

At $z = 0$ the boundary condition $dT/dz = G_{CONT}$ models contact heat generation. The generated heat increases the temperature of steel part and goes through the steel-copper contact to the copper part, heating it as well and finally dissipates into the cooling water.

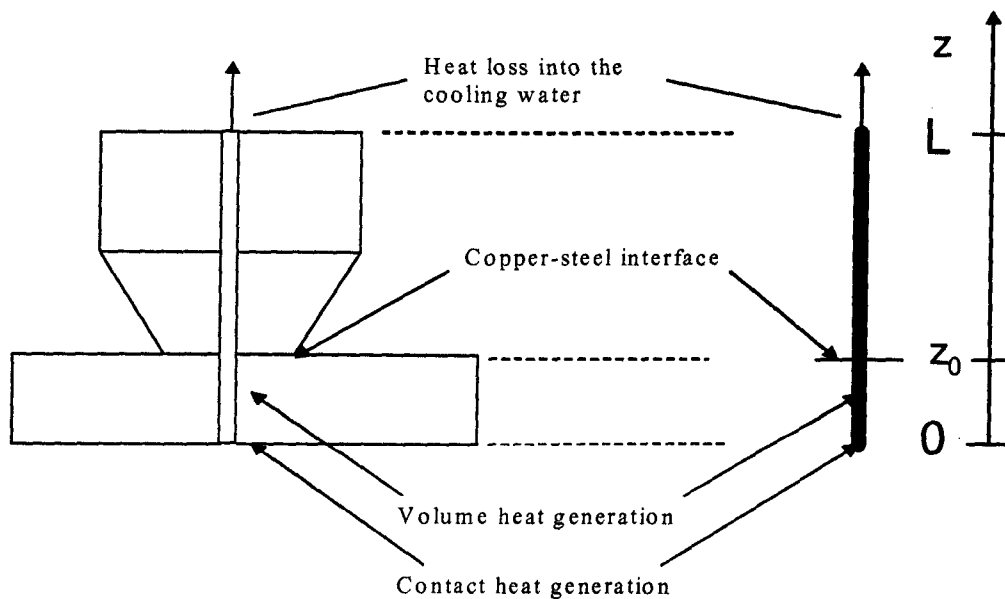


Figure 31. Schematic view of the 2D setup and its 1D analog.

Mathematical Formulation

The system consists of two materials stacked with each other; $k_1, k_2, \alpha_1, \alpha_2$ are thermal conductivity and thermal diffusivity of the materials; h_{CS} is the heat transfer coefficient at the steel-copper interface and h_{CW} is the heat transfer coefficient at the outer boundary ($z = L$). $T_1(z, t)$ and $T_2(z, t)$ are the temperature distributions within steel and copper layers respectively. The mathematical formulation of the problem consists of finding $T_i(z, t)$ for all i ($i = 1, 2$) which satisfy the transient inhomogeneous 1D heat equations

$$\begin{cases} \alpha_1 \frac{\partial^2 T_1}{\partial z^2} + \frac{\alpha_1}{k_1} g(z, t) = \frac{\partial T_1}{\partial t} & \text{for steel} \\ \alpha_2 \frac{\partial^2 T_2}{\partial z^2} = \frac{\partial T_2}{\partial t} & \text{for copper} \end{cases} \quad (1)$$

Boundary and matching conditions take the form

$$\begin{aligned} \text{BC: } \frac{\partial T_1(0, t)}{\partial z} &= g_{\text{CONTACT}}(t) & k_2 \frac{\partial T_2(L, t)}{\partial z} &= h_{CW}(T_{\text{water}} - T_{\text{copper}}(L, t)) \\ \text{MC: } k_1 \frac{\partial T_1(z_0, t)}{\partial z} &= k_2 \frac{\partial T_2(z_0, t)}{\partial z} & k_1 \frac{\partial T(z_0, t)}{\partial z} &= h_{CS}(T_2(z_0, t) - T_1(z_0, t)) \end{aligned}$$

Where T is the temperature as the function of time and coordinates, k is the thermal conductivity. Heat transfer coefficients h are the characteristics of the particular material (see Table 1). The volume heat generation $g(x, t)$ characterizes Joule effect due to the current passing through the material of known resistivity.

$$\begin{aligned} g_{\text{volume}}(z, t) &= \rho(T) \frac{I^2}{A^2} \\ g_{\text{volume}}(z, t) &= hT_1(z, t) \end{aligned}$$

Linear approximation of the temperature dependence of resistivity makes $g(x, t)$ a linear function of temperature, see Appendix D.

According to estimations the contact resistance can be well approximated by the exponential function of welding time. Contact resistance drops 3-5 times in the first few semi-cycles.

$$g_{contact}(t) = A \exp(-t / \tau) \quad \tau \text{ is about 5-6 semicycles}$$

A is initial heat generated due to the contact resistance at the very beginning of welding.

Plugging these approximations into (1) and into boundary conditions one obtains the final mathematical formulation of the problem

$$\begin{cases} \alpha_1 \frac{\partial^2 T_1(z, t)}{\partial z^2} + h T_1(z, t) = \frac{\partial T_1(z, t)}{\partial t} \\ \alpha_2 \frac{\partial^2 T_2(z, t)}{\partial z^2} = \frac{\partial T_2(z, t)}{\partial t} \end{cases} \quad (2)$$

$$\frac{\partial T_1(0, t)}{\partial z} = A \exp(-t / \tau) \quad k_2 \frac{\partial T_2(L, t)}{\partial z} = h_{CW} (T_{water} - T_2(L, t))$$

$$k_1 \frac{\partial T_1(z_0, t)}{\partial z} = k_2 \frac{\partial T_2(z_0, t)}{\partial z} \quad k_1 \frac{\partial T_1(z_0, t)}{\partial z} = h_{CS} (T_2(z_0, t) - T_1(z_0, t)) \quad (3)$$

General Solution

To solve the problem it is to be reformulated to the easier form. The system of inhomogeneous equations with *inhomogeneous* boundary conditions should be transformed into the system of inhomogeneous equations (sometimes more complicated) but with *homogeneous* boundary conditions. The general solutions of the system can be presented in the form

$$\begin{aligned}
T_1(z,t) &= \varphi_1(z)f_1(t) + \psi_1(z)f_2(t) + u_1(z,t) \\
T_2(z,t) &= \varphi_2(z)f_1(t) + \psi_2(z)f_2(t) + u_2(z,t) \\
f_1(t) &= A \exp(-t/\tau), \\
f_2(t) &= T_{water}
\end{aligned}$$

Application of boundary and matching conditions yields

$$\begin{aligned}
T_1(z,t) &= (c_1z + c_2)A \exp(-t/\tau) + u_1(z,t) \\
T_2(z,t) &= (c_3z + c_4)A \exp(-t/\tau) + u_2(z,t)
\end{aligned} \tag{4}$$

$$c_1 = 1, \quad c_2 = \frac{-k_1}{h} + \frac{k_1}{k_2}z_0 - \frac{k_1}{h_3} - \frac{k_1}{k_2}L - z_0, \quad c_3 = \frac{k_1}{k_2}, \quad c_4 = -\frac{k_1}{h_3} - \frac{k_1}{k_2}L \tag{5}$$

Temperature of water was taken 0 for simplicity. Substitution of (4) in (2) yields

$$\begin{cases}
\alpha_1 \frac{\partial^2 u_1(z,t)}{\partial z^2} + hu_1(z,t) = \frac{\partial u_1(z,t)}{\partial t} - A(c_1z + c_2)(h + 1/\tau) \exp(-t/\tau) \\
\alpha_2 \frac{\partial^2 u_2(z,t)}{\partial z^2} = \frac{\partial u_2(z,t)}{\partial t} - \frac{A}{\tau}(c_3z + c_4) \exp(-t/\tau)
\end{cases} \tag{6}$$

$$\frac{\partial u_1(0,t)}{\partial z} = 0 \quad k_2 \frac{\partial u_2(L,t)}{\partial z} = -h_3 u_2(L,t) \tag{7}$$

$$k_1 \frac{\partial u_1(z_0,t)}{\partial z} = k_2 \frac{\partial u_2(z_0,t)}{\partial z} \quad k_1 \frac{\partial u_1(z_0,t)}{\partial z} = h(u_2(z_0,t) - u_1(z_0,t))$$

Now (6) and (7) represent system of inhomogeneous equations with homogeneous boundary conditions. To solve such a system one needs to solve a system of *homogeneous* equations with the same BC and to use the obtained set of eigenfunctions to expand original equations.

$$\begin{cases}
\alpha_1 \frac{\partial^2 u_1(z,t)}{\partial z^2} = \frac{\partial u_1(z,t)}{\partial t} \\
\alpha_2 \frac{\partial^2 u_2(z,t)}{\partial z^2} = \frac{\partial u_2(z,t)}{\partial t}
\end{cases} \tag{8}$$

Solutions of system (8) should provide eigenfunctions to form orthonormal basis. The last can be used to expand equations 6. Equations 8 belong to the class of regular Sturm-Liouville problems [10] of the form

$$L(f) = (rf')' + pf + \lambda \omega f = 0$$

Thus there is an orthonormal basis consisting of eigenfunctions.

Separation of variables provides

$$\begin{cases} X_1''(z) + \frac{\beta^2}{\alpha_1} X_1(z) = 0 & 0 < z < z_0 \\ X_2''(z) + \frac{\beta^2}{\alpha_2} X_2(z) = 0 & z_0 < z < L \end{cases} \quad (9)$$

$$\begin{cases} T_1'(t) + \beta^2 T_1(t) = 0 \\ T_2'(t) + \beta^2 T_2(t) = 0 \end{cases} \quad (10)$$

General solutions for X_1 and X_2 of (9) take the form

$$\begin{aligned} X_1(z) &= c_1 \sin\left(\frac{\beta}{\sqrt{\alpha_1}} z\right) + c_2 \cos\left(\frac{\beta}{\sqrt{\alpha_1}} z\right) \\ X_2(z) &= c_3 \sin\left(\frac{\beta}{\sqrt{\alpha_2}} z\right) + c_4 \cos\left(\frac{\beta}{\sqrt{\alpha_2}} z\right) \end{aligned} \quad \begin{aligned} c_1 = 0, c_3 = \alpha c_4 \text{ for convenience} \\ c_3 = c_4 \frac{k_2 \frac{\beta}{\sqrt{\alpha_2}} \tan\left(\frac{\beta}{\sqrt{\alpha_2}} L\right) - h_3}{k_2 \frac{\beta}{\sqrt{\alpha_2}} + h_3 \tan\left(\frac{\beta}{\sqrt{\alpha_2}} L\right)} \end{aligned}$$

Applying matching conditions we require a nonzero solution of this homogeneous system for c_2 and c_4 so that the determinant of the coefficients must vanish.

$$\begin{pmatrix} -k_1 \frac{\beta}{\sqrt{\alpha_1}} \sin\left(\frac{\beta}{\sqrt{\alpha_1}} z_0\right) + h \cos\left(\frac{\beta}{\sqrt{\alpha_1}} z_0\right) & -h \sigma \sin\left(\frac{\beta}{\sqrt{\alpha_2}} z_0\right) + h \cos\left(\frac{\beta}{\sqrt{\alpha_2}} z_0\right) \\ -k_1 \frac{\beta}{\sqrt{\alpha_1}} \sin\left(\frac{\beta}{\sqrt{\alpha_1}} z_0\right) & -k_2 \sigma \frac{\beta}{\sqrt{\alpha_2}} \cos\left(\frac{\beta}{\sqrt{\alpha_2}} z_0\right) + \frac{\beta}{\sqrt{\alpha_2}} \sin\left(\frac{\beta}{\sqrt{\alpha_2}} z_0\right) \end{pmatrix} \begin{pmatrix} c_2 \\ c_4 \end{pmatrix} = \begin{pmatrix} 0 \\ 0 \end{pmatrix} \quad (11)$$

Equation of the determinant of (11) to zero gives transcendental equation to provide eigenvalues β for every eigenfunction.

$$|\Delta| = 0$$

This equation to be solved either graphically or numerically. Graphical representation of the solutions is shown on Fig. 32. These are the points of intersection of curves with line $y = 0$.

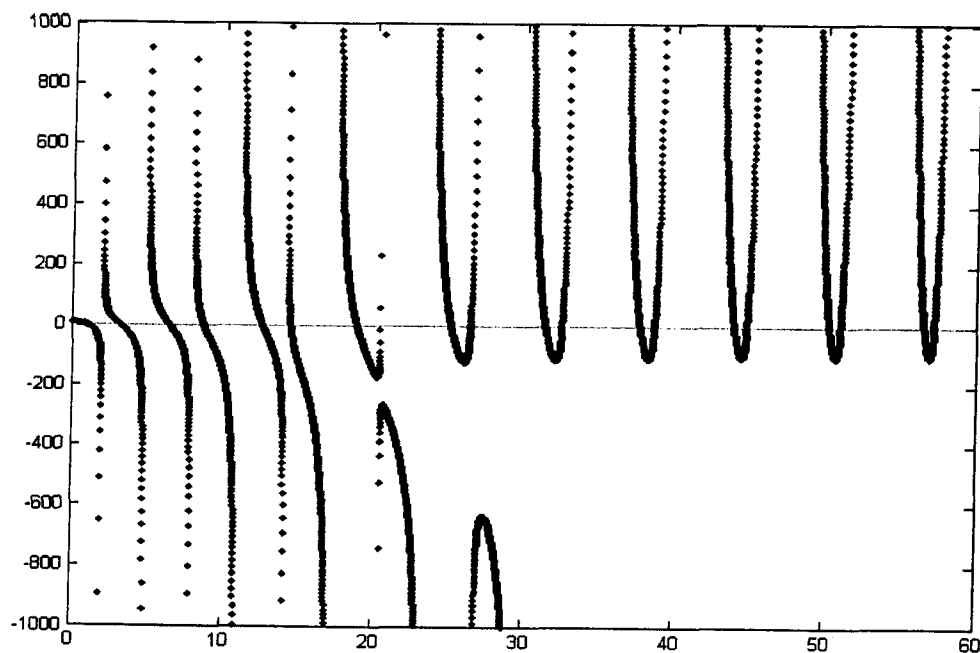


Figure 32. Graphical representation of the solutions of transcendental equation to provide eigenvalues for the solutions of the system of equations.

0.8508	3.1449	6.4336	8.7195	12.6433	14.5223	18.9011	20.4483	25.1715
--------	--------	--------	--------	---------	---------	---------	---------	---------

Table 2. First few eigenvalues, numerical solution.

Choosing coefficient c_2 to be $c_2 = -\frac{\sqrt{\alpha_1}}{k_1 \beta \sin(\beta z_0 / \sqrt{\alpha_1})}$, c_4 becomes

$$c_4 = \frac{\sqrt{\alpha_2}}{k_2 \beta \left(\sigma \cos\left(\frac{\beta}{\sqrt{\alpha_2}} z_0\right) - \sin\left(\frac{\beta}{\sqrt{\alpha_2}} z_0\right) \right)} \quad (12) \text{ and } (13)$$

$$\text{Norm takes the form } \|X^{(k)}\|^2 = \frac{k_1}{\alpha_1} \int_0^{z_0} X_1(z)^2 dz + \frac{k_2}{\alpha_2} \int_{z_0}^L X_2(z)^2 dz \quad (14)$$

The orthogonality of the set of eigenfunctions may be verified directly, and using (14), the set can be normalized. Using finite Fourier transform or separation of variables, the series representation for the solution $u(x, t)$ becomes

$$\begin{cases} u_1(z, t) = \sum_{n=1}^{\infty} c_n \exp(-\beta^2 t) X_{1n}(z) \\ u_2(z, t) = \sum_{n=1}^{\infty} c_n \exp(-\beta^2 t) X_{2n}(z) \end{cases} \quad (15)$$

with eigenfunctions of the form

$$\begin{cases} X_1(z) = c_2 \cos\left(\frac{\beta}{\sqrt{\alpha_1}} z\right) \\ X_2(z) = \sigma c_4 \sin\left(\frac{\beta}{\sqrt{\alpha_2}} z\right) + c_4 \cos\left(\frac{\beta}{\sqrt{\alpha_2}} z\right) \end{cases} \quad (16)$$

$$\text{and } c_n = \frac{1}{\|X^{(k)}\|^2} \left(\frac{k_1}{\alpha_1} \int_0^{z_0} u_1(z, 0) X_1(z) dz + \frac{k_2}{\alpha_2} \int_{z_0}^L u_2(z, 0) X_2(z) dz \right) = \frac{1}{\|X^{(k)}\|^2} (c_n^1 + c_n^2) \quad (17)$$

Expansion of equations of system (6) gives coefficient

$$\begin{aligned} c_n &= \frac{1}{\|X^{(k)}\|^2} c_n^1 \left(\exp(\text{heat} \cdot t - \beta^2 t) + \frac{\psi_1(\exp(-t/\tau) - \exp(-\beta^2 t))}{\beta^2 - 1/\tau} \right) + \\ &\frac{1}{\|X^{(k)}\|^2} c_n^{2\sin} \left(\exp(-\beta^2 t) + \frac{\psi_2(\exp(-t/\tau) - \exp(-\beta^2 t))}{\beta^2 - 1/\tau} \right) + \\ &\frac{1}{\|X^{(k)}\|^2} c_n^{2\cos} \left(\exp(-\beta^2 t) + \frac{\psi_3(\exp(-t/\tau) - \exp(-\beta^2 t))}{\beta^2 - 1/\tau} \right) \end{aligned}$$

The description of abbreviated notation of some variables is given in Appendix B.

Finally one gets the solution of the system in terms of T_1 and T_2 for two bars.

$$u(z, t) = \begin{cases} u_1(z, t) = \sum_1^{\infty} c_n X_{1n}(z) \\ u_2(z, t) = \sum_1^{\infty} c_n X_{2n}(z) \end{cases} \quad (18)$$

And substituting $u_i(x, t)$ into equations for $T_i(x, t)$ one gets

$$T(z, t) = \begin{cases} T_1(z, t) = (c_1 z + c_2) A \exp(-t / \tau) + u_1(z, t) \\ T_2(z, t) = (c_3 z + c_4) A \exp(-t / \tau) + u_2(z, t) \end{cases} \quad (19)$$

which is the solution of the 1D problem of heat generation and propagation in two bars

- in thermal contact with each other,
- with internal heat generation and heat supply from the left end and,
- Newtonian cooling from the right end.

To check the obtained results the first calculations have been performed in the absence of active heat sources. Two bars at approximately 100°C and 50°C are put together. The left end of the left bar is thermally insulated; the right end of right bar can loose heat into the ambient having 0° C temperature. The cooling process is shown in Fig. 33. The initial temperature should be represented by two straight lines at 100 and 50 degrees. The red line on the figure (initial temperature) is not straight because finite number of eigenfunctions has been used to represent it. The computer program used first 18 eigenvalues and corresponding eigenfunctions. The increase of the number of eigenfunctions reduces the error but significantly increases calculation time. 18th eigenvalues contribute less than 0.2% to the temperature values for all but the first step.

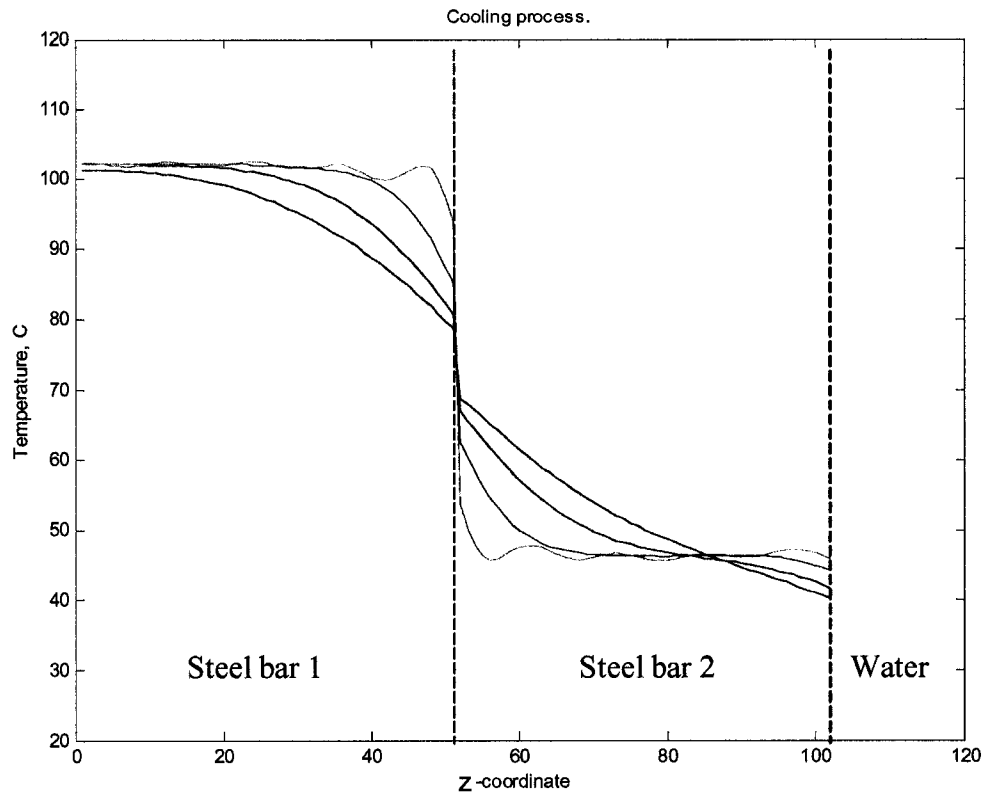


Figure 33. Heat redistribution. Two steel bars initially at temperatures 103°C and 47°C experience redistribution of heat inside of them. Red line is initial temperature, green – next time step. Time increment is 20 ms. Heat transfer coefficient at steel-steel contact is $40,000 \text{ W/m}^2/\text{K}$, at steel-water contact is $10,000 \text{ W/m}^2/\text{K}$. Length of each bar 0.5 mm.

The simulation uses two heat sources – from the left end of the left bar and inside of the whole length of the left bar. The first one characterizes contact heat generation, the second one – heat generation due to resistivity of steel volume. Heat generation in the right bar (copper) is ignored as its resistivity is about ten times lower than that of the steel. Fig. 34 shows heat distribution in steel and copper bars at the final welding cycle. The analytic model did not take into account the melting process. Heat capacity of steel was considered as constant, independent of temperature. This representation is rougher than the numerical approach. But even in this case the calculations resemble the pictures obtained using finite difference approximation.

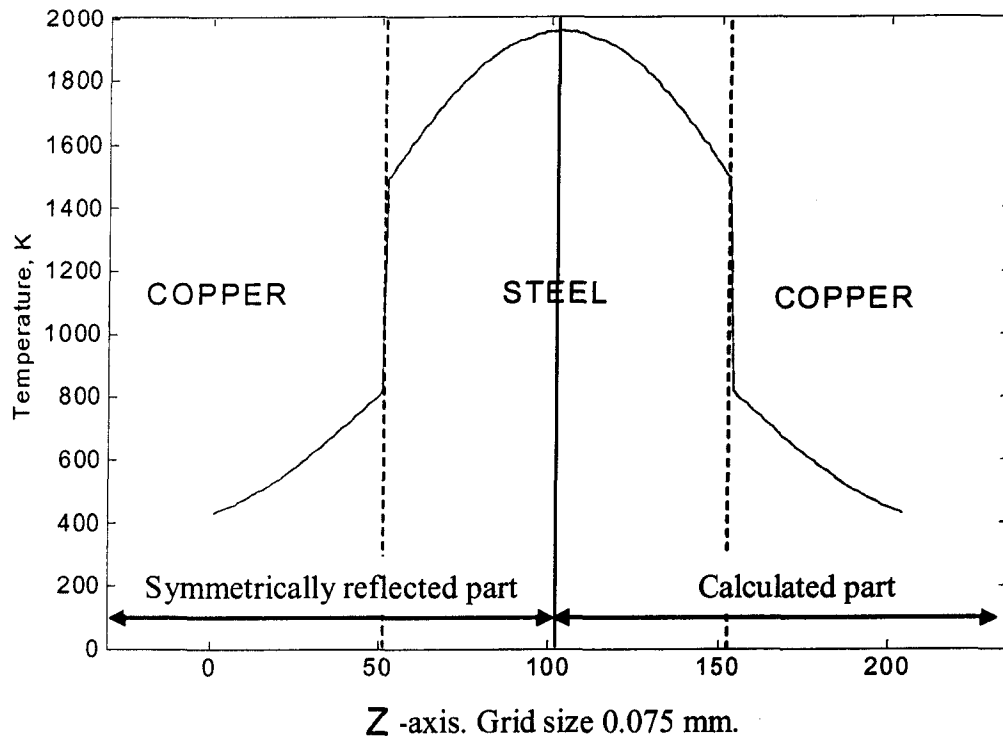


Figure 34. Temperature profile in copper-steel-copper setup at final moment of welding. Analytical approach.

Fig. 35 shows comparison of numerical and analytical solutions. The molten region can be easily seen on numerical curve. Analytical model did not count for it. The difference in temperature distributions arises from several facts reflected in Table 3. The advantage of analytical approach is the possibility to instantly obtain solution at any time in any point. Numerical one requires go through all time steps from the beginning, calculating temperature in every point, and slowly approaching the moment of interest. The longer the period from the beginning of the process the more computer resources and time are required to get an answer.

Approach:	Numerical	Analytical
<i>Contact resistance model</i>	Straight line: max in the beginning, zero at melting point.	Exponential decay. Even behind the melting point the model has some contact resistance.
<i>Heat capacity</i>	Temperature dependent, includes latent heat of fusion.	Constant value, taken as average over the temperature range 300-2000K
<i>Thermal conductivity</i>	Temperature dependent	Constant value, taken as average over the temperature range 300-2000K
<i>Dimensionality</i>	Three dimensions. Used two because of cylindrical symmetry.	One dimension.

Table 3. Comparison of analytical and numerical approaches.

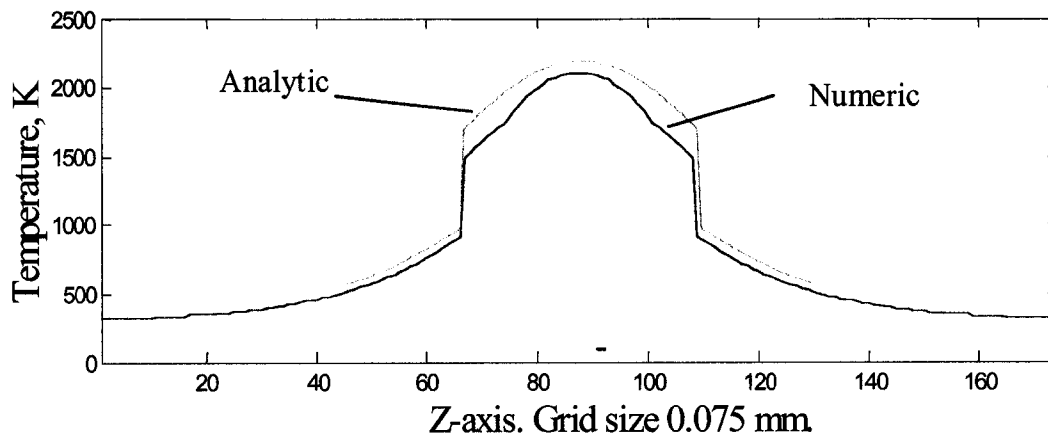


Figure 35. Graphical comparison of numeric and analytic results.

The obtained temperature distributions can now be used for calculations of material properties in every point of setup at every time step. These material property fields define the inhomogeneity of the media. The model of wave propagation will require these properties in order to simulate behavior of the wave at every moment of welding.

References

1. Von W. Kurz, B. Lux. *Lokalisierung der Erstarrungsfront beim Stranggießen von Stahl*.
2. Auburn University's Materials Processing Center.
3. Crank, J. *Free and Moving Boundary Problems*. Clarendon Press, Oxford, United Kingdom, Chap. 6, 1984.
4. P.S. Wei, C.Y. Ho. *Axisymmetric Nugget Growth During Resistance Spot Welding*. Journal of Heat Transfer, May 1990.
5. Voller, V., and Cross, M. *Accurate Solutions of Moving Boundary Problems Using the Enthalpy Methods*. Int. J. Heat Mass Transfer, Vol. 24, 1981, pp. 545-556.
6. M. Necati Ozisik. *Finite Difference Methods in Heat Transfer*. Boca Raton: CRC Press, 1994.
7. K.P. Bentley et al. *Temperature Distributions in Spot Welds*. British Welding Journal, December, 1963.
8. J.A. Greenwood. *Temperatures in Spot Welding*. British Welding Journal, June, 1961.
9. Z. Han et al. *Resistance Spot Welding: A Heat Transfer Study*. Welding Research Supplement, September 1989.
10. Gerald B. Folland. *Fourier Analysis and Its Applications*. Brooks/Cole Publishing Company, 1992.
11. Erich Zauderer. *Partial Differential Equations of Applied Mathematics*. New York [N.Y.]; Toronto [Ont.]: Wiley, 1983.
12. Tyn Myint U. *Partial Differential Equations for Scientists and Engineers*. New York: North Holland, 1987.
13. Ritger, Paul D. *Differential Equations With Applications*. New York: McGraw-Hill, 1968.
14. Ernesto Gutierrez-Miravete. *Heat Conduction in Composite Materials*. Web notes at http://www.rh.edu/~ernesto/C_S2002/CHT/notes/s14/s14.html.
15. Earl D. Rainville. *Elementary Differential Equations*. New York: Macmillan, 1952.

CHAPTER IV

Wave Propagation in a Spot Weld

1. Introduction

In the previous chapter the temperature distribution in the spot weld has been obtained. It is possible to recalculate this temperature field into the material properties fields. That is, temperature gradient creates gradients of mass density, Lamé constants and all other temperature dependent properties. Having the inhomogeneity profile of the media it is necessary now to predict the behavior of the wave in such a system. The most important features to verify are the time of flight of the signal and the possibility to use reflected signal for weld inspection.

The obtained picture of the spot weld temperature distributions enables to make some assumptions which will be helpful in the future calculations. First assumption is that the steel-liquid-steel interfaces are parallel to the other interfaces except for the lateral areas. In other words we have normal incidence of the wave. It can be well seen from the thermal simulation pictures. Second, having the main beam of the signal well concentrated around the central axis (see Appendix C) it is possible to claim that the majority of the signal passes through the central, flat, part of the solid-liquid interface. Thus, in the first approximation it is expected that the one-dimensional model could provide reliable picture of wave propagation in the setup. In other words, the curvatures of the weld do not provide much distortion to the signal features we try to model.

The first part of the chapter considers the analytical approach to the wave behavior in linearly inhomogeneous media. The second part deals with numerical model of wave propagation in the setup using assumptions much closer to the experimental reality.

As it was already mentioned, the temperature gradient in the media creates the gradients of material properties thus making the media inhomogeneous. The wave propagation in such a media can not be described by common sine and cosine (or complex exponential) wave function. The problem is that the inhomogeneity of the Lamé constants and mass density changes the equation of motion of vibrating media as follows.

$$\nabla \cdot \mathbf{T} = \rho \frac{\partial^2 \mathbf{u}}{\partial t^2} - \mathbf{F} \quad (1)$$

is the translational equation of motion derived using the Second Newton's Law.

\mathbf{T} is the stress tensor describing the forces acting on the surface of the oscillating particle in the medium, \mathbf{u} is the displacement of this particle from its equilibrium position. The problem will be considered in the absence of external forces ($\mathbf{F} = 0$).

The stress tensor can be described in terms of material properties (Lamé constants) and strain tensor. The last characterizes the displacement of the particle in space.

$$T_{ik} = \lambda(\varepsilon_{11} + \varepsilon_{22} + \varepsilon_{33})\delta_{ik} + 2\mu\varepsilon_{ik} \quad (2)$$

Here

$$\varepsilon_{ik} = \frac{1}{2} \left(\frac{\partial u_i}{\partial x_k} + \frac{\partial u_k}{\partial x_i} \right), \quad i = 1,2,3, \quad k = 1,2,3. \quad (3)$$

is the strain tensor.

If one considers the one-dimensional problem in z coordinate the \mathbf{T} will take the form

$$T_{ik} = T_{zz} = (\lambda + 2\mu) \frac{\partial u_3}{\partial x_3} = (\lambda + 2\mu) \frac{\partial u}{\partial z} \quad (4)$$

In inhomogeneous media $(\lambda + 2\mu)$ will become coordinate dependent, $f(z)$.

Equation of motion takes the form

$$\frac{\partial}{\partial z} \left(f(z) \frac{\partial u}{\partial z} \right) = \rho \frac{\partial^2 u}{\partial t^2}, \quad \text{or} \quad \frac{\partial f(z)}{\partial z} \frac{\partial u}{\partial z} + f(z) \frac{\partial^2 u}{\partial z^2} = \rho \frac{\partial^2 u}{\partial t^2} \quad (5)$$

The last equation differs from 1D wave equation by extra term which is responsible for coordinate dependence of Lamé constants. Figs. 1 and 2 show temperature distributions in spot weld. To avoid the discontinuity in calculations, it is possible to consider steel and copper parts separately and achieve satisfactory linear approximation within each material (Figs. 3, 4). See Appendix D for approximation analysis.

In analytical approach there was used above mentioned linear approximation of material properties: $f(z) = az + b$. Numerical model will deal with more challenging problem of tracking the exact shape of material property profile in the setup.

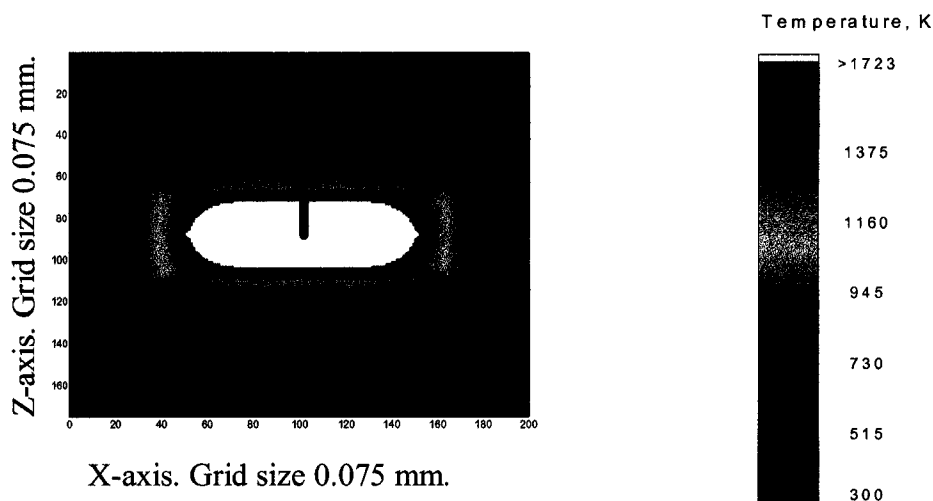


Figure1. Temperature distribution in the spot weld.

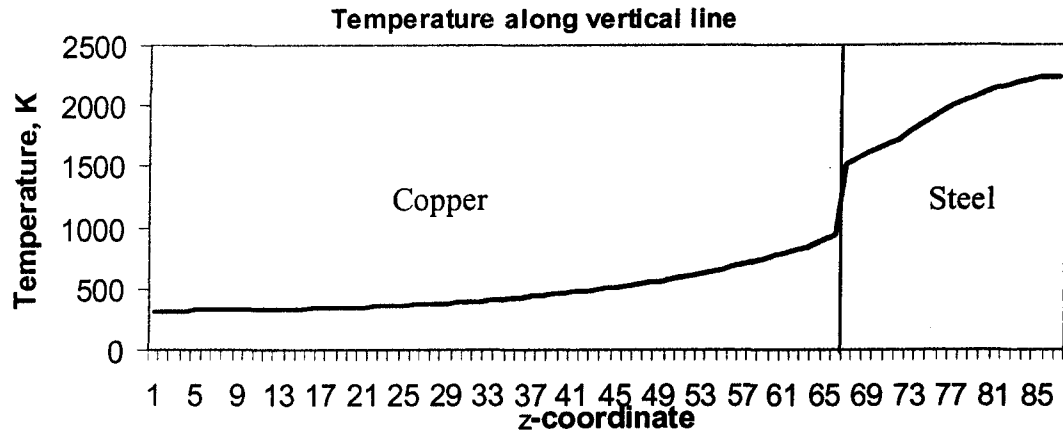


Figure 2. Temperature profile in the spot weld along the central axis.

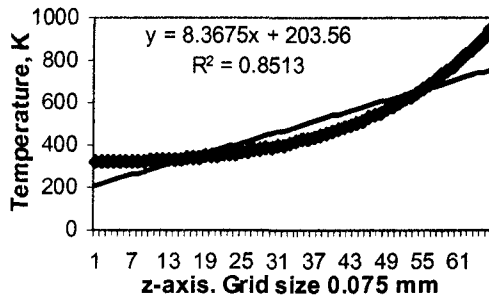


Figure 3. Piecewise approximation in the copper part.

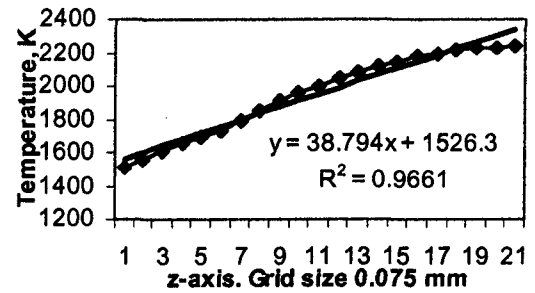


Figure 4. Piecewise approximation in the steel part.

2. Analytical Approach

In this part the wave propagation in linearly inhomogeneous media will be considered. That is, the combination of Lamé coefficients $\lambda + 2\mu$ will be described by function $f(z) = az$. The constant b was left aside to simplify the solution. One can consider wave propagation from right to left only from point L to point b/a . In this case

$$\frac{\partial}{\partial z} \left((\lambda + 2\mu) \frac{\partial u}{\partial z} \right) = \rho \frac{\partial^2 u}{\partial t^2} \quad \text{becomes} \quad \frac{\partial}{\partial z} \left((az) \frac{\partial u}{\partial z} \right) = \rho \frac{\partial^2 u}{\partial t^2} \quad (6)$$

and finally

$$z \frac{\partial^2 u}{\partial z^2} + \frac{\partial u}{\partial z} = \frac{\rho}{a} \frac{\partial^2 u}{\partial t^2} \quad (7)$$

This is the equation to describe the vibrations in one-dimensional linearly inhomogeneous media of length L . The real life analogies to be described by this equation could be the chain hanging from the hook; its strain is different at different heights because of mass of the chain; the air column. The first example deals with transverse oscillations while the second one with longitudinal. The boundary and initial conditions take the form

$$\frac{\partial u(0,t)}{\partial z} = 0 \text{ - free left end}$$

$$u(L,t) = A \sin(kt) \text{ - the right end is externally driven by oscillator.}$$

$$u(z,0) = 0, \quad \frac{\partial u(z,0)}{\partial t} = 0 \text{ - the system is initially in the rest.} \quad (8)$$

These boundary and initial conditions pretty much resemble the situation of our case when the acoustic wave comes from external source into initially non-vibrating media. The wave function describing the wave in such media comes from the solution of equation (7) imposed to the boundary conditions (8).

The first step to be taken to solve the problem is making the boundary conditions (BC) homogeneous. For this purpose the general solution u is represented in the form

$$u(z,t) = \varphi_1(z)f_1(t) + \varphi_2(z)f_2(t) + v(z,t) \quad (9)$$

$f_1(t)$ and $f_2(t)$ are the BC from (8) and φ_1, φ_2 have the form $az + b$.

Application of BC to equation (9) yields

$$u(z,t) = A \sin(kt) + v(z,t) \quad (10)$$

Equation (7) becomes more complicated but subject to the homogeneous BC:

$$zv_{zz} + v_z = \frac{\rho}{a} v_{tt} - \frac{\rho Ak^2}{a} \sin(kt) \quad (11)$$

$$v_z(0,t) = v(L,t) = 0, \quad v(z,0) = 0 \text{ and } v_t(z,0) = -Ak \quad (12)$$

The solution to the inhomogeneous equation (11) comes from the solution of respective homogeneous equation, subject to the same BC.

$$zv_{zz} + v_z = \frac{\rho}{a} v_{tt} \quad (13)$$

It can be shown that the infinite set of the solutions of equation (13) can be used to form orthonormal basis to expand equation (11).

Separation of variables of equation (13) gives

$$zZ''T + Z'T = \frac{\rho}{a} ZT'' \Rightarrow z\frac{Z''}{Z} + \frac{Z'}{Z} = \frac{\rho}{a} \frac{T''}{T} = -v^2 \quad (14)$$

$$\text{and finally } zf'' + f' + v^2 f = 0 \quad (15)$$

This equation is to provide the eigenfunctions needed to solve the original problem. It is reducible to Bessel's equation. One of the theorems of mathematical analysis states that the general solution of equation

$$x^p f''(x) + px^{p-1} f'(x) + (ax^q + bx^{p-2}) f(x) = 0 \quad (16)$$

has the form

$$f(x) = x^\alpha (c_1 J_\nu(\lambda x^\beta) + c_2 Y_\nu(\lambda x^\beta)) \quad (17)$$

$$\alpha = \frac{1-p}{2}, \quad \beta = \frac{q-p+2}{2}, \quad \lambda = \frac{2\sqrt{|a|}}{q-p+2}, \quad \nu = \frac{\sqrt{(1-p)^2 - 4b}}{q-p+2},$$

provided $\begin{matrix} (1-p)^2 - 4b \geq 0 \\ q-p+2 > 0 \end{matrix}$. J and Y are the Bessel functions of first and second kind.

For the given case $p=1$, $q=0$, $a=v^2$, $b=0$, and the general solution is

$$f(z) = c_1 J_0(2v\sqrt{z}) + c_2 Y_0(2v\sqrt{z}) \quad (18)$$

For the determination of the constants we examine the free (left) end. As the displacements are finite, the coefficient before the Y_0 function must be zero. It is physically reasonable because Bessel functions of the second kind go to infinity at zero.

At the right end $f(z)$ becomes zero

$$f(z) = c_1 J_0(2v\sqrt{z}) \Big|_{z=L} = c_1 J_0(2v\sqrt{L}) = 0, \quad (19)$$

$$2v\sqrt{z} = \lambda_k \Rightarrow v = \frac{\lambda_k}{2\sqrt{L}} \text{ at } z=L, \text{ where } \lambda_k \text{ are the roots of } J_0(\lambda) = 0.$$

Finally $f_k(z) = J_0\left(\lambda_k \sqrt{\frac{z}{L}}\right)$ represents the set of eigenfunctions with known

eigenvalues λ_k . This orthogonal set of eigenfunctions can be normalized using

$$\|f_k\|^2 = \int_0^L \left| J_0\left(\lambda_k \sqrt{\frac{z}{L}}\right) \right|^2 dz = L \cdot J_1(\lambda_k)^2 \quad (20)$$

to obtain the basis.

Any continuous function on $[0, L]$ can be expanded in this basis like

$$g(z) = \sum_1^{\infty} \frac{1}{L J_1(\lambda_k)} \left[\int_0^L g(z) J_0\left(\lambda_k \sqrt{\frac{z}{L}}\right) dz \right] J_0\left(\lambda_k \sqrt{\frac{z}{L}}\right).$$

Obtained expansion of homogeneous equation can be used to produce solutions of inhomogeneous equation $L(u) = F(z,t)$, namely equation (11)

$$zv_{zz} + v_z = \frac{\rho}{a} v_{tt} - \frac{\rho A k^2}{a} \sin(kt)$$

One needs to expand this equation in terms of obtained eigenfunctions to get rid of z variable and to solve it for time dependent component.

$$\int_0^L (zv_{zz} + v_z) J_0\left(\lambda_k \sqrt{\frac{z}{L}}\right) dz = \frac{\rho}{a} \int_0^L v_{tt} J_0\left(\lambda_k \sqrt{\frac{z}{L}}\right) dz - \frac{\rho A k^2}{a} \sin(kt) \int_0^L J_0\left(\lambda_k \sqrt{\frac{z}{L}}\right) dz$$

Using recurrence formulas one finally gets ordinary inhomogeneous equation

$$b_k''(t) + \frac{a\lambda^2}{4L\rho} b_k(t) = \frac{2Ak^2}{\lambda_k J_1(\lambda_k)} \sin(kt) \quad \text{or} \quad b_k''(t) + \alpha^2 b_k(t) = \beta \sin(kt) \quad (21)$$

$$\text{Here } b_k(t) = \int_0^L v(z, t) J_0 \left(\lambda_k \sqrt{\frac{z}{L}} \right) dz.$$

The general solution for this equation takes the form

$$b_k(t) = c_1 \cos(\alpha t) + c_2 \sin(\alpha t) + \frac{\beta \sin(kt)}{\alpha^2 - k^2} \quad (22)$$

Solution of (22) can be used to obtain series representation of $v(x, t)$:

$$v(z, t) = \sum_1^{\infty} b_k(t) f_k(z) = \sum_1^{\infty} b_k(t) J_0 \left(\lambda_k \sqrt{\frac{z}{L}} \right) \quad (23)$$

Application of initial condition to the (22) gives $c_1 = 0$ and $c_2 = \frac{-2Ak\alpha}{\lambda_k J_1(\lambda_k)(\alpha^2 - k^2)}$.

Thus the final form for $v(x, t)$ becomes

$$v(z, t) = \sum_1^{\infty} \left[c_2 \sin(\alpha t) + \frac{\beta \sin(kt)}{\alpha^2 - k^2} \right] J_0 \left(\lambda_k \sqrt{\frac{z}{L}} \right) \quad (24)$$

Recollecting the formula $u(z, t) = A \sin(kt) + v(z, t)$, the wave function for the vibrations in one-dimensional linearly inhomogeneous media, subject for given initial and boundary conditions takes the form

$$u(z, t) = A \sin(kt) + \sum_1^{\infty} \left[c_2 \sin(\alpha t) + \frac{\beta \sin(kt)}{\alpha^2 - k^2} \right] J_0 \left(\lambda_k \sqrt{\frac{z}{L}} \right) \quad (25)$$

In the following pictures the temperature decreases from left to right. Thus, density and acoustic velocity increases from left to right. Fig. 5 demonstrates wave propagation in linearly inhomogeneous media. Fig. 6 shows the pressure distribution of continuous wave in the same media having 3 times bigger size.

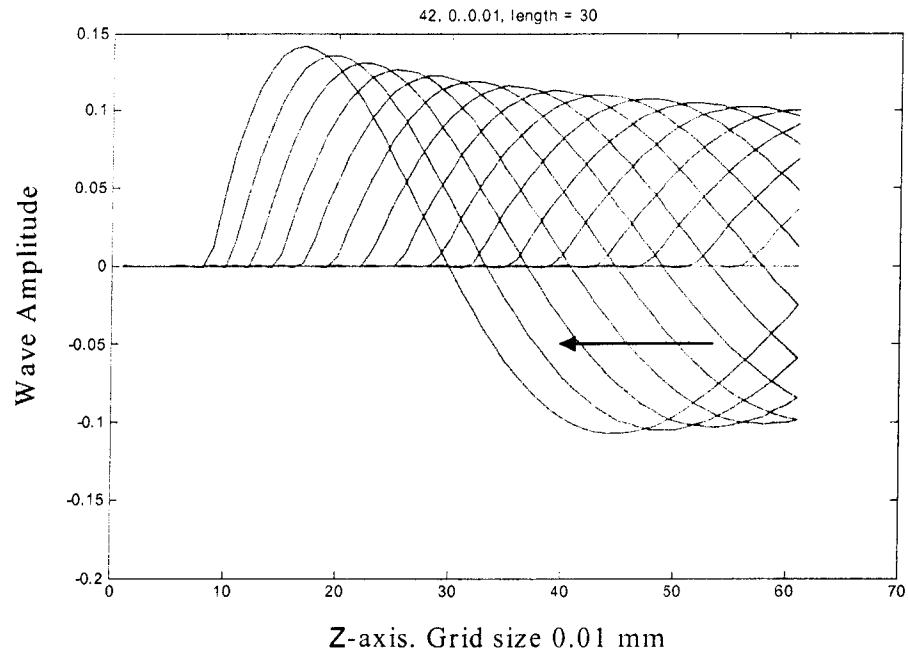


Figure 5. Wave propagating in the media with linear inhomogeneity. Wave propagates from right to left. The same time intervals between consecutive images of the wave provide different separation. The separation decreases as wave progresses to the left revealing the drop of propagation velocity.

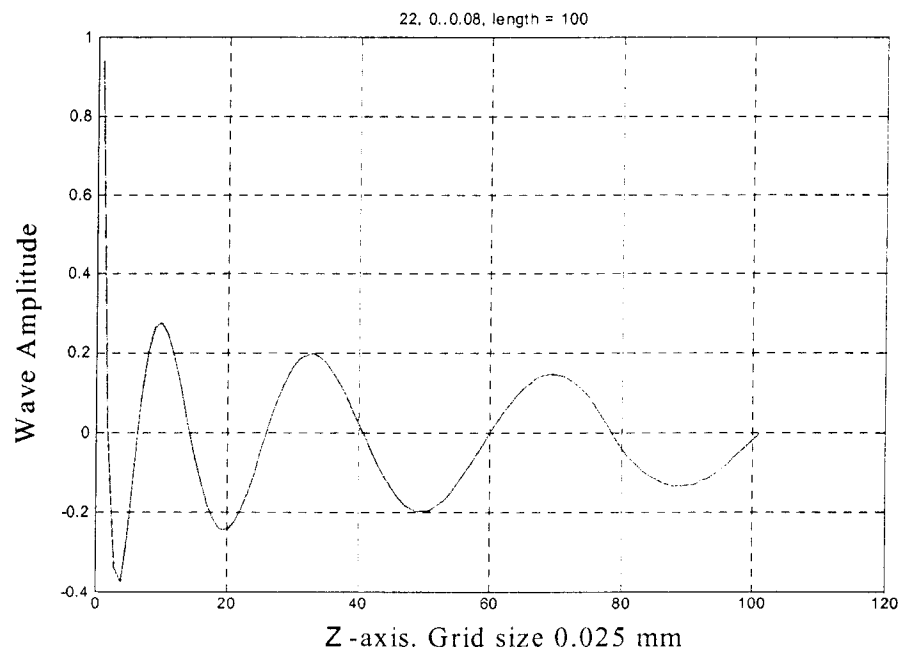


Figure 6. Wave propagating in the media with linear inhomogeneity. As the acoustical impedance decreases, the amplitude of displacement grows; as the velocity in the media decreases, the “wavelength”, or the distance between adjacent peaks, decreases.

3. Finite Difference Model

The advantage of numerical model is the fact that it enables to take into account much more features than the analytical approach does. It is relatively easy to deal with equations which have no analytical solution at all. The problem in study deals with discontinuous temperature, and thus material properties, fields. Analytical solutions can be often found only for some special cases with many simplifications. The more accurate solution should take into account nonlinear profile of velocities, density and thermal expansion of the material:

$$\frac{\partial f(x)}{\partial x} \frac{\partial u}{\partial x} + f(x) \frac{\partial^2 u}{\partial x^2} = \rho(x) \frac{\partial^2 u}{\partial t^2}. \quad (26)$$

In the following equations the notation for z-coordinate was substituted by x-coordinate.

The equation (26) describes the vibrations in the inhomogeneous media having arbitrary Lamé coefficients and density profiles. These profiles are formed by temperature profiles in the system during welding.

The finite difference formulation of this equation together with boundary conditions will enable to describe wave propagation in multilayered system consisting of inhomogeneous pieces.

The wave equation in one dimension will take the finite difference form

$$\frac{\partial^2 u}{\partial x^2} = \frac{1}{c^2} \frac{\partial^2 u}{\partial t^2} \quad \frac{u_{i-1}^n - 2u_i^n + u_{i+1}^n}{\Delta x^2} = \frac{1}{c^2} \frac{u_i^{n-1} - 2u_i^n + u_i^{n+1}}{\Delta t^2} \quad \begin{array}{l} n - \text{time} \\ i - \text{coordinate} \end{array}$$

Graphical representation of space-time in finite differences is shown in Fig. 7.

Given formulation enables to obtain the displacement at time step $(n+1)$ from time steps

$$(n) \text{ and } (n-1): u_i^{n+1} = ru_{i-1}^n + ru_{i+1}^n + 2(1-r)u_i^n - u_i^{n-1}, \quad r = \frac{c^2 \Delta t^2}{\Delta x^2}.$$

Unlike in thermal dynamics (parabolic equation), wave (hyperbolic) equation requires the knowledge of two previous time steps to calculate the next step. From equation (26) the same formulation for inhomogeneous media takes the form

$$u_i^{n+1} = ru_{i-1}^n \left(\frac{f_{i-1}^n - f_{i+1}^n}{4} + f_i^n \right) + ru_{i+1}^n \left(\frac{f_{i+1}^n - f_{i-1}^n}{4} - f_i^n \right) + 2(1-r)u_i^n - u_i^{n-1}, \quad r = \frac{\Delta t^2}{\rho_i^n \Delta x^2} \quad (27)$$

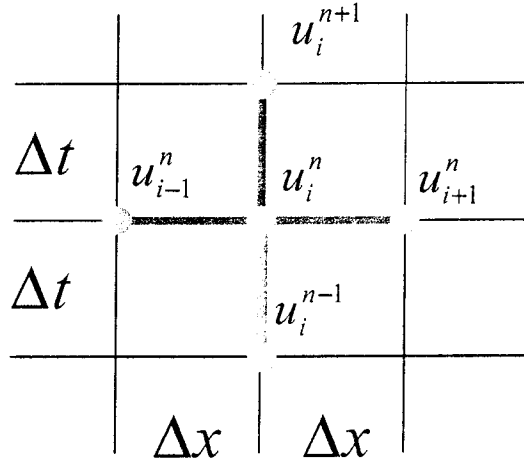


Figure 7. Discretization of space-time.

Treatment of interfaces is performed using boundary conditions

$$\begin{aligned} u_B^I &= u_B^{II}; \\ (\sigma_{ik} n_k)_B^I &= (\sigma_{ik} n_k)_B^{II}. \end{aligned} \quad (28)$$

In one dimension they become

$$\begin{aligned} u_1^B &= u_2^B; \\ (\lambda_1 + 2\mu_1) \frac{\partial u_1^B}{\partial x} &= (\lambda_2 + 2\mu_2) \frac{\partial u_2^B}{\partial x}. \end{aligned} \quad (29)$$

In order to fulfill requirements of boundary conditions it is necessary to introduce imaginary layers on the boundaries of numerical model. Fig. 8 shows introduction of the layers in the media having higher propagation velocity at the interface.

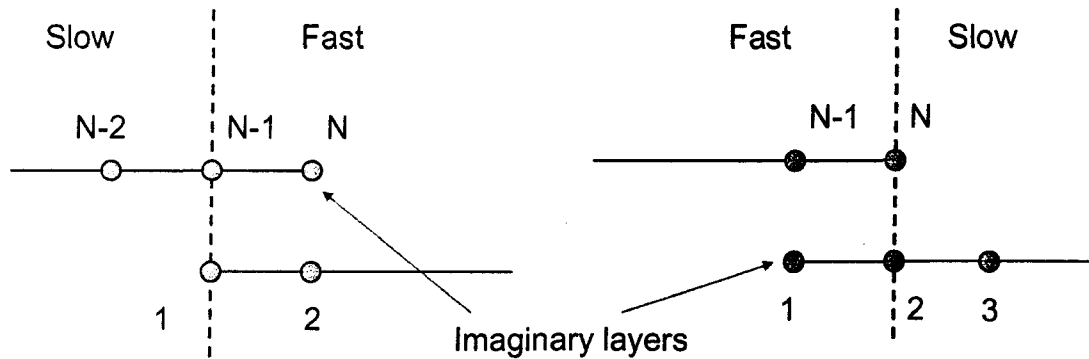


Figure 8. Introduction of imaginary layer in the faster media is needed to realize the boundary conditions in numerical model.

Waves propagating on a discrete grid become progressively dispersed with increasing travel time. This phenomenon is called grid dispersion. The dispersion increases in prominence as the grid interval becomes larger. Making the grid size close to the product $c\Delta t$ reduces the error (c is the sound velocity in given point of the media). If velocity changes, grid size can be adjusted in accordance with velocity at given point. The error accumulation due to too big grid size and normal wave are shown on Figs. 9 and 10. When the grid size is properly adjusted the error is almost invisible during time period used in the model, Figs. 11 and 12.

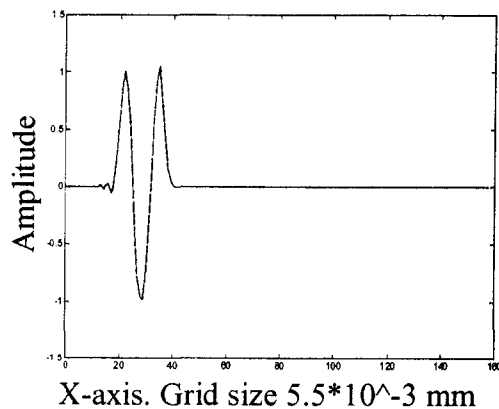


Figure 9. Wave with big grid size. In the beginning.

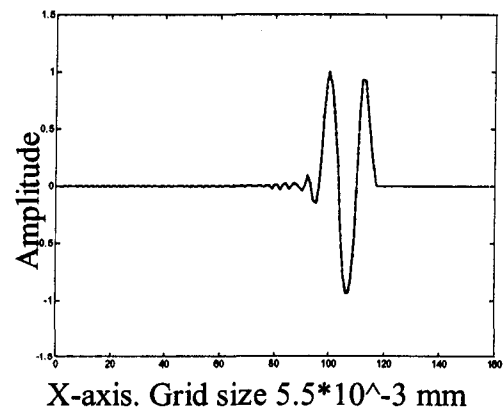


Figure 10. Wave 90 iterations later. The error accumulates as time progresses.

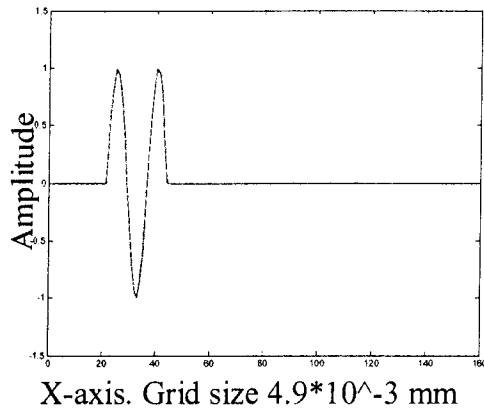


Figure 11. Wave in the media with correct grid size.

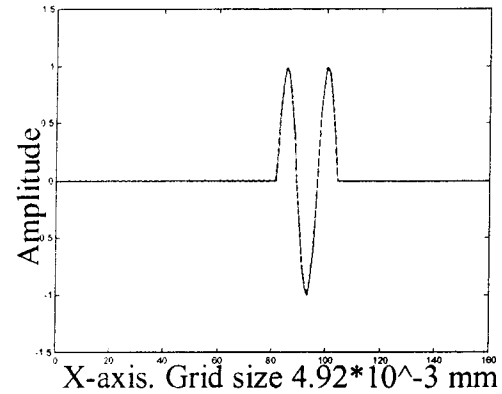


Figure 12. Wave 90 iterations later. Error is invisible (very small).

The temperature dependence of material properties such as velocity, density or thermal expansion coefficient can be taken from the tables. The thermal expansion at melting can be calculated from the density plot – if one knows solid and liquid state densities at the melting temperature. All plots for material temperature dependencies are given in Appendix A. For mild steel the change of linear dimensions at phase transition from solid to liquid is 1.535%.

Thus the signal travels through the multilayer system consisting of inhomogeneous parts. The temperature and material property profiles in these layers change with time (as welding goes on). Their rate of change is relatively small compared to the time of wave propagation. In other words it is possible to consider the temperature distribution as stationary during the period the wave passes through. During this time (about 5 microseconds) the real TOF increases approximately by 1.0000275, or by 0.00275 %. During 87 iterations (time of welding) the total error of TOF will constitute about 0.23 %. It is sufficient to consider the picture as quasi-stationary because these calculations are compared with the experimental results having possible error in the range of 2-4 % of the

total TOF. This error arises from the finite discretization of the oscilloscope. 66 MHz discretization rate provides possible TOF error about 7.5 ns. Total TOF parameter varies from 180 ns to 330 ns thus giving error in the range of 2-4 %. Thus 0.23 % error in the TOF calculation using stationary picture is small enough for the reflection of experiment reality. Figures 13, 14, 15 show temperature distributions in half of the setup at different welding time. For each temperature distribution there is corresponding velocity, density and thermal expansion coefficient distributions. Figs 16, 17, 18 represent velocity distributions as an example. The rightmost plots show molten region in steel part – discontinuity in temperature distribution (Fig 15.) and abrupt drop of the velocity (Fig. 18).

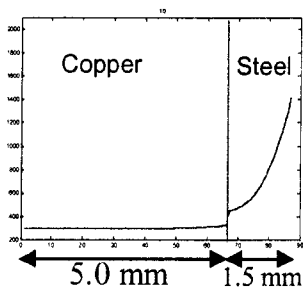


Figure 13. Temperature at first welding cycle.

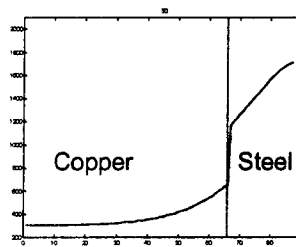


Figure 14. Temperature at cycle 6.

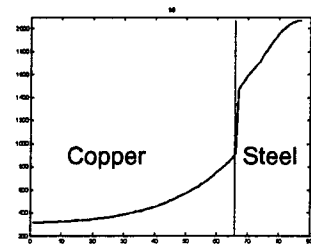


Figure 15. Temperature at the end of cycle 11.

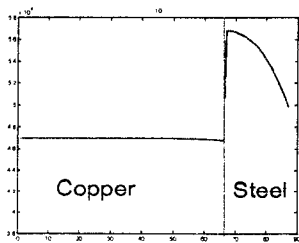


Figure 16. Velocity at first welding cycle.

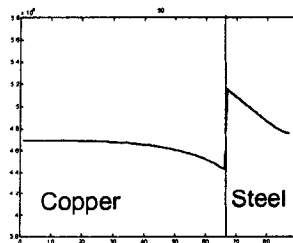


Figure 17. Velocity at cycle 6.

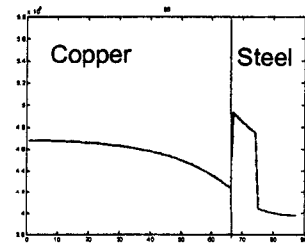


Figure 18. Velocity at the end of cycle 11.

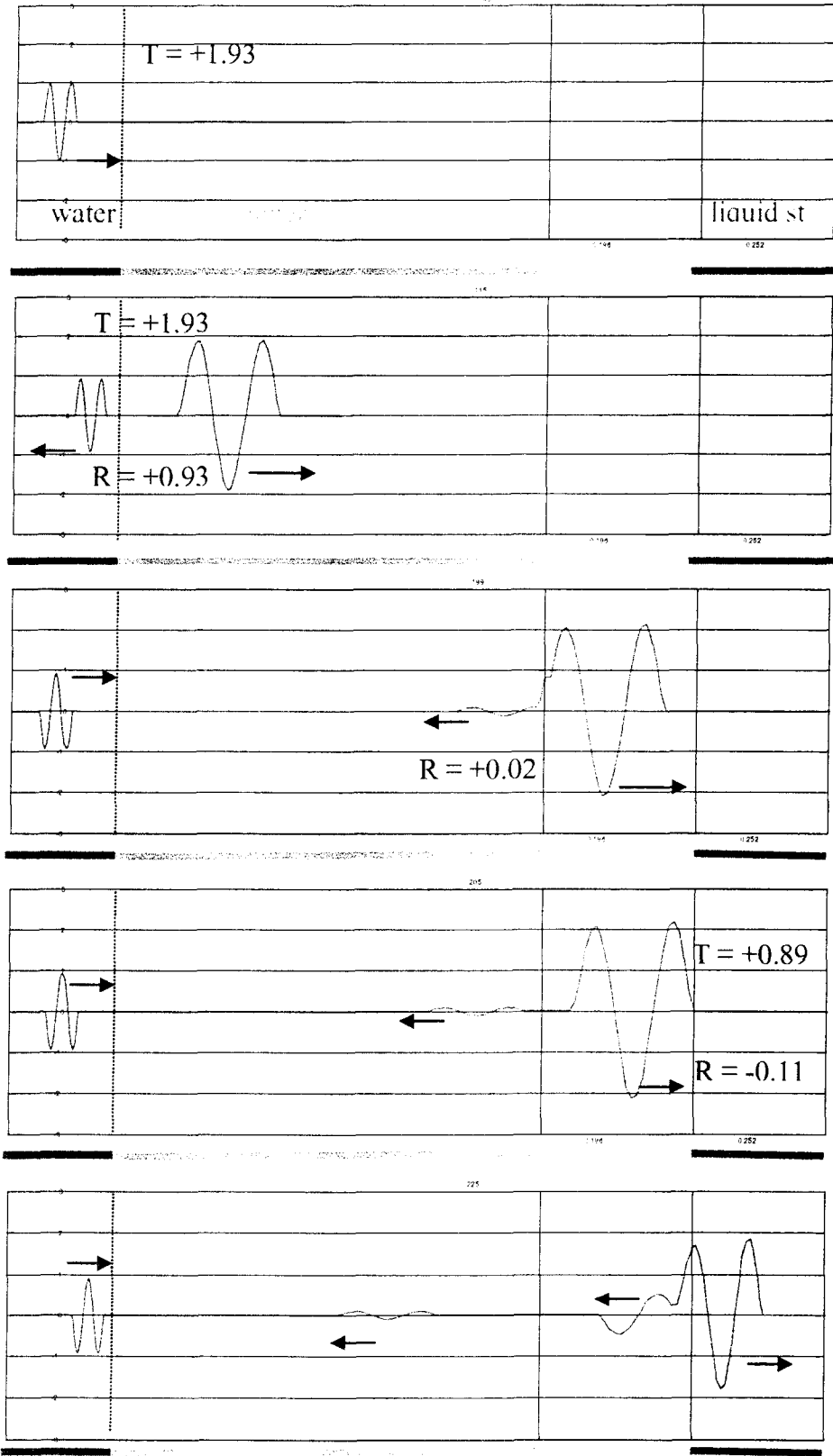


Figure 19. Pressure of the wave passing through different materials. Reflection and transmission coefficients for pressure at every interface are given as R and T respectively.

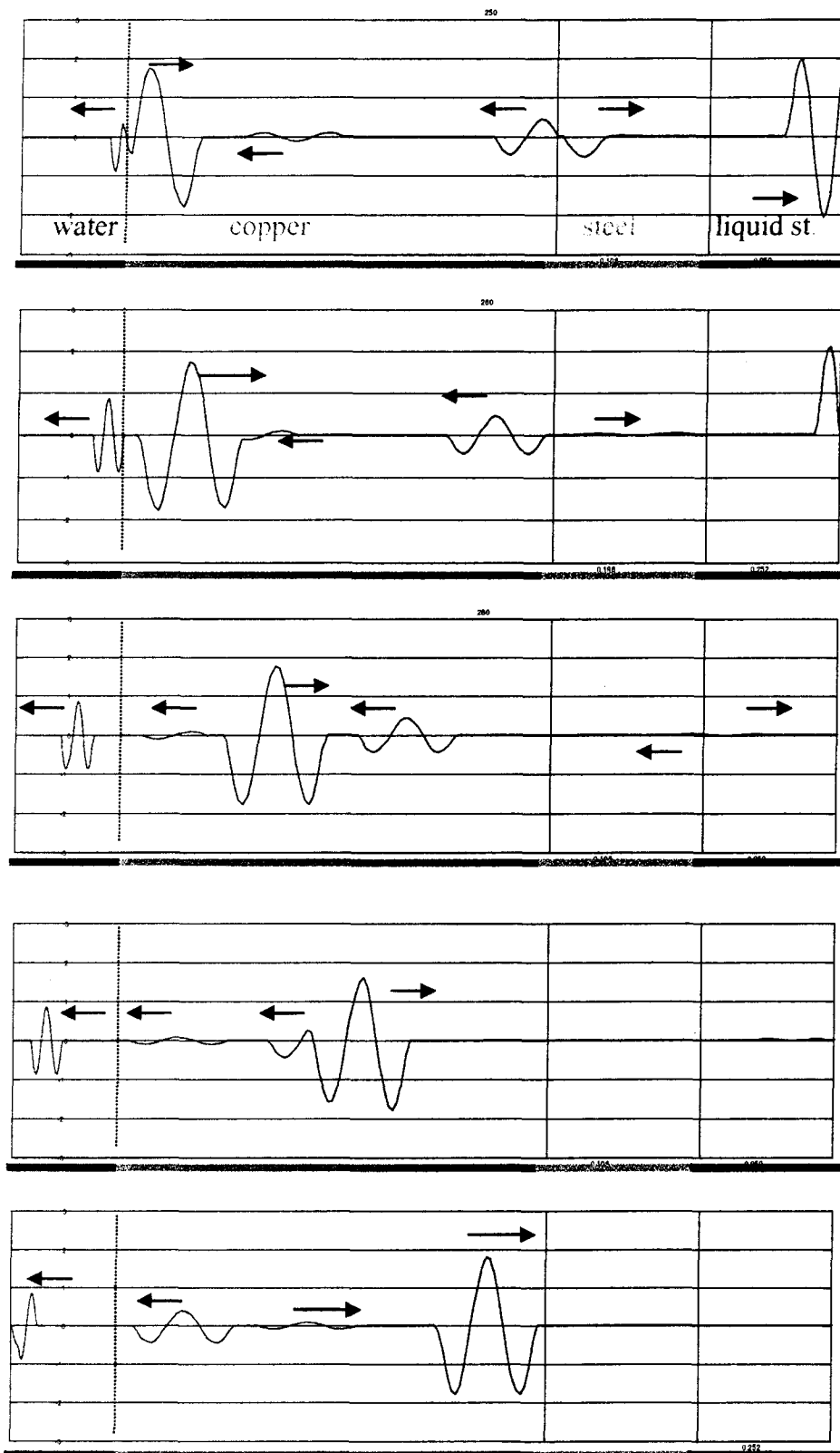


Figure 20. Pressure of the wave passing through different materials. Minus in reflection coefficient denotes phase inversion on reflection.

Figs. 19, 20 demonstrate dynamics of the wave pressure in different media. The wave starts to move from the left end (from water) and experiences multiple reflections on interfaces between different inhomogeneous parts of the setup. As the maximum (theoretical) transmission coefficient for the pressure is 2, there is no violation of energy conservation law. For example, transmission coefficient for pressure at water-copper interface when the wave travels from water into copper is 1.93.

$$T = \frac{2z_2}{z_1 + z_2} \quad z_1, z_2 \text{ are acoustic impedances of mediums.}$$

Calculation of TOF at every stage of welding generates the time-of-flight curve. The travel time of the wave could be calculated from the previously obtained velocity distribution along the wave path. As long as the space was discretized, the velocity was found in the corresponding nodes of the grid. The velocity was considered to be constant within the length of the grid near the given node. Thus the total propagation time can be calculated by summation of the travel times through every grid cell. Figs. 21, 22 represent the experimental TOF curves for stick weld and good weld. Theoretical calculation of TOF has been performed only for the time of welding. Cooling and solidification processes were not considered. The attention was concentrated at this region because it is the most stable region on experimental curve throughout the welding process. Before the current is on and after the current is off the TOF curve happens to be unstable and does not represent much interest.

The obtained TOF curves describe the delay of the through transmitted signal at different moments of welding. The value of TOF parameter in the beginning corresponds to the time of flight through the cold setup. At the very end (when current turns off) TOF parameter is the travel time through the hot setup with the liquid area inside. The

difference of these two marginal values characterizes the difference between the cold setup and setup at the final stage of heating. This difference, or the height of the peak on the TOF curve, is the integral degree of heating. From experiment this parameter has correlation with nugget size in the range of 90-95%. The series of welds made for the verification of thermal model (Chapter III) was also used for checking the wave propagation model. The time-of-flight was measured for every weld during its manufacturing.

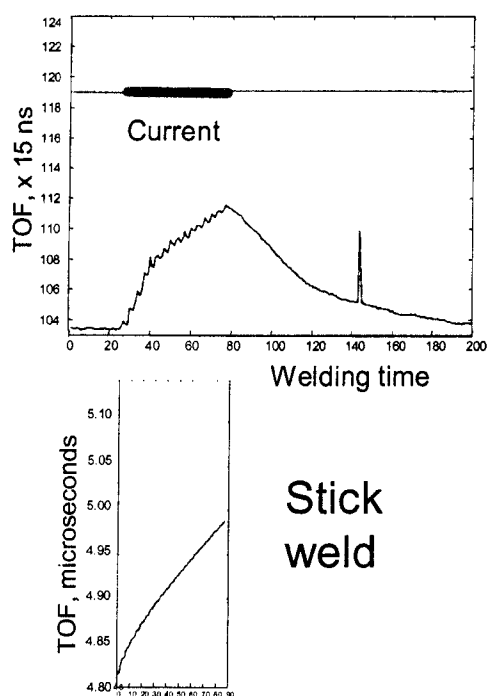


Figure 21. Stick weld. Experimental TOF curve (upper), theoretical (lower).

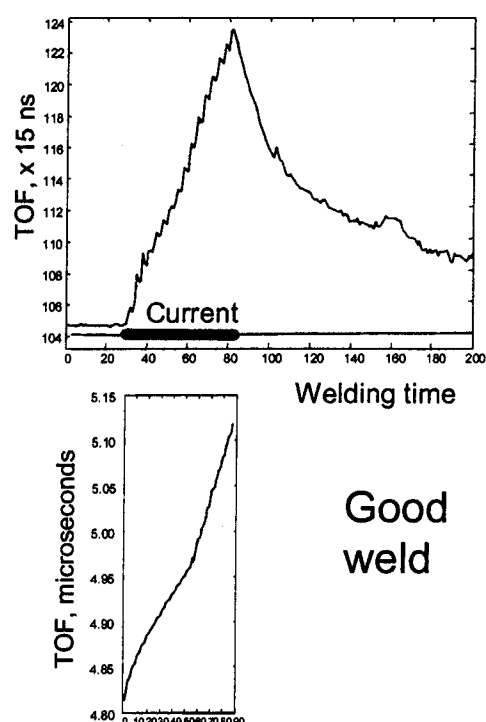


Figure 22. Good weld. Experimental TOF curve (upper), theoretical (lower).

The TOF values were in the range of 280-320 ns versus 303 ns for the calculated value. Thus the calculated TOF value lies within the experimentally obtained numbers.

The reason for such a big difference in experimental TOF is in instability of pressure inside the molten pool and unpredictable immersion of the tips into the molten area.

Another very important point at these plots is the point of discontinuity on TOF curve characterizing good weld. The nature of this distinct change of slope (change of heating rate) is the phase transformation. At the melting moment the electrical resistivity of steel jumps abruptly by more than 30 % (Fig 23). It causes sudden increase of the resistance of molten area and thus the increase of generated heat per unit time.

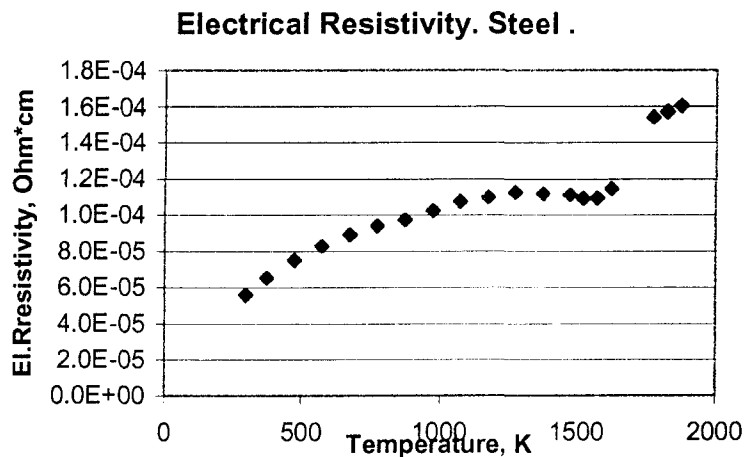


Figure 23. Electrical resistivity of steel as function of temperature.

This phenomenon enables us to identify the moment of melting which is very important in spot weld quality assurance. In the stick weld this moment is not seen on the experimental curve.

The reasonable question may arise if one compares the theoretical and experimental curves for the stick weld. What causes the change of the slope to the smaller values in this case? The possible reason which had not been considered in full in the thermal model is as follows. The contact resistance between steel plates is not constant. It plays considerable role in heat generation at the beginning of welding. When the contact surfaces become hot their roughness decreases thus decreasing the contact resistance. If

the current flowing through the setup is not strong enough it will not be able to continue generation of considerable amount of heat only due to volume (material) resistance of steel plates. In this case the amount of heat generated per unit time will decrease thus decreasing the slope of TOF curve. At higher values of current (good weld) the contact heat generation enables to melt surrounding areas of steel before it vanishes. The current flowing through the molten area begins to generate more heat even in the absence of contact resistance. Thus the process continues to be self-sustaining and generates heat at even higher rates causing change of the slope of TOF curve to the bigger value.

References

1. Gerald B. Folland. *Fourier Analysis and Its Applications*. Brooks/Cole Publishing Company, 1992.
2. Acoustic Fields and Waves in Solids, B.A. Auld
3. Weng Cho Chew. *Waves and Fields in Inhomogeneous Media*. Wiley-IEEE Press; Reprint edition (December 1995).
4. N.W. McLachlan. *Bessel Functions for Engineers*. Oxford: Clarendon Press, 1961.
5. P. DuChateau, D. Zachmann. *Applied Partial Differential Equations*. New York: Harper & Row, 1989.
6. F.E. Relton. *Applied Bessel Functions*. London: Blackie, 1946.

CHAPTER V

Discussions, Conclusions and Future Work

In this work several models describing the process of spot welding and the process of wave propagation through the joint during its manufacturing were developed.

The first part dealt with the problem of temperature distributions in spot weld at different times of welding. The transient heat conduction equation has been used to describe the spot weld formation. The analytical approach considered one-dimensional picture with all material properties having constant values (average within the temperature range). Only the most critical parameter – the heat generation – was considered as a function of temperature and time. This dependency is the most important in the model as it reflects the main idea of the heat generation in spot welding. The solution was presented piecewise: one part described temperature distribution in steel another one in copper. The functions were expanded in infinite series of corresponding eigenvalues. The model calculated just one half of the setup as it is symmetrical with respect to the steel-steel interface. The model uses several assumptions and simplifications but in spite of this it reflects the general pattern of temperature distribution in the system.

Numerical model considered three-dimensional case. Introduction of cylindrical coordinate system and use of the azimuthal angle symmetry made possible to represent 3D picture with only two coordinates without loss of generality. Due to symmetry with respect to central (z) axis and with respect to the steel-steel interface plane (x-axis) (see

figure 5, Chapter III) the calculations have been performed only for the quarter of the setup. Given numerical model provided more realistic picture compared to analytical one as it described three-dimensional system with temperature dependent material properties.

The model of heat generation has shown good correlation of predicted weld geometry with the real welds. Metallographic weld cuts revealed similar weld shape. The peel test of the welds obtained at the same welding schedule as that in the model has shown nugget diameters close to the calculated values. The difference could arise from the fact that in the model we neglected heating of cooling water, steel-copper interface heat generation and from uncertainty of the peel test measurements having possible error of 10-20%. In general, comparison of simulation with experiment has verified that the model satisfactorily reflects the features needed in subsequent wave propagation simulation.

The second part used the results of thermal model to describe wave propagation in inhomogeneous multilayered system. As the signal is sent through the setup at every stage of welding, the obtained temperature distributions were used to calculate material property distributions. The last define the acoustical properties at every point to simulate wave behavior in the setup. Thus the 1D wave propagation model enables to visualize the process, to calculate time of flight at every moment and to estimate the opportunity to use the reflected signal to identify melting moment. Both analytical and numerical models used translational equation of motion to describe wave propagation in inhomogeneous media. In analytical approach there was derived the wave function for wave propagation in linearly inhomogeneous media. The wave function was expanded into infinite series made of orthogonal set of Bessel functions. The numerical simulation enabled to solve

the problem with arbitrary (nonlinear) distribution of material properties. The TOF parameter lied within the experimentally obtained range of values. This was the main criteria used to verify correctness of the wave model. It has also implicitly confirmed correctness of the thermal simulation, as these calculations were based on the results of the thermal model.

The wave propagation simulation has shown the possibility to identify melting moment using through transmission signal. This is very important feature in welding technology. The ability to distinguish good weld from bad one during welding could provide reliable instrument to correct welding process in on-line mode. It was theoretically shown that the discontinuity of TOF curve in the middle of welding process corresponds to the beginning of melting.

Thus the signal time of flight becomes the implicit measure of the degree of heating of the setup. It provides the integral value of the delay, and thus the integral value of heating. The obtained thermal model can be used to separate the effects of velocity drop and thermal expansion. Having the general patterns of temperature distributions in spot weld and the experimentally measured TOF it is possible to define the picture of temperature distributions in the setup. In other words one can solve the inverse problem of finding the nugget size (and total temperature distribution) using just one experimentally obtained set of parameters – time-of-flight curve. The discontinuity on TOF curve could be used as a reference point to locate the moment of melting. From the set of previously calculated temperature distributions the software could select the one which corresponds to the given melting moment position and final TOF value.

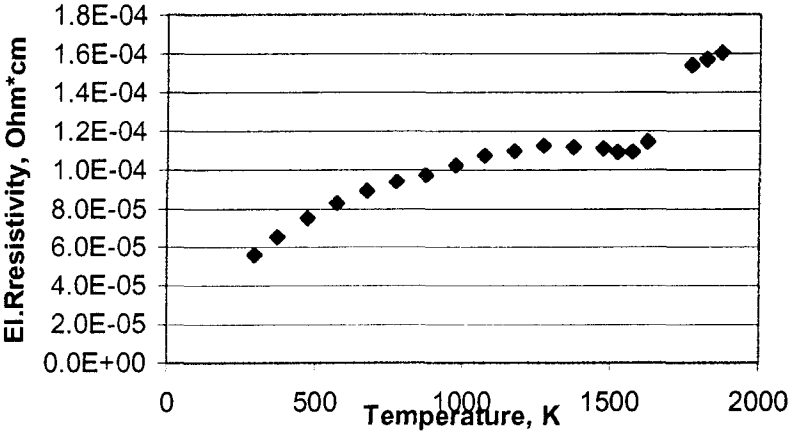
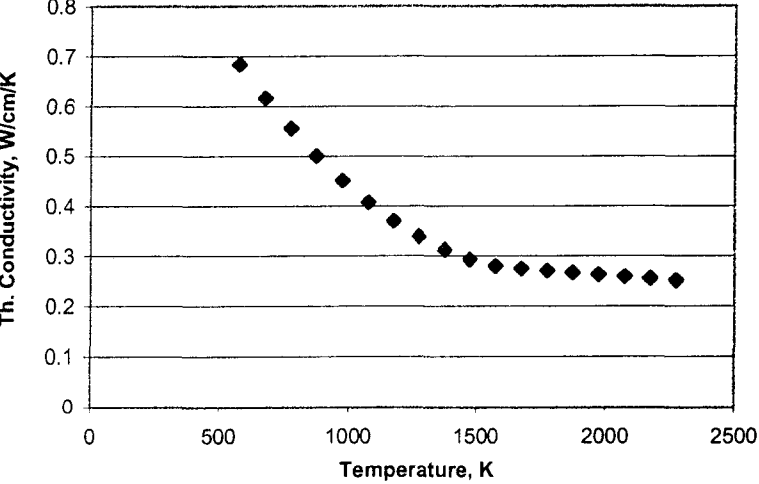
Temperature distribution tells the actual size of the molten area. The last defines geometry of the future nugget size after solidification.

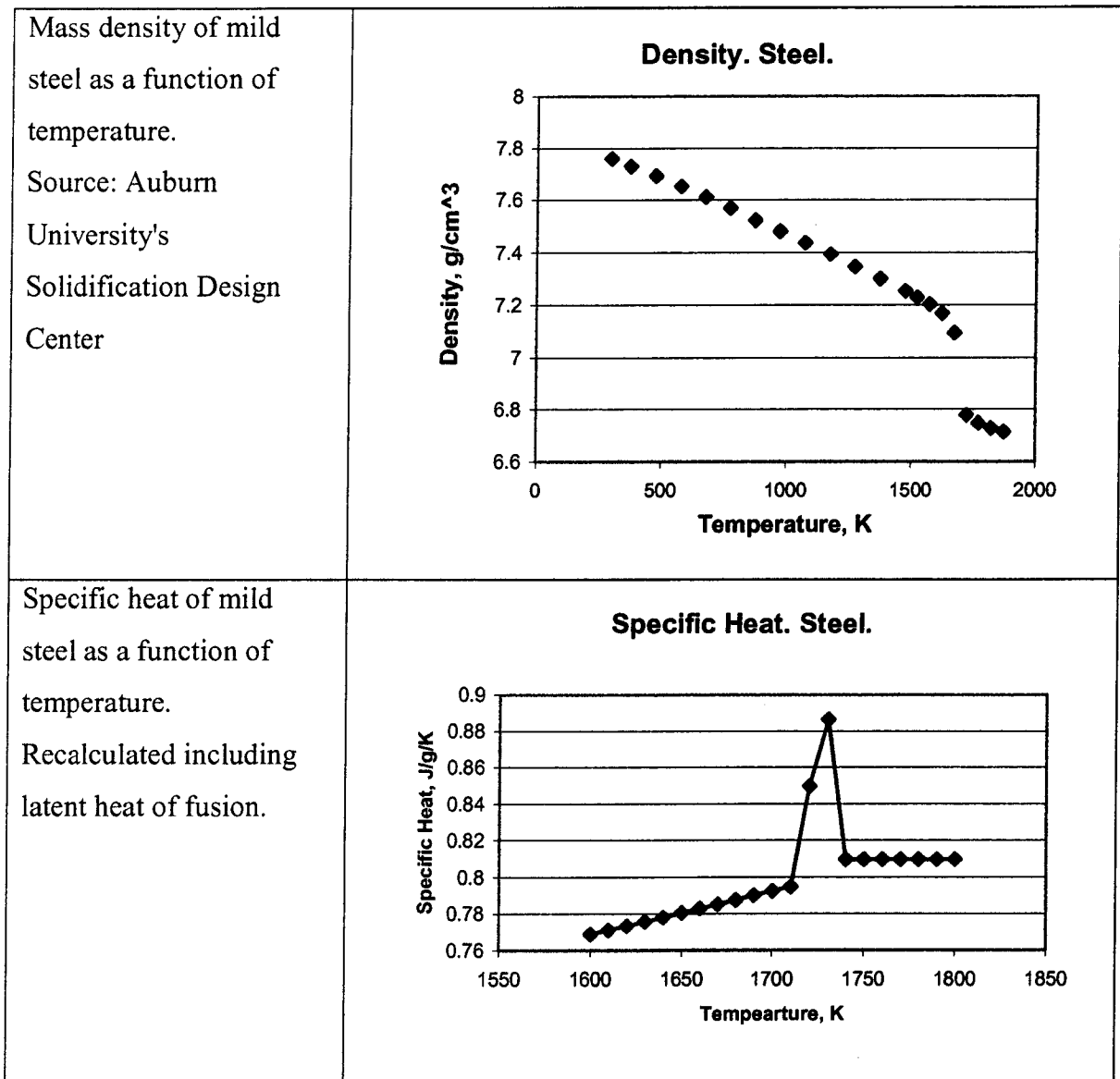
In general the model has shown good correlation of calculated values with experimental results for both thermal processes and wave propagation. Of course the method is still to be improved in order to consider common side effects affecting the welding. The above calculations have been performed for ideal welding conditions with no misalignments, impurities in electrode tips or pressure fluctuations during welding. These are all common side effects which introduce some uncertainties to the real process. In fact, this is more technical problems than physical. But developing the mathematical algorithms capable to describe aging of electrodes could be very challenging and important problem. It could consider diffusion of impurities (zinc, iron) into the body of copper electrodes at elevated temperatures and their effect on thermal conductivity and resistivity of the near-surface electrode layer. Another interesting problem to be solved as logical continuation of the research is developing the model of 3D acoustic beam behavior in the complex geometry of spot-weld system. Both through transmission and reflection modes can be considered, as both of these configurations are within the scope of interests of this research.

Appendix A

Material Properties

Steel

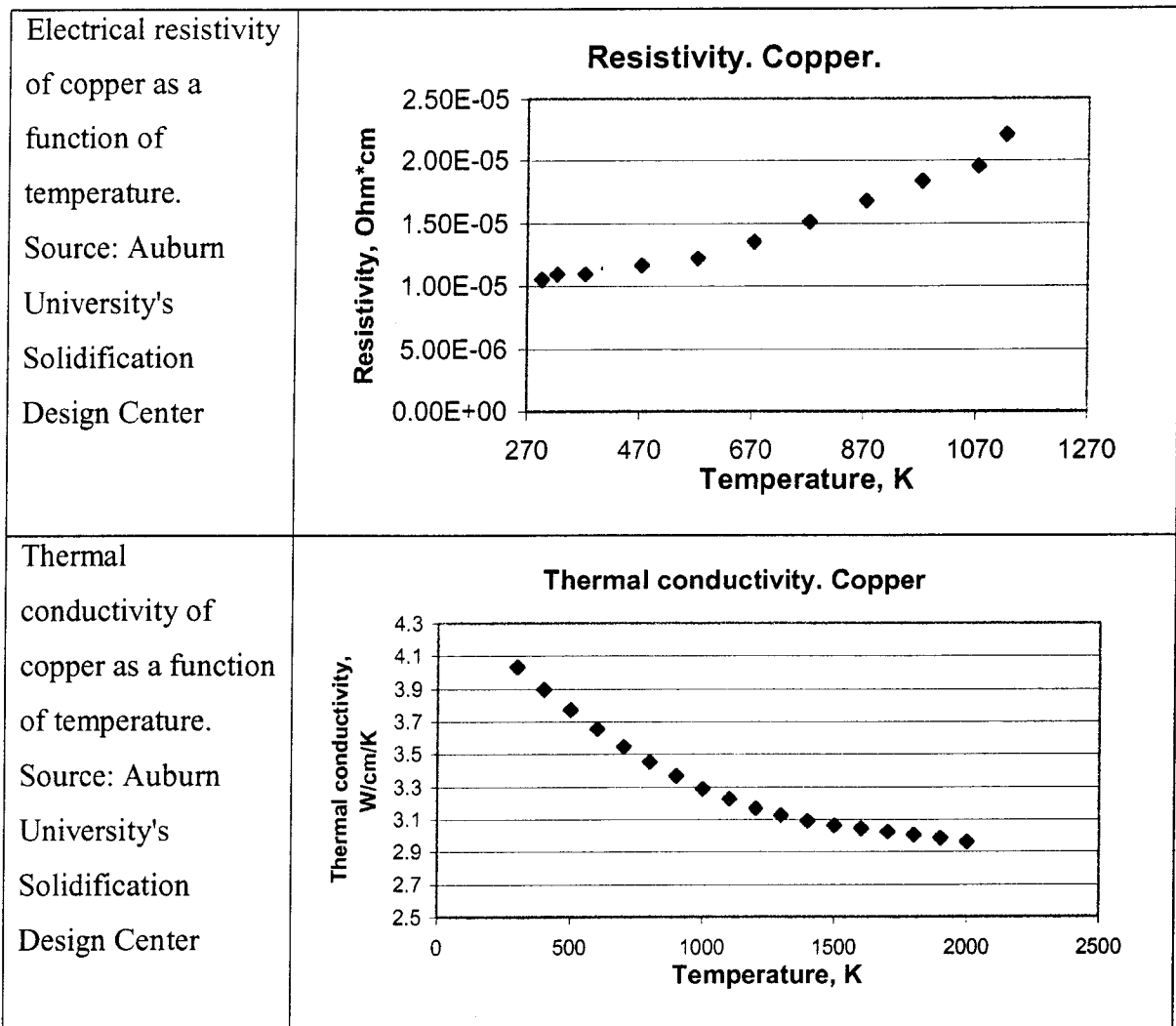
<p>Electrical resistivity of mild steel as a function of temperature.</p> <p>Source: Auburn University's Solidification Design Center</p>	<p>Electrical Resistivity. Steel .</p>  <table border="1"><thead><tr><th>Temperature, K</th><th>El. Resistivity, Ohm*cm</th></tr></thead><tbody><tr><td>300</td><td>5.5E-05</td></tr><tr><td>400</td><td>6.5E-05</td></tr><tr><td>500</td><td>7.5E-05</td></tr><tr><td>600</td><td>8.5E-05</td></tr><tr><td>700</td><td>9.5E-05</td></tr><tr><td>800</td><td>1.0E-04</td></tr><tr><td>900</td><td>1.05E-04</td></tr><tr><td>1000</td><td>1.1E-04</td></tr><tr><td>1100</td><td>1.15E-04</td></tr><tr><td>1200</td><td>1.15E-04</td></tr><tr><td>1300</td><td>1.15E-04</td></tr><tr><td>1400</td><td>1.15E-04</td></tr><tr><td>1500</td><td>1.1E-04</td></tr><tr><td>1600</td><td>1.1E-04</td></tr><tr><td>1700</td><td>1.15E-04</td></tr><tr><td>1800</td><td>1.55E-04</td></tr><tr><td>1900</td><td>1.6E-04</td></tr></tbody></table>	Temperature, K	El. Resistivity, Ohm*cm	300	5.5E-05	400	6.5E-05	500	7.5E-05	600	8.5E-05	700	9.5E-05	800	1.0E-04	900	1.05E-04	1000	1.1E-04	1100	1.15E-04	1200	1.15E-04	1300	1.15E-04	1400	1.15E-04	1500	1.1E-04	1600	1.1E-04	1700	1.15E-04	1800	1.55E-04	1900	1.6E-04		
Temperature, K	El. Resistivity, Ohm*cm																																						
300	5.5E-05																																						
400	6.5E-05																																						
500	7.5E-05																																						
600	8.5E-05																																						
700	9.5E-05																																						
800	1.0E-04																																						
900	1.05E-04																																						
1000	1.1E-04																																						
1100	1.15E-04																																						
1200	1.15E-04																																						
1300	1.15E-04																																						
1400	1.15E-04																																						
1500	1.1E-04																																						
1600	1.1E-04																																						
1700	1.15E-04																																						
1800	1.55E-04																																						
1900	1.6E-04																																						
<p>Thermal conductivity of mild steel as a function of temperature.</p> <p>Source: Auburn University's Solidification Design Center</p>	<p>Thermal Conductivity. Steel.</p>  <table border="1"><thead><tr><th>Temperature, K</th><th>Th. Conductivity, W/cm/K</th></tr></thead><tbody><tr><td>600</td><td>0.68</td></tr><tr><td>700</td><td>0.62</td></tr><tr><td>800</td><td>0.55</td></tr><tr><td>900</td><td>0.50</td></tr><tr><td>1000</td><td>0.45</td></tr><tr><td>1100</td><td>0.40</td></tr><tr><td>1200</td><td>0.37</td></tr><tr><td>1300</td><td>0.34</td></tr><tr><td>1400</td><td>0.31</td></tr><tr><td>1500</td><td>0.29</td></tr><tr><td>1600</td><td>0.28</td></tr><tr><td>1700</td><td>0.27</td></tr><tr><td>1800</td><td>0.27</td></tr><tr><td>1900</td><td>0.27</td></tr><tr><td>2000</td><td>0.26</td></tr><tr><td>2100</td><td>0.26</td></tr><tr><td>2200</td><td>0.26</td></tr><tr><td>2300</td><td>0.25</td></tr></tbody></table>	Temperature, K	Th. Conductivity, W/cm/K	600	0.68	700	0.62	800	0.55	900	0.50	1000	0.45	1100	0.40	1200	0.37	1300	0.34	1400	0.31	1500	0.29	1600	0.28	1700	0.27	1800	0.27	1900	0.27	2000	0.26	2100	0.26	2200	0.26	2300	0.25
Temperature, K	Th. Conductivity, W/cm/K																																						
600	0.68																																						
700	0.62																																						
800	0.55																																						
900	0.50																																						
1000	0.45																																						
1100	0.40																																						
1200	0.37																																						
1300	0.34																																						
1400	0.31																																						
1500	0.29																																						
1600	0.28																																						
1700	0.27																																						
1800	0.27																																						
1900	0.27																																						
2000	0.26																																						
2100	0.26																																						
2200	0.26																																						
2300	0.25																																						

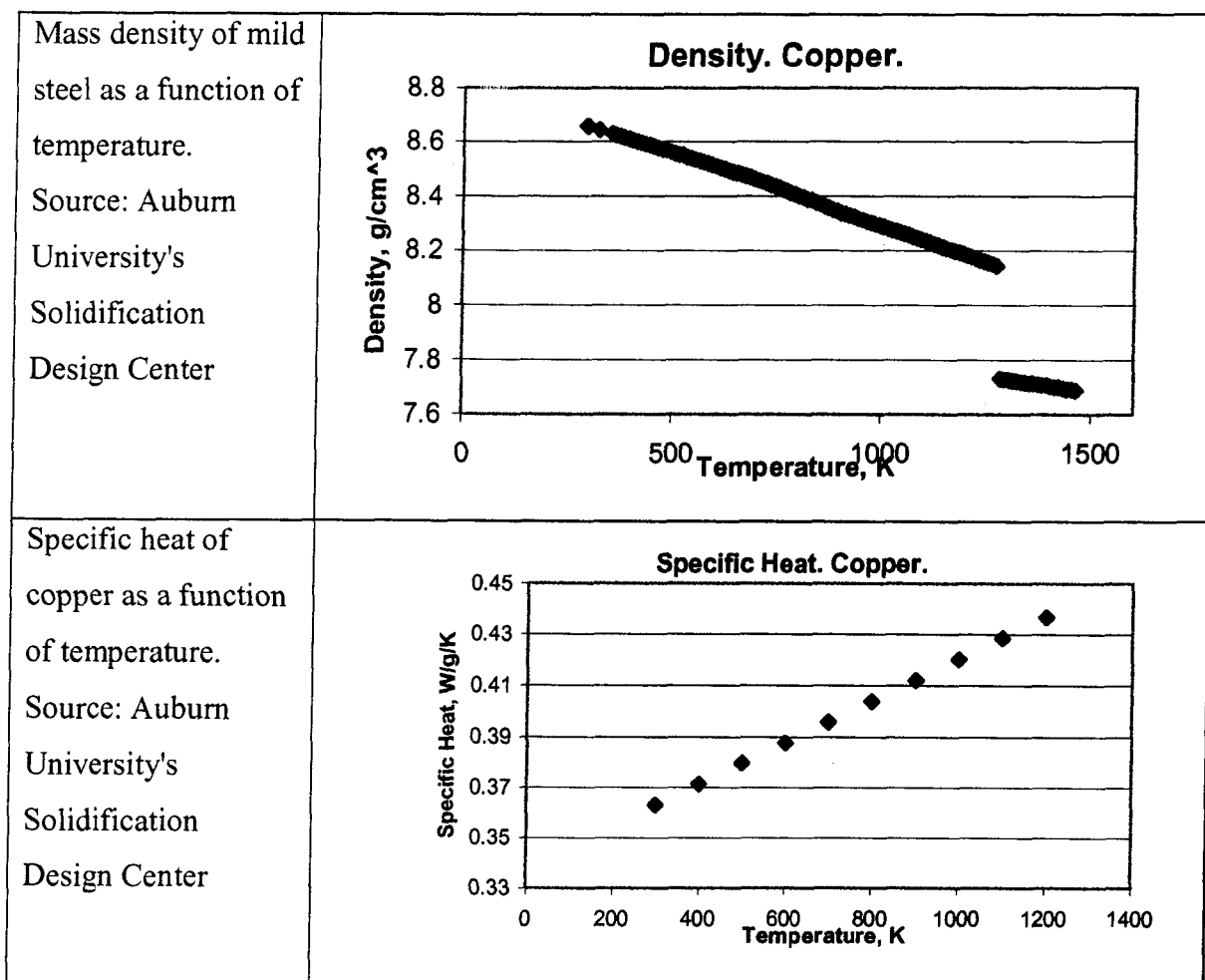


Chemical composition of mild steel in use.

Classification	Chemical Composition %							
	C	Mn	Si	Ti	Zr	Al	P	S
Mild Steel	0.07	0.90-1.40	0.40-0.70	0.05-0.15	0.02-0.12	0.05-0.15	0.025	0.035

Copper





Appendix B

Abbreviations used for analytical solution in Chapter III

$$\psi_1 = \frac{A}{\tau} \left[\frac{d_1 z_0 \sqrt{\alpha_1}}{\beta} \sin\left(\frac{\beta z_0}{\sqrt{\alpha_1}}\right) + \frac{d_1 \alpha_1}{\beta^2} \cos\left(\frac{\beta z_0}{\sqrt{\alpha_1}}\right) - \frac{d_1 \alpha_1}{\beta^2} + \frac{d_2 z_0 \sqrt{\alpha_1}}{\beta} \sin\left(\frac{\beta z_0}{\sqrt{\alpha_1}}\right) \right]$$

$$\psi_2 = \frac{A}{\tau} (d_3 rsnx + d_4 rsnc)$$

$$\psi_3 = \frac{A}{\tau} (d_3 rcscx + d_4 r csc)$$

$$rcscx = \frac{\sqrt{\alpha_2}}{\beta} \left[L \sin\left(\frac{\beta L}{\sqrt{\alpha_2}}\right) - z_0 \sin\left(\frac{\beta z_0}{\sqrt{\alpha_2}}\right) \right] + \frac{\alpha_2}{\beta^2} \left[\cos\left(\frac{\beta L}{\sqrt{\alpha_2}}\right) - \cos\left(\frac{\beta z_0}{\sqrt{\alpha_2}}\right) \right]$$

$$r csc = \frac{\sqrt{\alpha_2}}{\beta} \left[\sin\left(\frac{\beta L}{\sqrt{\alpha_2}}\right) - \sin\left(\frac{\beta z_0}{\sqrt{\alpha_2}}\right) \right]$$

$$rsnx = \frac{\sqrt{\alpha_2}}{\beta} \left[z_0 \cos\left(\frac{\beta z_0}{\sqrt{\alpha_2}}\right) - L \cos\left(\frac{\beta L}{\sqrt{\alpha_2}}\right) \right] + \frac{\alpha_2}{\beta^2} \left[\sin\left(\frac{\beta L}{\sqrt{\alpha_2}}\right) - \sin\left(\frac{\beta z_0}{\sqrt{\alpha_2}}\right) \right]$$

$$rsnc = \frac{\sqrt{\alpha_2}}{\beta} \left[\cos\left(\frac{\beta z_0}{\sqrt{\alpha_2}}\right) - \cos\left(\frac{\beta L}{\sqrt{\alpha_2}}\right) \right]$$

$$d_1 = 1, \quad d_2 = \frac{-k_1}{h} + \frac{k_1}{k_2} z_0 - \frac{k_1}{h_3} - \frac{k_1}{k_2} L - z_0, \quad d_3 = \frac{k_1}{k_2}, \quad d_4 = -\frac{k_1}{h_3} - \frac{k_1}{k_2} L$$

$$c_n^1 = \frac{k_1 c_2 T_1}{\beta \sqrt{\alpha_1}} \sin\left(\frac{\beta z_0}{\sqrt{\alpha_1}}\right)$$

$$c_n^{2\sin} = -\frac{k_2 c_4 T_2 \sigma}{\beta \sqrt{\alpha_2}} \left[\cos\left(\frac{\beta L}{\sqrt{\alpha_2}}\right) - \cos\left(\frac{\beta z_0}{\sqrt{\alpha_2}}\right) \right]$$

$$c_n^{2\cos} = \frac{k_2 c_4 T_2}{\beta \sqrt{\alpha_2}} \left[\sin\left(\frac{\beta L}{\sqrt{\alpha_2}}\right) - \sin\left(\frac{\beta z_0}{\sqrt{\alpha_2}}\right) \right]$$

Appendix C

The Acoustic Field of Circular Transducer

The Rayleigh-Sommerfeld integral

$$p(x, \omega) = \frac{-i\omega\rho v}{2\pi} \int_S \frac{\exp(ikr)}{r} dS$$

enables to calculate the pressure field at every point of space. The oscillator is mounted in an extended absolutely rigid wall and radiates into a liquid. Every point of emitting surface S (figure) is represented as the point source of spherical wave. The Sommerfeld radiation condition states that

$$R \left(\frac{\partial p}{\partial R} - ikp \right) \rightarrow 0 \text{ as } R \rightarrow \infty$$

$$p \rightarrow 0 \text{ as } R \rightarrow \infty$$

These condition guarantees that waves at infinity are outgoing waves and decay sufficiently fast so that there no sources at infinity. Contribution of the surface at infinity is zero.

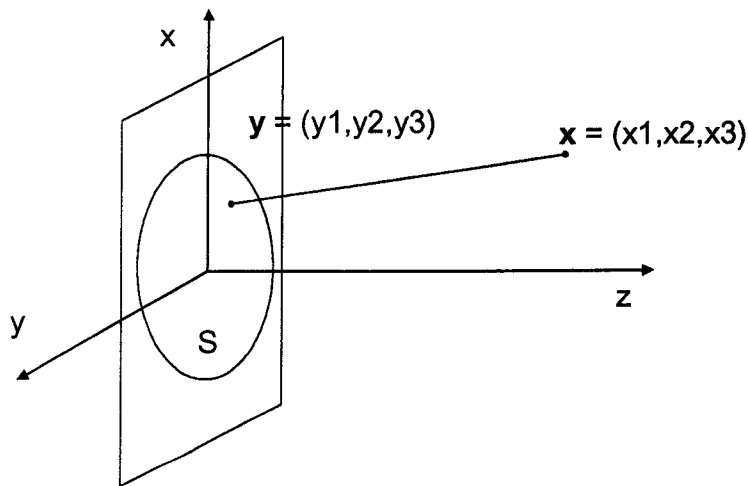


Figure 1

The direct numerical integration of given integral enables to get pressure distribution in water with circular transducer of 7 mm diameter. See figure.

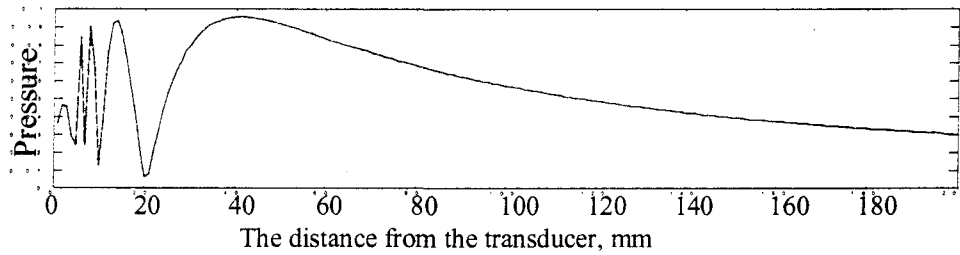


Figure 2. On-axis pressure in the water. Continuous excitation.

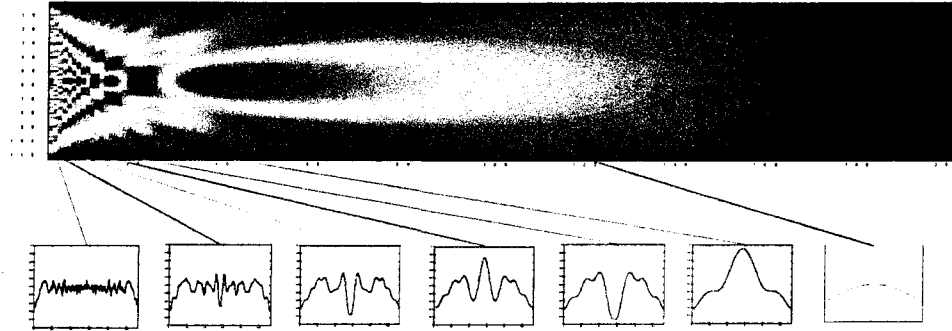


Figure 3. The field of 7 mm piston in the water. 5 MHz.

The near (interference) field is 40 mm. It could be inferred from both the figures 2, 3 and from the estimation formula

$$N = \frac{D^2 - \lambda^2}{4\lambda} \quad D - \text{transducer diameter}, \quad \lambda - \text{wavelength}$$

5 MHz wave in water has the wavelength of 0.3 mm. $D = 7.0$ mm.

In given setup the area of interest is located in the transducer's far field. It guarantees that there will be no sudden changes of signal amplitude when the geometry of liquid area will begin to change. The divergence angle of the far field is about 3 degrees. It can be calculated from the formula

$$\gamma = 1.2 \frac{\lambda}{D} \frac{180}{\pi} \text{ degrees.}$$

It can also be seen from the figure 3 – most of the field is concentrated within transducer diameter. In the case of pulsed radiation (the real case) the picture is not as clear as in continuous excitation. The shorter the pulses the more the near field will be distorted and the more smudged picture will be for the far field off the axis (when the angle is more than 10°). But along the axis in the far field the picture is still close to the case of continuous excitation.

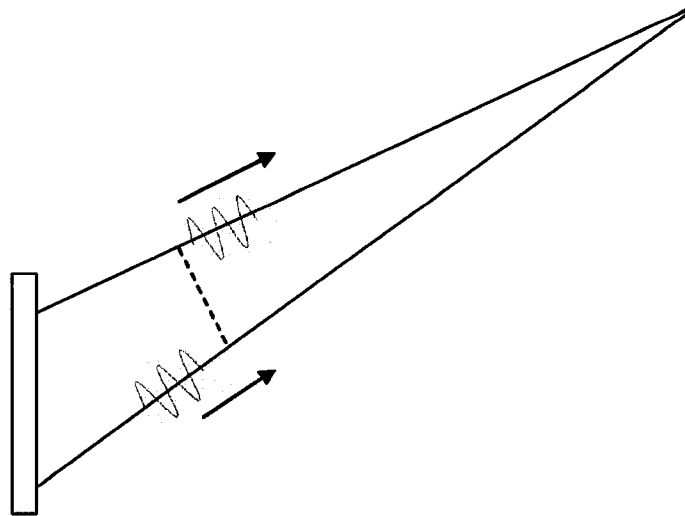


Figure 4. In the case of short pulses, in the areas away from central axis, the waves from different parts of the transducer can have a delay bigger than their lengths.

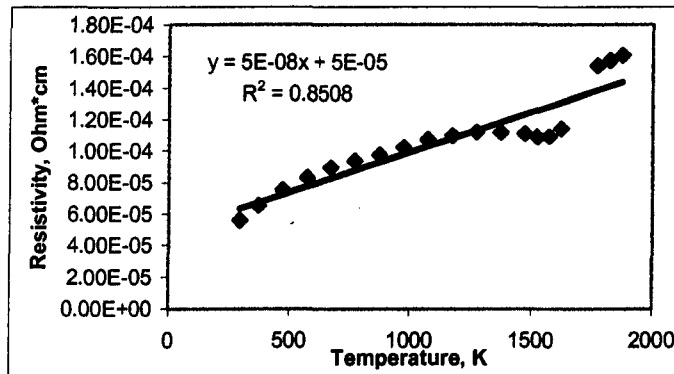
Appendix D

Linear Approximation Errors

In order to simplify analytical approach for both heat processes in spot welding and wave propagation in inhomogeneous media some nonlinear dependencies were approximated by first order polynomials – straight lines. This analysis is made to estimate the errors introduced by these approximations to the models.

Summary output for linear approximation of mild steel resistivity as function of temperature

Regression Statistics	
Multiple R	0.922379
R Square	0.850784
Adjusted R Square	0.842006
Standard Error	1.12E-05
Observations	19



ANOVA

	df	SS	MS	F	Significance F
Regression	1	1.21071E-08	1.21071E-08	96.92843	1.94507E-08
Residual	17	2.12343E-09	1.24908E-10		
Total	18	1.42306E-08			

% from average

Max error	2.00E-05 Ohm*cm	18.80
Average error	1.12E-05 Ohm*cm	10.53
Average resistivity	1.06E-04 Ohm*cm	100.00

The r-square value and estimator for variance was obtained from ANOVA summary

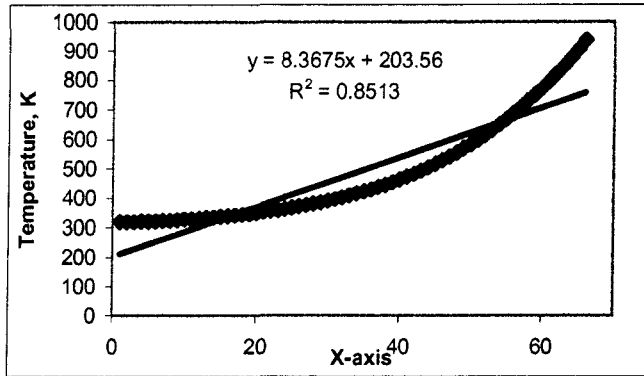
table using formulas $R^2 = \beta \frac{S_{xy}}{S_{yy}}$ $s^2 = \sum_{i=1}^N \frac{(y_i - \hat{y}_i)^2}{n-2} = \frac{S_{yy} - \beta S_{xy}}{n-2}$

ANOVA

	df	SS	MS	F	Significance F
Regression	1	βS_{xy}	βS_{xy}	MSrg/MSrs	
Residual	n-2	$S_{yy} - \beta S_{xy}$	$(S_{yy} - \beta S_{xy})/(n-2)$		
Total	n-1	S_{yy}			

SUMMARY OUTPUT for linear approximation of temperature distribution in copper

Regression Statistics	
Multiple R	0.922653
R Square	0.851288
Adjusted R Square	0.848965
Standard Error	67.65746
Observations	66



ANOVA

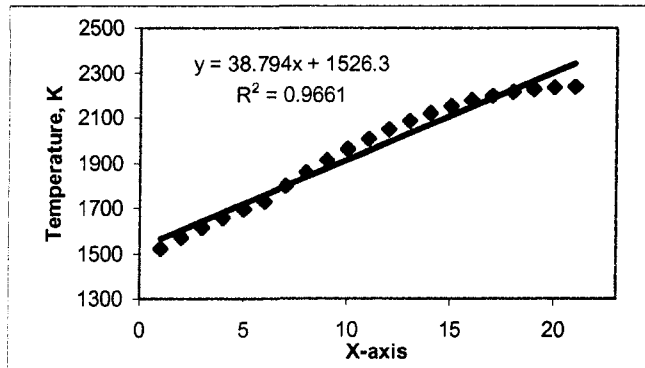
	df	SS	MS	F	Significance F
Regression	1	1677036.643	1677036.643	366.3626	3.51582E-28
Residual	64	292962.048	4577.532		
Total	65	1969998.691			

% from average

Max error	178 K	36.85
Mean error	67 K	13.87
Average temperature	483 K	100.00

SUMMARY OUTPUT for linear approximation of temperature distribution in steel

Regression Statistics	
Multiple R	0.982882
R Square	0.966056
Adjusted R Square	0.96427
Standard Error	46.29287
Observations	21



ANOVA

	df	SS	MS	F	Significance F
Regression	1	1158843.506	1158843.506	540.75	2.02228E-15
Residual	19	40717.57026	2143.030014		
Total	20	1199561.076			

% from average

Max error	103 K	5.27
Mean error	46 K	2.36
Average temperature	1953 K	100.00

Big error in temperature approximations is not extremely critical as far as we are concerned about integral delay of the signal. Total delay the analytical solution provides (using linear approximation) is not much different from that of the numerical (using exact distribution). By definition the least squares fitting guarantees minimized deviations of the approximation curve from real values. Theoretically, the total of all deviations from approximation is zero. In given case the difference is 0.0001%. Thus for the purposes of integral delay calculations the linear approximation provides the same result as exact distribution does.

Vita Auctoris

Name: Andriy M. Chertov
Place of birth: Simferopol, Ukraine
Date of birth: May 18, 1976
Education: BSc in Electronics Engineering (1998), Sevastopol State Technical University
BSc in Economics (1999), Sevastopol State Technical University

Articles

- “Neural Network Analysis in Nondestructive Characterization of the Resistance Spot Weld Quality” Authors: Kyung Cho Kim, Andriy Chertov, Roman Gr. Maev. Article is currently under review in Journal of Nondestructive Evaluation.
- Abstract for the article “Inverse Problem Solution to find real-time temperature distribution inside the spot weld medium using ultrasound time of flight methods” had been submitted in May 2003 to the 30th Annual QNDE conference. Authors: A.M. Chertov, R.Gr. Maev.